United States
Environmental Protection
Agency

Environmental Sciences Research
Laboratory
Research Triangle Park NC 27711

EPA-600/8-79-015a
June 1979

Research and Development

EPA

A Lagrangian Photochemical Air Quality Simulation Model

Adaptation to the St. Louis—RAPS Data Base Volume I. Model Formulation

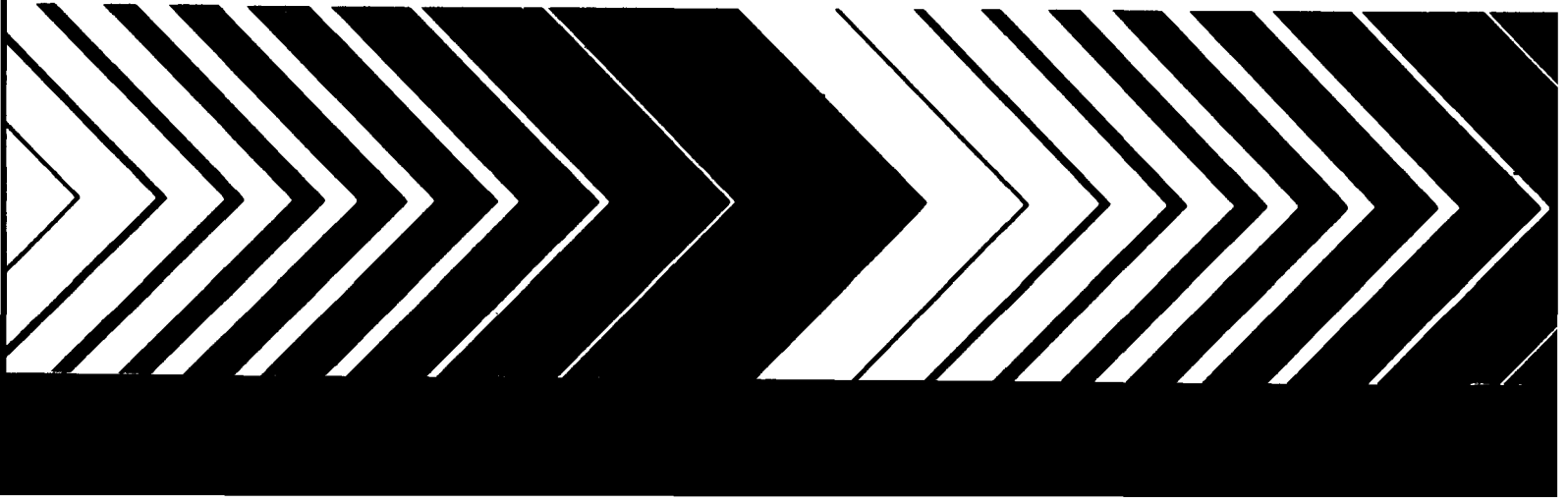

RESEARCH REPORTING SERIES

Research reports of the Office of Research and Development, U.S. Environmental Protection Agency, have been grouped into nine series. These nine broad categories were established to facilitate further development and application of environmental technology. Elimination of traditional grouping was consciously planned to foster technology transfer and a maximum interface in related fields. The nine series are:

1. Environmental Health Effects Research
2. Environmental Protection Technology
3. Ecological Research
4. Environmental Monitoring
5. Socioeconomic Environmental Studies
6. Scientific and Technical Assessment Reports (STAR)
7. Interagency Energy-Environment Research and Development
8. "Special" Reports
9. Miscellaneous Reports

This report has been assigned to the SPECIAL REPORTS series. This series is reserved for reports which are intended to meet the technical information needs of specifically targeted user groups. Reports in this series include Problem Oriented Reports, Research Application Reports, and Executive Summary Documents. Typical of these reports include state-of-the-art analyses, technology assessments, reports on the results of major research and development efforts, design manuals, and user manuals.

This document is available to the public through the National Technical Information Service, Springfield, Virginia 22161.

EPA-600/8-79-015a
June 1979

A LAGRANGIAN PHOTOCHEMICAL AIR QUALITY SIMULATION MODEL

Adaptation to the St. Louis - RAPS Data Base

Volume I. Model Formulation

by

Fred Lurman, Daniel Godden, Alan C. Lloyd, Richard A. Nordsieck
Environmental Research and Technology, Inc.
Environmental Analysis Division
2625 Townsgate Road
Westlake Village, California 91361

Contract No. 68-02-2765

Project Officer

Jack H. Shreffler
Meteorology and Assessment Division
Environmental Sciences Research Laboratory
Research Triangle Park, NC 27711

ENVIRONMENTAL SCIENCES RESEARCH LABORATORY
OFFICE OF RESEARCH AND DEVELOPMENT
U.S. ENVIRONMENTAL PROTECTION AGENCY
RESEARCH TRIANGLE PARK, NC 27711

DISCLAIMER

This report has been reviewed by the Environmental Sciences Research Laboratory, U.S. Environmental Protection Agency, and approved for publication. Approval does not signify that the contents necessarily reflect the views and policies of the U.S. Environmental Protection Agency, nor does mention of trade names or commercial products constitute endorsement or recommendation for use.

AFFILIATION

Dr. Shreffler, the Project Officer, is on assignment to the Meteorology and Assessment Division, Environmental Sciences Research Laboratory, from the National Oceanic and Atmospheric Administration, U.S. Department of Commerce.

ABSTRACT

A Lagrangian photochemical air quality simulation model has been adapted to St. Louis Missouri/Illinois metropolitan region and the Regional Air Pollution Study (RAPS) aerometric and emissions data base. This adaptation was performed to provide a means for EPA to independently assess the validity of a state-of-the-art Lagrangian photochemical model.

Chemical kinetic oxidation mechanisms involving hydrocarbons, nitrogen oxides and sulfur oxides and a vertical diffusion formulation developed by Environmental Research and Technology Inc. for modeling reactive pollutants in the troposphere are described. Methods for determining model input parameters are discussed and model results for ozone, nitrogen dioxide, carbon dioxide, sulfur dioxide, and sulfate are presented for three summer days in 1976. In considering so few simulations, no firm conclusions concerning model reliability are possible, although predicted pollutant concentrations are of reasonable levels. Most noteworthy for future users, the results suggest that the model may predict less ozone than is actually generated in St. Louis. Uncertainty in initial conditions of ozone and organic species is likely responsible for this discrepancy between observed and computed values.

CONTENTS

ABSTRACT		iii
LIST OF ILLUSTRATIONS		vii
LIST OF TABLES		ix
ACKNOWLEDGEMENTS		x
1.	INTRODUCTION	1-1
2.	MATHEMATICAL FORMALISM OF THE ATMOSPHERIC DIFFUSION MODEL	2-1
	2.1 Governing Equations	2-1
	2.2 Validity and Restrictions of the Lagrangian Air Parcel Concept	2-4
	2.3 Numerical Methods	2-5
	2.3.1 Spatial Discretion of the Governing Equations	2-5
	2.3.2 Solution of the Ordinary Differential Equations	2-9
3.	FORMALISM OF THE EDDY DIFFUSIVITY ALGORITHM	3-1
	3.1 K_z in the Surface Layer	3-1
	3.2 Evaluation of Surface Layer Parameters	3-2
	3.3 K_z in the Ekman Layer	3-3
	3.4 Application of Meteorological Data	3-9
4.	DEVELOPMENT OF A HOMOGENEOUS GAS PHASE MODEL FOR THE PREDICTION OF OZONE AND SULFATE FORMATION	4-1
	4.1 Formulation of a Chemical Mechanism for the HC/NO_x System	4-1
	4.1.1 Chemical Mechanism Development	4-2
	4.1.2 Kinetics and Mechanism for the Photochemical Model	4-2
	4.1.3 Salient Features of the Inorganic Mechanism	4-5
	4.1.4 Salient Features of the Organic Mechanism	4-12
	4.1.5 Validation of Photochemical Model	4-18
	4.1.6 Results and Discussion	4-19
	4.2 Formulation of a Chemical Mechanism for SO_2 Oxidation	4-45

	4.2.1	SO_2 Oxidation Chemistry	4-45
	4.2.2	Validation of the $HC/NO_x/SO_x$ System	4-50
	4.2.3	Results and Discussion	4-54
5.	ADAPTATION OF THE MODEL TO THE ST. LOUIS REGION AND RAPS DATA BASE		5-1
6.	METHODS AND RESULTS FOR TEST DAY SIMULATIONS		6-1
	6.1	Air Parcel Trajectories	6-1
	6.2	Meteorological Conditions	6-3
	6.3	Air Quality Conditions	6-15
	6.4	Source Emission Strengths	6-20
	6.5	Initial Pollutant Concentrations	6-20
	6.6	Simulation Model Results	6-27
7.	CONCLUSIONS AND RECOMMENDATIONS		7-1
8.	REFERENCES		8-1

LIST OF ILLUSTRATIONS

Figure		Page
2-1	Spatial Mesh Description	2-6
	Geometric Parameters of Spatial Mesh	2-6
	Discretized Air Parcel (not to scale)	2-6
3-1	Method of Updating Temperature Sounding	3-11
4-1	Scheme For Photooxidation of a Typical Aromatic Hydrocarbon Using Toluene as an Example	4-16
4-2	Simulation of Smog Chamber Experiment GC 116	4-20
4-3	Simulation of Smog Chamber Experiment GC 119	4-25
4-4	Simulation of Smog Chamber Experiment GC 133	4-28
4-5	Simulation of Smog Chamber Experiment GC 135	4-31
4-6	Simulation of Smog Chamber Experiment GC 138	4-34
4-7	Simulation of Smog Chamber Experiment GC 150	4-37
4-8	Simulation of Smog Chamber Experiment GC 156	4-40
4-9	Simulation of Smog Chamber Experiment B-S-114	4-55
4-10	Simulation of Smog Chamber Experiment B-S-110	4-57
4-11	Simulation of Smog Chamber Experiment B-S-107	4-60
5-1	RAPS Measurement Station Locations	5-2
5-2	Clear Sky Ultraviolet Radiation	5-4
6-1	Air Parcel Trajectory For 6-29-76	6-2
6-2	Air Parcel Trajectory For 7-13-76	6-4
6-3	Air Parcel Trajectory For 7-14-76	6-5
6-4	Vertical Temperature Profiles (6-29-76)	6-9
6-5	Vertical Temperature Profiles (7-13-76)	6-10
6-6	Vertical Temperature Profiles (7-14-76)	6-11
6-7	Initial Pollutant Concentration Vertical Profiles 6-29-76	6-24
6-8	Initial Pollutant Concentration Vertical Profiles 7-13-76	6-25

LIST OF ILLUSTRATIONS (CONTINUED)

Figure		Page
6-9	Initial Pollutant Concentration Vertical Profiles 7-14-76	6-26
6-10	Trajectory Model Concentration Predictions For 6-29-76	6-29
6-11	Trajectory Model Concentration Predictions For 6-29-76	6-30
6-12	Trajectory Model Concentration Predictions For 7-13-76	6-32
6-13	Trajectory Model Concentration Predictions For 7-13-76	6-33
6-14	Trajectory Model Concentration Predictions For 7-14-76	6-35
6-15	Trajectory Model Concentration Predictions For 7-14-76	6-36

LIST OF TABLES

Table		Page
3-1	Relationship of Pasquill Stability Categories To Ranges of the Parameter a (Fulle, 1975)	3-4
4-1	Detailed Composition of Hydrocarbon Surrogate Mixture	4-3
4-2	Generalized Reaction Mechanisms	4-6
4-3	Chemical Species Symbol Definitions	4-8
4-4	Surrogate Hydrocarbon Smog Chamber Runs Used For Model Testing and Development	4-43
4-5	Rate Constants Used For Hydrocarbons (ppm^{-1} min^{-1})	4-43
4-6	Additional Reactions Used For $HC/NO_x/SO_x$ Homogeneous Reaction Mechanism	4-51
4-7	Initial Conditions For Battelle Smog Chamber Simulations	4-53
6-1	Meteorological Conditions For 6/29/76	6-6
6-2	Meteorological Conditions For 7/13/76	6-7
6-3	Meteorological Conditions For 7/14/76	6-8
6-4	Vertical Eddy Diffusivity Coefficients For 6/29/76	6-12
6-5	Vertical Eddy Diffusivity Coefficients For 7/13/76	6-13
6-6	Vertical Eddy Diffusivity Coefficients For 7/14/76	6-14
6-7	Air Quality Along Trajectory For 6/29/76	6-16
6-8	Air Quality Along Trajectory For 7/13/76	6-17
6-9	Air Quality Along Trajectory For 7/14/76	6-18
6-10	Area Source Emissions Entrained Along Trajectories	6-21
6-11	Point Source Emissions Entrained Along Trajectories	6-21

ACKNOWLEDGMENTS

The work reported in this document was performed under contract to United States Environmental Protection Agency, Environmental Science Research Laboratory, Meteorological Assessment Division. The project monitor for the effort was Dr. Jack Shreffler.

This study was carried out by a project team led by Mr. Fred Lurmann of the Environmental Analysis Division of Environmental Research and Technology, Inc., at Santa Barbara, California. The project supervisor was Dr. Alan Eschenroeder, Manager of that Division. Other members of the project team included Dr. Alan Lloyd, Mr. Daniel Godden, and Mr. Richard Nordsieck.

We wish to thank the following programs, organizations, and individuals for their support and technical assistance in the model development program which preceded and made possible this study.

(1) Coordinating Research Council and members of the CRC-CAPA-12 Committee

(2) Los Angeles Reactive Pollutant Program (LARPP)

(3) Environmental Research & Technology's ARTSIM Research Program

(4) National Science Foundation

(5) Electric Power Research Institute

1. INTRODUCTION

The objective of this study is to provide a state-of-the-art Lagrangian photochemical air quality simulation model suitable for predicting atmospheric pollutant concentrations in the St. Louis, Missouri/Illinois Metropolitan Area. The Environmental Research & Technology, Inc., (ERT) Lagrangian Photochemical Diffusion Code has been adapted for use with the Regional Air Pollution Study (RAPS) meteorological and emissions data base and implemented on the Environmental Protection Agency's UNIVAC 1110 computer for this purpose. In adapting the model to the St. Louis region, a deliberate effort has been made to fully utilize the extensive data base provided by the RAPS field program. The model has been exercised for simulations of three summer days during 1976. These days were selected by the Environmental Protection Agency (EPA) to use to demonstrate the model's operational capabilities. A user's manual has been prepared to provide instructions for proper use of the computer programs and to document their computational procedures. Since it is the intent of EPA to exercise the code extensively, an integral part of this study has been to maximize the computational efficiency of the model and its interfaces with the RAPS data base.

This report is organized into two volumes. Volume I describes the mathematical, meteorological, and chemical formalism incorporated in the air quality simulation model. It provides an overview of the adaptation of the model to the St. Louis region and its data base. The methodology and results of air quality simulations for the test days are presented and interpreted. Exercises for evaluation of the model's predictive capabilities are suggested. Volume II consists of the user's manual for the code, which includes FORTRAN listings of the computer programs and instructions for their use.

2. MATHEMATICAL FORMALISM OF THE ATMOSPHERIC DIFFUSION MODEL

2.1 Governing Equations

The fundamental approach used to determine pollutant concentration in the ambient atmosphere involves solving the differential equations governing the conservation of pollutant mass. The general conservation equation for a particular pollutant may be written in vector form, as follows:

$$\frac{\partial c_i}{\partial t} = -\nabla \cdot (\vec{V} c_i) + \nabla \cdot (D \nabla c_i) + R_i + S_i \qquad (2\text{-}1)$$

with c_i = concentration of species i

i = 1, 2, 3, ..., n species

$\vec{V}$ = the wind velocity with components u, v, and w in the x, y, and z directions

$\nabla = \frac{\partial}{\partial x}\vec{i} + \frac{\partial}{\partial y}\vec{j} + \frac{\partial}{\partial z}\vec{k}$

x,y,z = component directions

$\vec{i},\vec{j},\vec{k}$ = units vectors in directions x, y, z, respectively

D = molecular diffusivity tensor

R_i = rate of generation of i^{th} species by chemical reactions

S_i = emission source strength for i^{th} species

Equation (2-1) states that the time rate of concentration change, $\frac{\partial c_i}{\partial t}$, is equal to the net effect of four processes:

(1) advection (or transport) of pollutant, $\nabla \cdot (\vec{u} c_i)$

(2) molecular diffusion, $\nabla \cdot (D c_i)$, of the pollutant;

(3) the change due to chemical reactions, R_i; and

(4) emissions source strength, S_i, of the pollutant.

The concentration and wind can be expressed in terms of turbulent deviations from their time-averaged values:

$$c_i = \bar{c}_i + c_i'$$

$$\vec{V} = \bar{\vec{V}} + \vec{V}'$$

thus

$$u = \bar{u} + u'$$

$$v = \bar{v} + v'$$

$$w = \bar{w} + w'$$

where bars above the quantities denote time-averaged values, and primes indicate turbulent eddy fluctuations.

By introducing the above expressions into Equation (2-1), taking time averages of each term, expanding, and rearranging terms, the following equation is obtained for the conservation of mass of species i in a turbulent atmosphere:

$$\frac{\partial \bar{c}_i}{\partial t} + \frac{\partial(\overline{uc_i})}{\partial x} + \frac{\partial(\overline{vc_i})}{\partial y} + \frac{\partial(\overline{wc_i})}{\partial z} + \frac{\partial(\overline{u'c_i'})}{\partial x} + \frac{\partial(\overline{v'c_i'})}{\partial y} + \frac{\partial(\overline{w'c_i'})}{\partial z}$$

$$= D_i \left(\frac{\partial^2 \bar{c}_i}{\partial x^2} + \frac{\partial^2 \bar{c}_i}{\partial y^2} + \frac{\partial^2 \bar{c}_i}{\partial z^2} \right) + R_i + S_i \qquad (2\text{-}2)$$

In order to reduce Equation (2-2) to a form tractable for solution, the following assumptions are made:

(1) Molecular diffusion is negligible in comparison to turbulent diffusion, hence $D_i = 0$.

(2) Atmospheric flow is incompressible, hence

$$\frac{\partial \bar{u}}{\partial x} + \frac{\partial \bar{v}}{\partial y} + \frac{\partial \bar{w}}{\partial z} = 0$$

(3) The turbulent eddy diffusion coefficients K_x, K_y, K_z may be defined as follows:

$$\overline{u'c_i'} = -K_x \frac{\partial \bar{c}_i}{\partial x}$$

$$\overline{v'c_i'} = -K_y \frac{\partial \bar{c}_i}{\partial y}$$

$$\overline{w'c_i'} = -K_z \frac{\partial \bar{c}_i}{\partial z}$$

Introducing these assumptions into Equation (2-2) gives;

$$\frac{\partial \bar{c}_i}{\partial t} + \bar{u} \frac{\partial \bar{c}_i}{\partial x} + \bar{v} \frac{\partial \bar{c}_i}{\partial y} + \bar{w} \frac{\partial \bar{c}_i}{\partial z} =$$

$$\frac{\partial}{\partial x}\left(K_x \frac{\partial \bar{c}_i}{\partial x}\right) + \frac{\partial}{\partial y}\left(K_y \frac{\partial \bar{c}_i}{\partial y}\right) + \frac{\partial}{\partial z}\left(K_z \frac{\partial \bar{c}_i}{\partial z}\right) + R_i + S_i \qquad (2\text{-}3)$$

Further simplification can be achieved by introducing the following additional assumptions:

(1) The vertical velocity component $\bar{w}$ can be neglected.

(2) Horizontal eddy diffusion can be neglected.

(3) The horizontal wind field can be considered uniform flow (i.e., no vertical or horizontal wind shear).

With these assumptions, Equation (2-3) reduces to:

$$\frac{\partial \bar{c}_i}{\partial t} + \bar{u} \frac{\partial \bar{c}_i}{\partial x} + \bar{v} \frac{\partial \bar{c}_i}{\partial y} = \frac{\partial}{\partial z}\left(K_z \frac{\partial \bar{c}_i}{\partial z}\right) + R_i + S_i \qquad (2\text{-}4)$$

This equation can be solved in the fixed x, y, z Eulerian coordinate system, or it can be transformed to a Lagrangian coordinate system, moving with horizontal velocity $\vec{V}$, $\vec{V} = u\vec{i} + v\vec{j}$, which results in further simplification. The transformation to the Lagrangian coordinate system reduces Equation (2-4) to:

$$\frac{\partial \bar{c}_i}{\partial t} = \frac{\partial}{\partial z}\left(K_z \frac{\partial \bar{c}_i}{\partial z}\right) + R_i + S_i \qquad (2\text{-}5)$$

This is the form of the governing equation assumed in the ERT Lagrangian Photochemical Diffusion model. Implicit in the coordinate transformation is the concept of an air parcel (or column) moving across a region with conservation of mass within its boundaries.

2.2 Validity and Restrictions of the Lagrangian Air Parcel Concept

Since the ERT Lagrangian Photochemical Diffusion Model solves the form of the conservation of mass equation shown in Equation (2-5), the appropriateness of the assumptions used in its formulation deserves discussion.

The assumption to neglect the vertical component of the wind velocity is believed to be realistic for regions with relatively smooth terrain. In regions with rough terrain, the occurrence of convergent or divergent flows caused by topographic constraints makes this assumption unrealistic.

The assumption to neglect horizontal and vertical wind shear is believed to be realistic under certain meteorological conditions and for limited modeling time periods. During daylight hours with moderate or strong wind velocities, the effects of shear are normally most important within a thin layer above the surface. Thus, if the wind speed used in the model to advect the parcel is chosen to be representative for the region above this layer, the assumption is realistic. For meteorological conditions characterized by light winds, the assumption is somewhat less reliable (as is the hourly averaged wind data). However, the light-wind conditions, for which vertical shear is most pronounced, occur more frequently at night, when the ground-level concentrations are lowest due to lower source strengths and slower chemical rates of transformation. In addition, it is believed that possible errors, introduced by the assumption, increase with time, so that the recommended duration for air parcel simulations is realistically limited to 8 to 12 hours. For practical purposes, then the zero-shear assumption is accepted with recognition of the associated uncertainties under some conditions.

Horizontal diffusion can realistically be neglected when the geographic distribution of emission strengths is fairly uniform in the proximity of the air parcel. Although area source emissions in an urban airshed generally have this characteristic, the superposition of major

point source emissions significantly reduces the uniformity of total emissions. To account for this phenomenon, the model has been formulated to include the approximate effects of lateral dispersion on emissions from major point sources in the source term, S_i, of Equation (2-5). Classical Gaussian plume solutions to the expression for mass conservation are used to determine the downwind distribution of mass from major point sources near the air parcel's trajectory. The model estimates discrete net amounts of point source emissions that are entrained into the passing air parcel. Thus, while the model's formalism does not account for lateral diffusion on a continuous basis, the effects due to major point sources are incorporated in an approximate manner. This approximation is generally realistic for an urban airshed where the area source emissions exceed the point source contributions.

In summary, the assumption of conservation of mass in a Lagrangian air parcel is realistic in regions with smooth terrain during daylight hours with significant wind velocities, provided that special treatment is given to lateral diffusion from major point sources.

2.3 Numerical Methods

2.3.1 Spatial Discretion of the Governing Equation

To solve Equation (2-5), the discrete spatial analog of the equation is formulated using finite difference approximations (also known as the method of lines). The spatial discretion employed allows variable-size mesh specification. Given the spatial mesh description, as shown in Figure 2-1, the continuous-time-discrete-space approximate is:

$$\frac{dc_j}{dt} = \left(\frac{K_{j-\frac{1}{2}}}{\Delta z_{j-1} h_j}\right) [I]\ c_{j-1} - \left(\frac{K_{j-\frac{1}{2}}}{\Delta z_{j-1} h_j} + \frac{K_{j+\frac{1}{2}}}{\Delta z_j h_j}\right) [I]\ c_j + \left(\frac{K_{j+\frac{1}{2}}}{\Delta z_j h_j}\right) [I]\ c_{j+1} + R_j + S_j \qquad (2\text{-}6)$$

where c_j = vector of n species concentration at j^{th} spatial mesh point.

Figure 2-1 Spatial Mesh Description

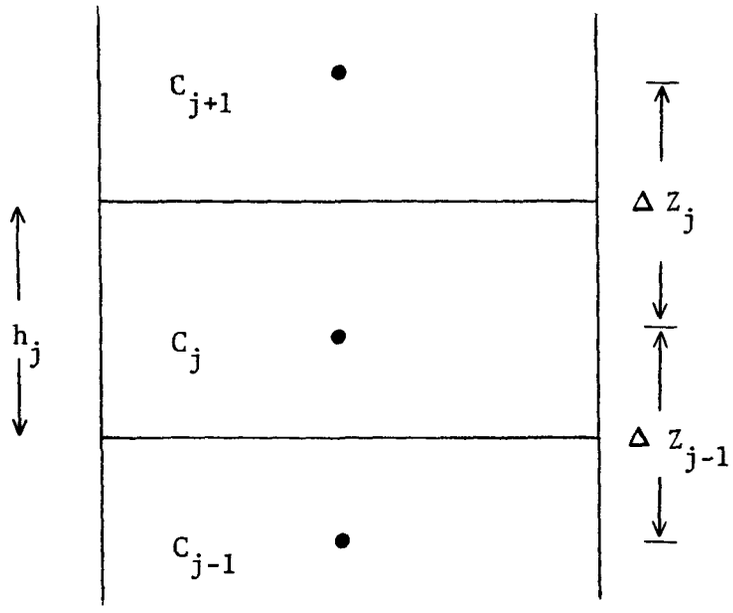

(a) Geometric Parameters of Spatial Mesh

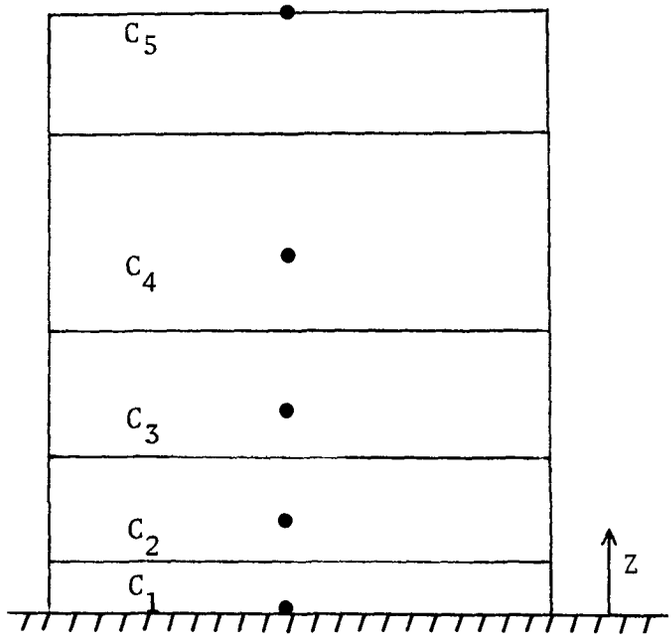

(b) Discretized Air Parcel (Not to Scale)

$K_{j-\frac{1}{2}}$ = vertical eddy diffusion coefficient between $(j-1)^{th}$ and j^{th} mesh points

$K_{j+\frac{1}{2}}$ = vertical eddy diffusion coefficient between j^{th} and $(j+1)^{th}$ mesh points

Δz_j = distance between j^{th} and $(j+1)^{th}$ mesh points

h_j = cell height, defined by $h_j = (\Delta z_{j-1} + \Delta z_j)/2$

[I] = identity matrix

R_j = vector of n species chemical rates for the j^{th} mesh points

S_j = vector of n species emission source rates for j^{th} mesh points

The boundary conditions for the equations are zero flux of pollutant mass through the ground and top edge of the air parcel. At the ground, which is surface mesh point 1, the boundary condition is:

$$K_1 \, [I] \, \frac{\partial c_1}{\partial z} = 0 \qquad (2\text{-}7)$$

This boundary condition is incorporated into the finite difference equation for the surface mesh point as follows:

Let: $\frac{\partial c_1}{\partial z} = \frac{c_2 - c_0}{\Delta z_0 + \Delta z_1}$ and $\Delta z_0 = \Delta z_1$

Thus: $c_0 = c_2$

Eliminating c_0 and Δz_0 in Equation (2-6) results in;

$$\frac{dc_1}{dt} = \left(\frac{K_{\frac{1}{2}} + K_{1\frac{1}{2}}}{\Delta z_1 h_1} \right) [I] \quad (-c_1 + c_2) + R_1 + S_1 \qquad (2\text{-}8)$$

Similarly, for the top mesh point, node n, the zero flux boundary condition results in $c_{N+1} = c_{N-1}$ and letting $\Delta z_N = \Delta z_{N-1}$ results in:

$$\frac{dc_N}{dt} = \left(\frac{K_{N-\frac{1}{2}} + K_{N+\frac{1}{2}}}{\Delta z_{N-1} h_N} \right) [I] \quad (c_{N-1} - c_N) + R_N + S_N \qquad (2\text{-}9)$$

In practice, to achieve the simulated reflection at the boundaries, $K_{\frac{1}{2}}$ and $K_{N+\frac{1}{2}}$ are chosen equal to $K_{1\frac{1}{2}}$ and $K_{N-\frac{1}{2}}$, respectively.

Surface deposition is treated as a sink for pollutant mass in the air parcel. In the present formulation, surface deposition is represented as a component, S_1^d, of the surface node source term S_1. Given the surface deposition velocity V_d for a particular species, this component is:

$$S_1^d = V_d C_1^p \left(\frac{2}{h_1} \right),$$

i.e., the surface flux is the product of the deposition velocity and the concentration to the power p.

The matrix form of Equation (2-6), which results after the incorporation of the boundary conditions, is written as:

$$\frac{dC}{dt} = QC + R + S \qquad (2\text{-}10)$$

where $C = [C_1, C_2, \ldots C_n]^T$

$R = [R_1, R_2, \ldots R_n]^T$

$S = [S_1, S_2, \ldots S_n]^T$

and

$$Q = \begin{bmatrix} -\frac{2K_{1\frac{1}{2}}}{z_1 h_1}[I] & \frac{2K_{1\frac{1}{2}}}{z_1 h_1}[I] & 0 & 0 & 0 \\ \frac{K_{1\frac{1}{2}}}{\Delta z_1 h_2}[I] & -\left(\frac{K_{1\frac{1}{2}}}{\Delta z_1 h_2} + \frac{K_{2\frac{1}{2}}}{\Delta z_2 h_2}\right)[I] & \frac{K_{2\frac{1}{2}}}{\Delta z_2 h_2}[I] & 0 & 0 \\ 0 & . & . & . & 0 \\ 0 & 0 & . & . & . \\ 0 & 0 & 0 & \frac{2K_{N-\frac{1}{2}}}{\Delta z_{N-1} h_N}[I] & \frac{2K_{N-\frac{1}{2}}}{\Delta z_{N-1} h_N}[I] \end{bmatrix}$$

It is important to note that this matrix has block-tridiagonal structure. Certain advantages associated with the use of matrices with this structure greatly reduce the computational effort for simultaneous solution of the equations.

2.3.2 Solution of the Ordinary Differential Equations

The continuous-time-discrete-space equation for n species at N mesh points results in an n x N system of ordinary differential equations. The solution to the system of equations is obtained by numerical integration, using a method first developed by Gear. The Gear-type integration algorithm used in the model is called EPISODE (Experimental Package of the Integration of Systems of Ordinary Differential Equations) and was developed by Hindmarsh and Byrne (1975) at the Lawrence Livermore Laboratory. A complete description of EPISODE is given by Hindmarsh and Byrne (1975), and will not be repeated here. The advantages of EPISODE are:

(1) its ability to integrate stiff equations;

(2) its use of a variable-order variable-step method;

(3) its ability to handle large systems of equations; and

(4) its economical operation due to its ability to take large steps by accurate tracking of the solution.

Most importantly, the backward differencing implicit method used by EPISODE assures numerical stability, regardless of spatial mesh size and equation stiffness.

The portion of the EPISODE package that solves the linear matrix equation QX = B for X by lower-upper (LU) decomposition at each time step has been modified to take advantage of the block-tridiagonal structure of Q. The mathematical formalism of LU decomposition on these type equations will not be presented here, but it is worth noting that it is believed to be the most efficient method available.

3. FORMALISM OF THE EDDY DIFFUSIVITY ALGORITHM

The vertical eddy diffusivity, K_z, is the parameter which controls the rate of vertical pollutant transfer in the atmosphere. For surface-based emissions of pollutants, large values of K_z result in vigorous vertical mixing and lower surface concentrations. Small values of K_z result in limited mixing and allow for surface build-up of pollutants.

This section of the report describes the theoretical basis and practice application of an algorithm to determine K_z coefficients as functions of height and time.

3.1 K_z in the Surface Layer

If it is assumed that atmospheric pollutants diffuse in the same manner as momentum, then the vertical eddy diffusivity in the surface layer is given by:

$$K_z = \frac{ku_* z}{\phi_m\left(\frac{z}{L}\right)} \tag{3-1}$$

where k = von Karman constant = 0.35 (Businger, et al, 1971)

u_* = friction velocity

z = height above ground

L = Monin-Obukhov length

ϕ_m = the non-dimensional wind shear.

By definition, $\phi_m\left(\frac{z}{L}\right)$ equals 1 for neutral conditions $\left(\frac{z}{L} = 0\right)$. For non-neutral conditions in the surface layer, Businger, et al (1971) developed the following formulae:

$$\phi_m\left(\frac{z}{L}\right) = \left[1 + 4.7\frac{z}{L}\right] \quad \text{for stable conditions } \left(\frac{z}{L} > 0\right) \tag{3-2a}$$

$$= \left[1 - 15\frac{z}{L}\right]^{-\frac{1}{4}} \quad \text{for unstable conditions } \left(\frac{z}{L} < 0\right) \tag{3-2b}$$

Substitution of Equations (3-2a and 3-2b) into Equation (3-1) yields formulae for determining K_z in the surface layer for non-neutral conditions:

$$K_z = \frac{ku_* z}{1 + 4.7\frac{z}{L}} \quad \text{for the stable case} \tag{3-3a}$$

$$= ku_* z \left(1 - 15\frac{z}{L}\right)^{\frac{1}{4}} \quad \text{for the unstable case.} \tag{3-3b}$$

In the neutral case, the equation for unstable conditions, (3-3b), is used with a large negative value of the Monin-Obukhov length ($L = -10^6$), which effectively reduces the equation to the form for neutral conditions.

The depth of the surface layer, and hence, the extent to which the surface formulae for K_z are applied, depends upon stability. Above the surface layer, in the region of the planetary boundary layer (PBL) often referred to as the Ekman layer, different formulations for K_z must be used. These formulations are presented in Section 3.3.

3.2 Evaluation of Surface Layer Parameters

The friction velocity u_* is determined in the model from the equation

$$u_* = \frac{ku(z_w)}{\int_{z_o}^{z_w} \frac{\phi_m\left(\frac{z}{L}\right)}{z} dz} \tag{3-4}$$

where z_w = wind measurement height

z_o = the roughness length.

Representations of $\phi\left(\frac{z}{L}\right)$ for stable and unstable conditions are given in Equations (3-2a and 3-2b). For the stable case, then,

$$u_* = \frac{ku(z_w)}{\ln\left(\frac{z_w}{z_o}\right) + \frac{4.7}{L}(z_w - z_o)} \tag{3-5}$$

Benoit's (1977) expression for the integral in Equation (3-4) is incorporated for unstable conditions, i.e.,

$$u_* = \frac{ku(z_w)}{\ln \frac{z_w}{z_o} + \ln \left[\frac{\left(\zeta_o^2 + 1\right)}{\left(\zeta_w^2 + 1\right)} \frac{\left(\zeta_o + 1\right)^2}{\left(\zeta_w + 1\right)^2} \right] + 2\left[\tan^{-1}(\zeta_w) - \tan^{-1}(\zeta_o)\right]} \quad (3\text{-}6)$$

where

$$\zeta_w \equiv \left(1 - 15\frac{z_w}{L} \right)^{\frac{1}{4}},$$

$$\zeta_o \equiv \left(1 - 15\frac{z_o}{L} \right)^{\frac{1}{4}}.$$

The Monin-Obukhov length (L) is determined by first evaluating the parameter a (Fulle, 1975), defined as

$$a = \left[\frac{1}{\left(10 + \frac{\partial T}{\partial z} \right)^2} + 0.0025 \frac{\partial u}{\partial z} \right]^{-\frac{1}{2}}. \quad (3\text{-}7)$$

The Pasquill stability class corresponding to a given value of a is determined as shown in Table 3-1, and then, L is determined within each class as a function of roughness length (z_o) using the method suggested by Golder (1972).

3.3 K_z in the Ekman Layer

O'Brien (1970) suggested an interpolation method to determine diffusivities between the top of the surface layer and the top of the planetary boundary layer (PBL). Taking into account the physical requirement that the first derivative of K_z be continuous with height in the Ekman layer, O'Brien formulated the second-order equation,

TABLE 3-1

RELATIONSHIP OF PASQUILL STABILITY CATEGORIES
TO RANGES OF THE PARAMETER a (FULLE, 1975)

a	Stability Class
$a \leq 7.0$	A (extremely unstable)
$7.0 < a \leq 8.0$	B (unstable)
$8.0 < a \leq 8.75$	C (slightly unstable)
$8.75 < a \leq 9.5$	D (neutral)
$9.5 < a \leq 11.25$	E (slightly stable)
$11.25 < a \leq 13.5$	F (stable)
$13.5 < a$	G (extremely stable)

$$K_z = K_A + \frac{(z - z_A)^2}{(z_A - z_B)^2} \left\{ K_B - K_A + (z - z_B) \cdot \left[\left(\frac{\partial K}{\partial z} \right)_{z=z_B} + 2 \frac{K_B - K_A}{z_A - z_B} \right] \right\} \quad (3\text{-}8)$$

where z = height at which K_z is to be determined

z_A = height of the PBL

z_B = height of the surface layer

K_A = value of K_z at the top of the PBL

K_B = value of K_z at the top of the surface layer.

The height of the PBL, z_A, in the neutral case was determined using the relationship (Blackadar and Tennekes, 1968)

$$z_A = c \frac{u_*}{f} \quad (3\text{-}9)$$

where u_* = the friction velocity

f = the Coriolis parameter.

The coefficient c has a value of 0.35 (Zilitinkevich, 1972).

In the non-neutral case the height calculated from Equation (3-9) is corrected for stability. For stable conditions the equation is

$$z_A = c\left(\frac{u_*}{f}\right)\left(\frac{u_*}{fL}\right)^{-\frac{1}{2}} \quad (3\text{-}10)$$

(Zilitinkevich, 1972). Reported values of c are 0.72 (Businger and Arya (1974) 0.22 (Wyngaard 1975), 0.40 (Brost and Wyngaard, 1978), and 0.27 (Rao and Snodgrass, 1978). For the present algorithm, a value of 0.35 was used. This value was chosen because it is near the center of the range reported and it is consistent with the value of c used in Equation (3-9). The effective mixing height, z_A, is not allowed to exceed the value calculated for neutral stability (Equation 3-9).

For unstable conditions, the equation used is

$$z_A = c \left(\frac{u_*}{f}\right)\left(-\frac{u_*}{fL}\right)^{\frac{1}{2}} \quad (3\text{-}11)$$

after Zilitinkevich (1972). The coefficient c was arbitrarily assigned a value of 0.35 to be consistent with the above formulations. In this case, z_A is not allowed to be less than the neutral case value, and, for the most unstable conditions, a maximum value of 2500m was assigned.

The determination of the height of the PBL from Equation (3-11) is not critical. An inversion, which limits the extent of vertical mixing, is generally present at some height well below z_A. In this case, the mixing height (H) determined in the conventional manner is used in place of z_A in Equation (3-8). This is the height in the most recent temperature sounding at which the potential temperature equals the potential temperature at the surface. That is, H is the height at which a line of slope -0.0098 °C/m (the dry adiabat) extended up from the observed surface temperature intersects the temperature profile. The height calculated by Equation (3-11) is used in the model as a secondary lid to define an upper limit to mixing for cases where no inversion is present in the temperature sounding.

The height of the surface layer in the neutral and stable cases is approximated as one-tenth the height of the PBL (Haltiner and Martin, 1957). That is,

$$z_B = 0.1 z_A .$$

For unstable conditions, z_B is estimated by

$$z_B = -5L ,$$

from Myrup and Ranzieri (1976), not to exceed the value

$$z_B = 0.1 z_A .$$

A very small value of K_z is assigned at the top of the boundary layer and above. That is,

$$K_A = 0.1 \text{ m}^2/\text{sec}$$

$$= 6.0 \text{ m}^2/\text{min}.$$

The value of K_z at the top of the surface layer is determined by evaluating the appropriate surface layer equation for $z = z_B$. In stable conditions, for example, Equation (3-3a) becomes

$$K_B = \frac{k\, u_* z_B}{1 + 4.7\frac{z_B}{L}} \quad .$$

It is also necessary when using Equation (3-8) to know the derivative of K_z with respect to z evaluated at height z_B. This is crucial to the determination of the shape of the K_z curve in the Ekman layer. In the stable case, Equation (3-3a) is differentiated and z_B substituted for z to yield

$$\left(\frac{\partial K}{\partial z}\right)_{z=z_B} = \frac{ku_*}{\left(1 + 4.7\frac{z_B}{L}\right)^2} \quad . \tag{3-12}$$

In the unstable case, the surface layer formula, Equation (3-3b), applies only within the layer where mechanically-induced turbulence is dominant in generating vertical mixing. At some height, or more specifically, at some value of $\frac{z}{L}$, turbulence induced by buoyancy effects is the dominant factor. Myrup and Ranzieri (1976) formulated an equation to describe buoyant eddy diffusion:

$$K_z = c\left(-\frac{0.4}{k}\,\frac{z}{L}\right)^{1/3} u_* z \quad . \tag{3-13}$$

They suggested that this equation be used for $\frac{z}{L} < -5$. A value of 0.58 for c is used to achieve continuity between Equation (3-13) and the surface layer formula (Equation 3-3b) at $\frac{z}{L} = -5$. This is incorporated into the present K_z algorithm as follows.

In the case when

$$-5L < 0.1H,$$

where H is determined as described above, then K_z is determined from Equation (3-13) for

$$-5L \leq z \leq 0.1H,$$

and the derivative of Equation (3-13), evaluated at z_B, is used in Equation (3-8). That is,

$$\left(\frac{\partial K}{\partial z}\right)_{z=z_B} = \frac{2}{3}\left(-\frac{0.4}{k}\frac{z_B}{L}\right)^{1/3} u_* \quad . \tag{3-14}$$

On the other hand, when

$$-5L \geq 0.1H \ ,$$

that is, for slightly unstable conditions, (Equation (3-13) is not used at all and the derivative of Equation (3-3b) evaluated at z_B,

$$\left(\frac{\partial K}{\partial z}\right)_{z=z_B} = ku_* \left(1 - 18.75\frac{z_B}{L}\right)\left(1 - 15\frac{z_B}{L}\right)^{-3/4} , \tag{3-15}$$

is used in Equation (3-8).

It is commonly observed that in the early morning a surface-based radiation inversion is surmounted by a deep neutral layer which is, in turn, capped by a subsidence inversion. The mixing which occurs in the elevated neutral layer is simulated by calculating K_z as though the layer extended to the surface. That is, if the top of the surface-based inversion is at 100m and the base of the elevated subsidence inversion is at 1,000m, then K_z is calculated between 100 and 1,000 in the same manner as if there were no surface-based inversion, except for one minor modification. To simulate a realistic transition across the upper boundary of the surface inversion, a smoothing factor is applied to the calculated values of K_z in the neutral layer. This factor is defined as:

$$S_1 = \left[\frac{z - z_T}{z_A - z_T}\right]^{1/4} \tag{3-16}$$

where z = height above surface

z_T = height of top of surface inversion

z_A = neutral boundary layer height (see Equation 3-9).

3.4 Application of Meteorological Data

The meteorological data base is used to evaluate the parameters used in the K_z algorithm as follows.

The information required to evaluate the parameter a (see Equation 3-7) and subsequently L, includes the vertical temperature gradient $(\frac{\partial T}{\partial z})$ and the vertical wind speed shear $(\frac{\partial u}{\partial z})$. The surface temperature gradient in the morning, when the temperature increases from its minimum value, is interpolated between an estimate of the maximum midday lapse rate $(-\frac{\partial T}{\partial z})$ and the neutral lapse rate (-0.98 °C/100m). The maximum midday temperature lapse rate is estimated from the nearest midday sounding. The depth of the layer of superadiabatic lapse (i.e., $-\frac{\partial T}{\partial z} > 0.98$) is also estimated from the available vertical temperature profile data. During this time, the temperature profile is updated each hour above the surface superadiabatic layer by extending a dry adiabat from the temperature at the top of the surface layer to its intersection with the initial profile.

In the afternoon, after the maximum surface temperature is reached and during the period when the surface temperature initially decreases, the temperature gradient is calculated from the surface temperature and the temperature at the top of the superadiabatic layer at the time of the maximum surface temperature.

Once the surface temperature has decreased such that the lapse rate in the surface layer is less than the neutral lapse rate, the surface lapse rate is estimated for each hour in a different manner. This estimation is accomplished by determining the slope of a line extending from the current surface temperature and intersecting the most recently updated profile at the height of the surface inversion top present in the morning's profile. This method is illustrated in Figure 3-1.

The wind shear, $\frac{\partial u}{\partial z}$, at the surface was estimated as

$$\frac{\partial u}{\partial z} = \frac{u(z_w)}{z_w}$$

where $u(z_w)$ is the wind speed along the trajectory at measurement height z_w. The estimate of $\frac{\partial u}{\partial z}$ is used along with the temperature gradient, as estimated above, to determine a value of L from the procedure described in Section 3.2.

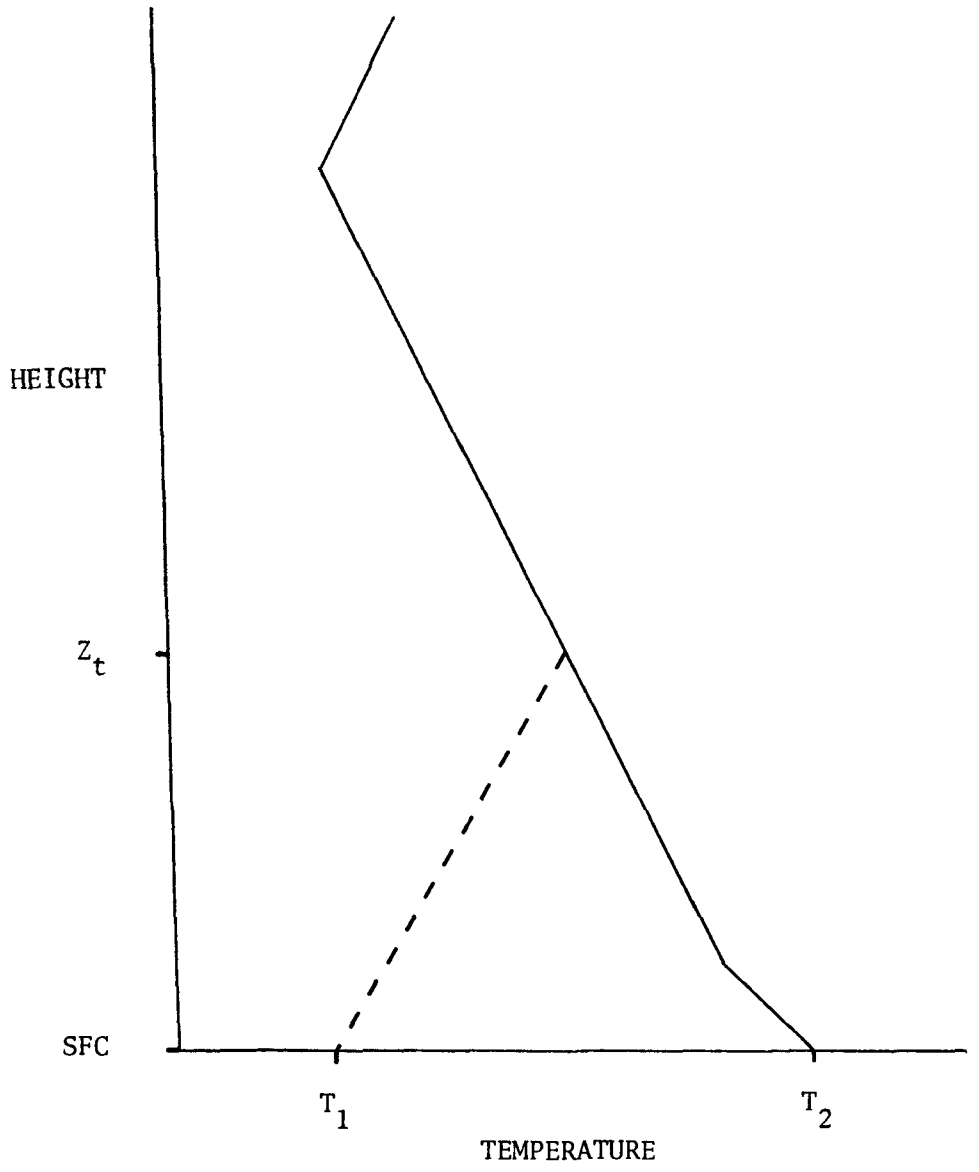

Figure 3-1 Method for updating sounding following afternoon temperature maximum. Solid line is temperature sounding at time of surface temperature maximum (T_m). Dashed line is subsequent update for a lower surface temperature (T_1). Z_t is depth of the morning's surface stable layer.

The wind shear in an elevated layer is approximated by first making an estimate using the logarithmic wind law for neutral conditions:

$$\frac{\partial u}{\partial z} \approx \frac{(u_2 - u_1)}{(z_2 - z_1)} = \frac{u_* \ln\left(\frac{z_2}{z_1}\right)}{k(z_2 - z_1)} \qquad (3\text{-}18)$$

where u_2 and u_1 are the estimated wind speeds at heights z_2 and z_1 corresponding to the top and the bottom of an elevated layer. The friction velocity, u_*, is determined initially from the logarithmic law using the interpolated surface wind:

$$u_* = \frac{ku(z_w)}{\ln\left(\frac{z_w}{z_o}\right)} \quad .$$

The wind shear for neutral conditions, $\left(\frac{\partial u}{\partial z}\right)_n$, determined from Equation (3-18), is used with the temperature gradient from the most recent profile to determine an initial value of L for the layer as described in Section 3.2. This value of L is then used to determine an initial non-neutral value of $\frac{\partial u}{\partial z}$ from the equations

$$\left(\frac{\partial u}{\partial z}\right)_u = \left(\frac{\partial u}{\partial z}\right)_n \left(1 - 15\frac{z_T}{L}\right)^{-1/4}$$

for unstable conditions, and

$$\left(\frac{\partial u}{\partial z}\right)_s = \left(\frac{\partial u}{\partial z}\right)_n \left(1 + 4.7\,\frac{z_T}{L}\right)$$

for stable conditions, where z_T is the height of the top of the layer. This procedure is repeated until the difference between the non-neutral $\frac{\partial u}{\partial z}$ on two successive iterations is sufficiently small to result in a difference of less than 1% in the corresponding values of L. This final value of L is then used to determine the stability within the elevated layer.

The estimated stability is used with the measured wind speeds each hour to determine the friction velocity, u_*, using Equation (3-5) or (3-6). As mentioned in Section 3, hourly-measured surface temperatures and available vertical temperature soundings are used to determine the mixing height, H.

3.5 Typical Profiles

Typical profiles of vertical eddy diffusivity are shown in Figure 3-2 and 3-3. Figure 3-2 depicts a profile under stable conditions, as with a surface-based inversion. Figure 3-3 shows a typical profile for an unstable mixed layer capped by an elevated inversion.

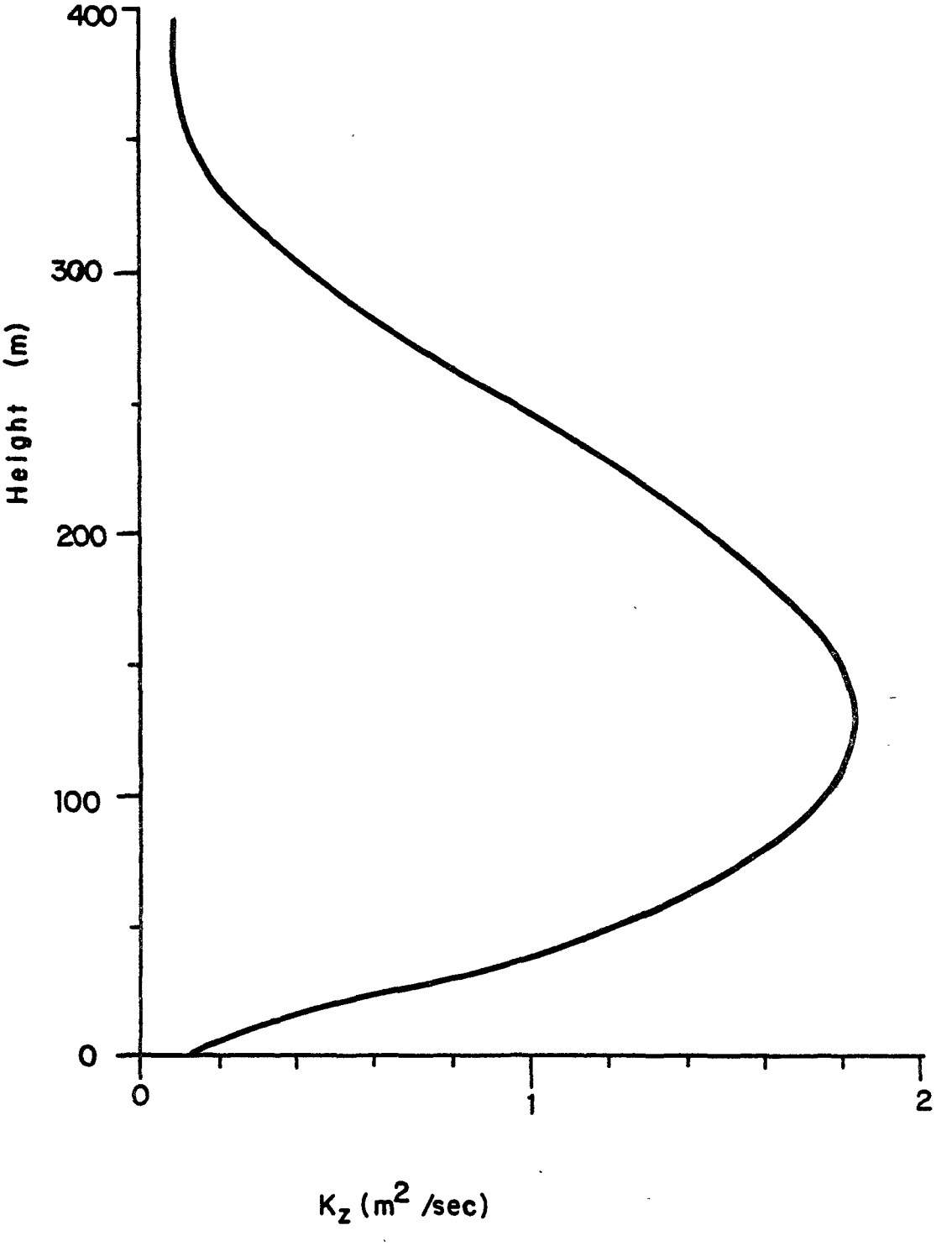

Figure 3-2. Vertical Eddy Diffusivity Profile for Slightly Stable Conditions (L=1060m, and u* = 0.09 m/sec).

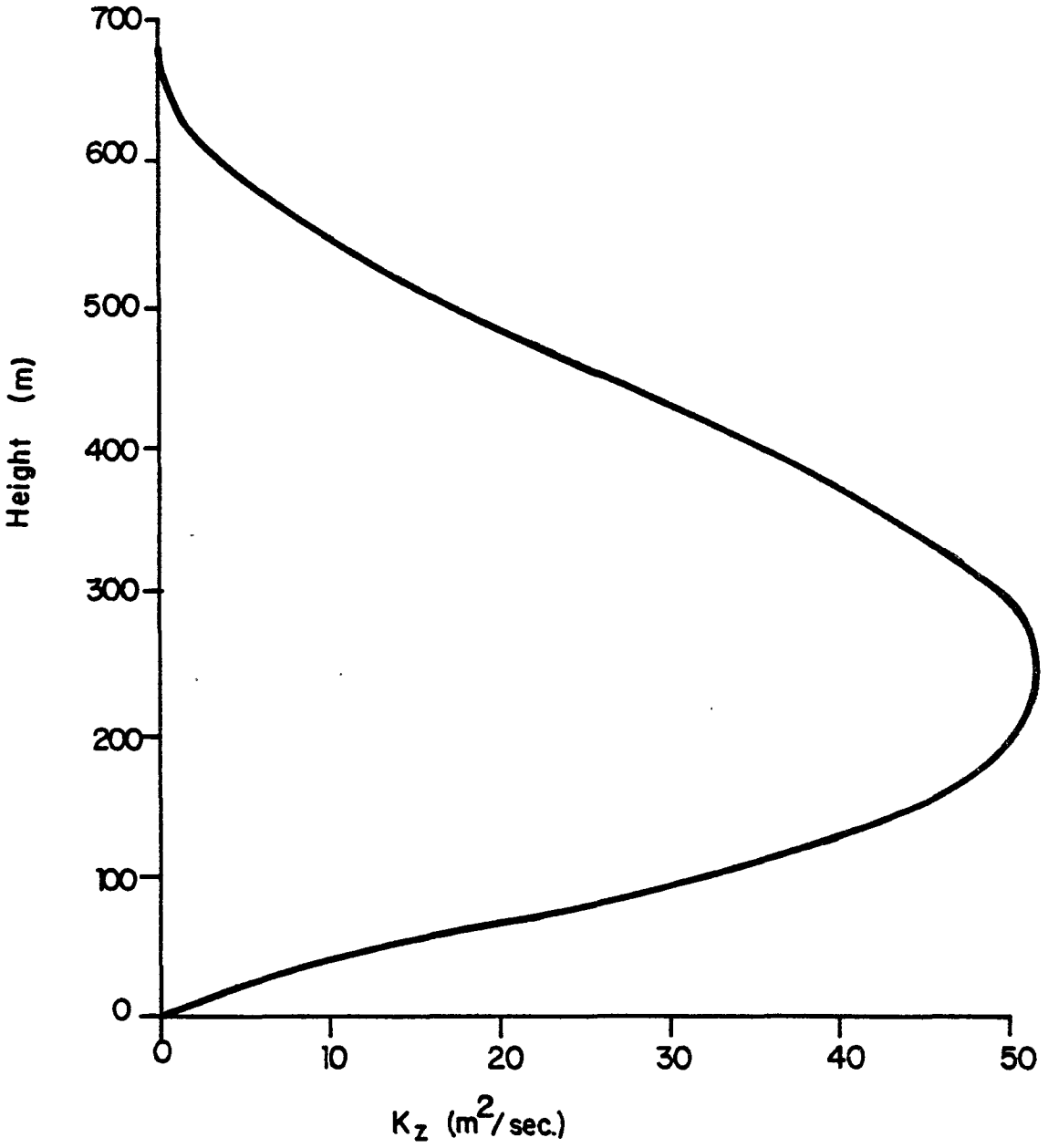

Figure 3-3. Vertical Eddy Diffusivity Profile for Unstable Conditions (L=-27m, u*=0.36, and H=670m).

W790050

4. DEVELOPMENT OF A HOMOGENEOUS GAS PHASE MODEL FOR THE PREDICTION OF OZONE AND SULFATE FORMATION

This section describes the formulation of a chemical mechanism to describe the gas phase reactions which produce ozone (O_3) and sulfate ($SO_4^=$) from irradiated mixtures of hydrocarbons (HC), nitrogen oxides (NO_x) and sulfur dioxide (SO_2). The majority of the work for this part of the model development was carried out under funding from the Coordinating Research Council and the National Science Foundation. Only slight modifications were made under this EPA program.

It is recognized that major advances have been made in our understanding of certain segments of the mechanism (e.g., O_3 - olefin reactions, aromatic hydrocarbon photooxidation) since the formulation of this mechanism. However, due to time constraints of this program, these latest changes are not reflected in the mechanism. Updating of the chemical mechanism incorporating the latest information is currently being carried out under continued funding from the Coordinating Research Council.

The following discussion describes initially the chemistry occurring in the hydrocarbon/nitrogen oxides (HC/NO_x) system and subsequently, the additional reactions necessary to describe the homogeneous gas phase conversion of SO_2 to sulfate. This is followed by a description of the reactions used to computer model the hydrocarbon/NO_x/SO_x system and a presentation of the comparison of the predicted results against smog chamber data.

4.1 Formulation of a Chemical Mechanism for the HC/NO_x System

The chemical kinetic mechanism for the HC/NO_x system, including the appropriate rate constants, is discussed in detail below. Briefly, it is a lumped hydrocarbon model in which the hydrocarbons are partitioned among five classes, namely, alkanes, alkenes, aromatics, formaldehyde and the higher aldehydes. In addition, some of the other oxygenated hydrocarbons, such as ketones, may be placed into the higher aldehyde category if desired.

A detailed discussion is given of the inputs into the chemical mechanism formulation. This was felt necessary since the quality of

the results of model predictions is a strong function of the input data (kinetic, mechanistic and experimental).

4.1.1 Chemical Mechanism Development

The chemical mechanism used was tested against various smog chamber data in a systematic manner. The following chamber data (from the University of California, Riverside chamber facility) (Pitts, et al, 1977a; Pitts, et al, 1976; Pitts, et al, 1975a) have been utilized:

- n-butane/NO_x mixtures
- propylene/NO_x mixtures
- n-butane/propylene/NO_x mixtures
- surrogate hydrocarbon mixtures representative of the atmosphere and composed of 4 alkanes, 4 olefins, 2 aromatics, 2 aldehydes, CO, CH_4, and acetylene. The detailed composition is shown in Table 4-1 (Pitts, et al, 1975a).

The calculations, including those involving SO_2 described later, were performed on an IBM 360/75 computer and a CDC 6400 computer, using a chemical kinetics program written in FORTRAN IV. The list of species, reactions and rate constants, and stoichiometric coefficients were input to the program, forming a set of kinetic differential equations. These equations were integrated, using an ordinary differential equation integration package developed by Gear (1971) for the variable-step-variable-order integration of coupled differential equations. Calculations were done in single precision with an error bound of 0.1%. Integrations ran smoothly with no problems encountered due to stiffness.

4.1.2 Kinetics and Mechanism for the Photochemical Model

In developing the chemical module for the atmospheric model, extensive use has been made of previous and current studies. These include those by Niki, et al (1972); Demerjian, et al (1974); Hecht, et al (1974); Whitten and Hogo (1977); Graedel (1976); and Carter, et al (1978). However, in order for the chemical scheme to have practical applications in terms of airshed models, the number of species has to be

TABLE 4-1

DETAILED COMPOSITION OF HYDROCARBON SURROGATE MIXTURE
(modified from Pitts, et al, 1975a)

Compound Class	Detailed Composition and Concentration (parts per billion as carbon, ppbC)
Alkanes	Ethane (160), Propane (40), n-Butane (785), 2,3-Dimethyl butane (615)
Alkenes	Ethene (84), Propene (35), cis-2-Butene (60), 2-Methyl-2-Butene (70)
Aromatics	Toluene (115), m-Xylene (325)
Aldehydes	Formaldehyde (54), Acetaldehyde (5)
Miscellaneous	Acetylene (101), Acetone (6), Methane (2800), Carbon Monoxide (7000)

carefully limited. Thus, inherently, the mechanism is an approximation adapted to the treatment of multicomponent mixtures of great complexity in contrast to the models developed by the majority of the above workers.

Our chemical mechanism has been significantly changed from that of Hecht, et al (HSD) (1974); however, our partitioning of the hydrocarbons into classes is very similar to that used by HSD with the exception of the fact that the aldehydes are split between formaldehyde and the higher aldehydes.

As indicated above, the formulation of a chemical kinetic scheme for use in an atmospheric model requires a substantial reduction in the level of chemical detail to be treated. For example, the numerous individual hydrocarbons must be "lumped" into various representative categories. The type of lumping employed can vary. Thus, we have partitioned the hydrocarbons into five classes, while other workers have used fewer classes (Hecht, et al, 1974) or have treated the total reactive hydrocarbons in terms of propylene (Graedel, et al, 1976; Wayne, et al, 1971) or a mixture of propylene and n-butane (Dodge, 1977) -- the latter two compounds representing the highly reactive and lesser reactive species, respectively, in the atmospheric mixture.

In view of the differences in reaction mechanisms, we felt at the outset that the hydrocarbons should be divided among alkanes, alkenes, aromatics, formaldehyde and the higher aldehydes. As with any lumping technique, errors are incurred, for example, an average, mole-weighted rate constant, which is representative of the class, has to be chosen. Where there is a wide variation in rate constants within a class, this assumption leads to an over or underprediction in reactivity during different stages of the reaction. A problem inherent with our approach is the fact that the grouping, represented by the symbol "R" for the generalized case, does not get degraded as rapidly in the model as would happen under experimental conditions, e.g., reaction 35 (Table 4-2) shows that R occurs on both sides of the equation although a carbon atom has been lost through the production of CO. We have tried to minimize the effect of this approximation by including nitrate and other stable product formation, and by differentiating among the alkyl groups originating from alkane and alkene species, e.g., alkanes are denoted by PA and alkenes by OLEF.

The extensive body of smog chamber data obtained by the Statewide Air Pollution Research Center of the University of California, Riverside, in its studies for the California Air Resources Board (Pitts, et al, 1975; 1976) has proved invaluable in checking the simulations against experimental observations under varying HC/NO_x ratios and total concentrations of HC and NO_x.

The reaction mechanism for the HC/NO_x system is presented in Table 4-2. Table 4-3 lists the definitions of the chemical species symbols used in Table 4-2. The additional reactions necessary to describe the SO_2 oxidation are presented later in this report. The rate constants shown in Table 4-2 are operative at 305°K and refer to the hydrocarbon mix used by Pitts, et al, in their smog chamber studies. In instances where M or O_2 occur in the reaction mechanism, their concentration has been included in the rate constant to give a pseudo first or second order rate constant.

4.1.3 Salient Features of the Inorganic Mechanism

The inorganic mechanism for hydrocarbon/NO_x/air mixtures has been generally well characterized. The mechanism has been discussed extensively in previous publications (Niki, et al, 1972; Demerjian, et al, 1974; Hecht, et al, 1974; Whitten and Hogo, 1977; Graedel, et al, 1976; Carter, et al, 1978), and the major reactions of O_3, NO, NO_2 and water are generally well known. However, continuing research has uncovered some important reactions, such as the formation of pernitric acid, HO_2NO_2, which have previously been neglected. In addition, recent work on OH reactions with NO, NO_2 and CO has led to the use of higher values of their rate constants. These recent studies have shown the importance of studying reactions under atmospheric conditions of temperature and pressure.

Many of the rate constants were taken from the National Bureau of Standards Technical Note #866, entitled "Chemical Kinetics and Photochemical Data for Modeling Atmospheric Chemistry" (Hampson and Garvin, 1975). In some cases, particularly for the organic reactions, kinetic data are generally taken from the work of Carter, et al (1978), while the remainder were derived in studies carried out for the Coordinating Research Council (Lloyd and Tashima, 1977) and the National Science

TABLE 4-2

GENERALIZED REACTION MECHANISMS

		Rate Constants (ppm^{-1} min^{-1}) at 305°K and 1 Atmosphere
1	$NO_2 + h\nu = O + NO$	3.20E-01
2	$O + O_2 (+ M) = O_3 (+ M)$	4.12E+06
3	$O_3 + NO = NO_2 + O_2$	2.50E+01
4	$NO + NO_2 + H_2O = 2HONO$	2.20E-09
5	$HONO + HONO = NO + NO_2 + H_2O$	1.40E-03
6	$HONO + h\nu = OH + NO$	8.96E-02
7	$OH + NO + M = HONO + M$	1.50E+04
8	$OH + NO_2 + M = HNO_3 + M$	1.50E+04
9	$OH + CO = HO_2 + CO_2$	4.40E+02
10	$HO_2 + NO = NO_2 + OH$	1.20E+04
11	$HO_2 + NO_2 = HO_2NO_2$	1.20E+03
12	$HO_2 NO_2 = HO_2 + NO_2$	4.00E+00
13	$HO_2 + HO_2 = H_2O_2 + O_2$	8.40E+03
14	$NO_2 + O_3 = NO_3 + O_2$	5.00E-02
15	$NO_3 + NO = 2NO_2$	1.30E+04
16	$NO_3 + NO_2 = N_2O_5$	5.60E+03
17	$N_2O_5 + H_2O = 2HNO_3$	5.00E-06
18	$N_2O_5 = NO_3 + NO_2$	2.40E+01
19	$OH + OLEF = AO_2$	4.00E+04
20	$AO_2 + NO = NO_2 + AO$	2.90E+04
21	$AO + O_2 = RCHO + HCHO + HO_2$	4.10E+05
22	$O_3 + OLEF = 0.5HCHO + 0.5RCHO + 0.25HO_2 + 0.25RCO_3 + 0.5OH + 0.5RCHO_2$	2.00E-01
23	$RCHO_2 + NO_2 = NO_3 + 0.5HCHO + 0.5RCHO$	2.30E+04

TABLE 4-2 (CONTINUED)

		Rate Constants (ppm^{-1} min^{-1}) at 305°K and 1 Atmosphere
24	$RCHO_2$ + NO = NO_2 + 0.5HCHO + 0.5RCHO	2.90E+04
25	O + OLEF = .3EPOX + .3RCHO + .4HO_2 + .4RO_2	2.30E+04
26	OH + PA = H_2O + PAO_2	3.80E+03
27	PAO_2 + NO = NO_2 + .85PAO + .15RO_2	2.90E+04
28	PAO_2 + NO = NTRA	2.60E+03
29	PAO = RO_2 + .5HCHO + .5RCHO	1.40E+05
30	PAO + O_2 = .5KET + .5RCHO + HO_2	6.70E+04
31	PAO + NO_2 = .85NTRA + .15RCHO + .15HONO	2.30E+04
32	RO_2 + NO = NO_2 + PAO	2.90E+04
33	OH + RCHO = RCO_3 + H_2O	2.20E+04
34	RCHO + hν = RO_2 + HO_2 + CO	1.40E-04
35	RCO_3 + NO = CO_2 + NO_2 + RO_2	2.90E+04
36	RCO_3 + NO_2 = PAN	1.70E+04
37	PAN = RCO_3 + NO_2	6.60E-02
38	HCHO + hν = 2.HO_2 + CO	2.30E-04
39	HCHO + OH = H_2O + HO_2 + CO	2.10E+04
40	RO_2 + HO_2 = RO_2H + O_2	4.20E+03
41	O_3 + WALL = LOSS OF O_3	3.21E-04
42	AR + OH = AROH + HO_2	2.24E+04
43	AROH + OH = ARCO	5.02E+04
44	ARCO + NO = NO_2 + RCHO	2.90E+04
45	AR + OH = H_2O + ARO	5.60E+03
46	ARO + NO = NO_2 + HO_2 + AR'CHO	2.90E+04

TABLE 4-3

CHEMICAL SPECIES SYMBOL DEFINITIONS

Species	Symbol Designation
AO	Alkoxy radical equivalent of AO_2
AO_2	Product of OH addition to olefin in the presence of O_2
AR	Aromatic hydrocarbons
ARCO	Product of addition of OH to a cresol in the presence of O_2
ARO	Product of H-abstraction from side chain alkyl group on benzene ring followed by addition of O_2 to radical formed
AR'CHO	Aromatic aldehyde
AROH	Cresol
CO	Carbon monoxide
CO_2	Carbon dioxide
D	Criegee intermediate ($RCHO_2$)
EPOX	Epoxide formed from O atom addition to olefin
HCHO	Formaldehyde
HONO	Nitrous acid
HNO_3	Nitric acid
HO_2NO_2	Pernitric acid
HO_2	Hydroperoxyl radical
H_2O	Water
H_2O_2	Hydrogen peroxide
HV	Photon
KET	Ketone
M	Any third body, such as N_2 or O_2
NO	Nitric oxide
NO_2	Nitrogen dioxide

TABLE 4-3 (CONTINUED)

Species	Symbol Designation
NO_3	Nitrate radical
N_2O_5	Dinitrogen pentoxide
NTRA	Organic nitrate
O	Oxygen atom (ground state)
O_2	Oxygen
O_3	Ozone
OH	Hydroxyl radical
OLEF	Alkenes (olefinic hydrocarbons)
PA	Alkanes (paraffinic hydrocarbons)
PAN	Peroxyacetyl Nitrate
PAO	Alkoxy radical formed by PA
PAO_2	Alkyl peroxy radical from the O_2 addition to the radical formed by H-abstraction from a paraffinic hydrocarbon
R	Generalized alkyl group (e.g., C_2H_5, C_3H_7, etc.)
RCHO	Aldehydes other than formaldehyde
RCO_3	Acyl peroxy radical
RO	Alkoxyl radical
RO_2	Alkyl peroxy radical
RO_2H	Product of disproportionation between HO_2 and RO_2

Foundation (Martinez, et al, 1977). The majority of the following discussions has appeared in these two reports but will be repeated here for completeness.

There are recent experimental data for several of the inorganic reactions of interest. These are discussed in detail below:

The Chemistry of Nitrous Acid

The formation of nitrous acid by the reaction

$$NO + NO_2 + H_2O \rightleftarrows 2HONO$$

has been investigated recently by several workers, including Chan, et al (1976); Cox (1975); and Zafonte, et al (1975). This reaction together with the reaction

$$OH + NO + M \rightarrow HONO + M$$

are presumed to be the major sources of nitrous acid formation in chamber studies, and probably in ambient air. We have used the data obtained by Chan, et al (1976), for the formation and destruction of nitrous acid. In addition, we have used the photolysis rate constant obtained by Cox and Derwent (1977).

In order to account for the radical initiation in smog chamber studies (Whitten and Hogo, 1977; Carter, et al, 1978; Dodge, 1977; Niki and Weinstock, 1975; Wu, et al, 1976) and to take into account chamber wall contamination (Bufalini, et al, 1972), we have used a portion of the equilibrium HONO concentration to provide an initial radical source to initiate the photochemical smog reactions (Whitten and Hogo, 1977; Jeffries, et al, 1975). As discussed in Section 4.1.6, the values used are usually one quarter of the equilibrium HONO concentration. One problem in using this method to account for the radical initiation is that it tends to shorten the ozone initiation time, but does not adequately account for radical production later in the run. In essence, it affects the time to ozone maximum but not the value of the maximum. However, if no significant initial radical source is used in simulating smog chamber experiments, then the reactivity of the system, in terms of time to NO_2 maximum, rate of NO oxidation, etc., is invariably under-predicted. As discussed below, it may be unnecessary to use initial

HONO as a radical initiator under ambient conditions since there may be sufficient aldehydes present.

The Reaction of HO_2 with NO

There have been several studies (Hampson and Garvin, 1975) of the reaction

$$HO_2 + NO \rightarrow NO_2 + OH \quad .$$

We have used the value reported by Howard (1977), who obtained a rate constant of $1{\cdot}2 \times 10^4$ ppm^{-1} min^{-1} based on a laser magnetic resonance study of HO_2.

The Formation of Pernitric Acid From The Reaction of HO_2 With NO_2

The importance of pernitric acid in photooxidation studies involving nitrogen oxides has become increasingly evident in the last few years (Niki, et al, 1976a; Levine, et al, 1977). While earlier studies (Simonaitis and Heicklen, 1974; Cox and Derwent, 1975; Simonaitis and Heicklen, 1976) showed the formation of nitrous acid from this reaction, there now seems to be reasonable agreement that pernitric acid is the major, if not the only, product, Niki, et al (1976a; 1977a).

$$HO_2 + NO_2 \rightarrow HO_2NO_2 \quad .$$

Pernitric acid decomposes in a manner similar

$$HO_2NO_2 \rightarrow HO_2 + NO_2$$

to peroxyacetyl nitrate with a rate constant which obeys the Arrhenius expression

$$k = 1{\cdot}3 \times 10^{14} \exp\left(\frac{-20700}{RT}\right) \quad sec^{-1} \quad \text{(Graham, et al, 1977).}$$

The value chosen for the HO_2NO_2 decomposition rate affects the final O_3 peak since HO_2NO_2 acts as a reservoir for NO_2. A short lifetime means that the net effect of reaction (11) on O_3 production is not significant, and vice versa.

O_3 Decay at the Smog Chamber Walls

In order to model O_3 behavior in a chamber, one has to take into account the O_3 reactions with the walls of the chamber. This is usually calculated by measuring the rate of decay of ozone in a nonirradiated chamber and quoting a half-life for the dark decay. A half-life of 35 hours for dark decay was used (Darnall, 1977) for the simulations of the surrogate data from the UCR-SAPRC glass chamber, indicating that the surface is very inert to ozone reaction.

4.1.4 Salient Features of The Organic Mechanism

The standard organic reactions used in modeling studies have been discussed in detail by many workers (Niki, et al, 1972; Demerjian, et al, 1974; Hecht, et al, 1974; Whitten and Hogo, 1977; Graedel, et al, 1976; Hendry, et al, 1978; Carter, et al, 1978). Thus, the present discussion of individual reactions is limited to a few key aspects in the treatment of the organic system.

Olefin Reactions With O_3

The major role in photochemical oxidant formation played by the reactions of O_3 with olefins has been known for many years and described in detail elsewhere (Niki, et al, 1972; Demerjian, et al, 1974; Hecht, et al, 1974; Whitten and Hogo, 1977; Graedel, et al, 1976; Carter, et al, 1978). Recently (Niki, et al, 1976; Niki, 1977; Walter, et al, 1977), studies have shown that the reaction produces fewer radicals than previously thought. Thus, a major advance was made with the definitive identification of a stable secondary ozonide by Niki, et al (1976), which confirmed the earlier but less definitive work of Hanst, et al (1958). Therefore, it appears that Criegee biradicals ($RCHO_2 \cdot$) are formed under atmospheric conditions and last sufficiently long to react bimolecularly. We have assumed that they react rapidly with NO and NO_2. However, there is still significant uncertainty concerning the relative rates of molecular (path A) compared to fragmentation routes (path B) in

the overall reaction

$$O_3 + R\text{-}CH = CHR_1 \rightarrow 0.5RCHO + 0.5R_1CHO + 0.5RCHO_2\cdot + 0.5R_1CHO_2 \quad (A)$$

$$O_3 + R\text{-}CH = CHR_1 \rightarrow 0.5RCHO + 0.5R_1CHO + 0.5RCO + 0.5R_1CO + OH \quad (B)$$

where $RCHO_2\cdot$ and $R_1CHO_2\cdot$ represent the Criegee intermediates. Early modeling studies depicted the O_3-olefin reaction in terms of path B. The net reaction and overall rate constant are shown in Table 4-2. Equal partitioning between the two paths has been assumed in the current study.

In a surrogate hydrocarbon model, the uncertainty of the mechanism of the ozone-olefin reaction is compounded by the uncertainty inherent in choosing an appropriate olefin representative of the bulk olefin mixture. Such a choice has a bearing on both the rate constant and the mechanism.

In this study, a molar-weighted rate constant was chosen based on the composition of the surrogate hydrocarbon mixture used in the smog chamber experiments. Thus, the olefins used in the surrogate mixture are ethylene, propylene, cis-2-butene, and 2-methyl 2-butene, as shown in Table 4-1. The value of the molar-weighted rate constant derived lies between the value for the reaction of O_3 with propylene and that for cis-2-butene, while the mechanism is largely representative of that for propylene.

Olefin Reactions With OH

The consumption of olefins, during the early stages of reaction before a significant build-up of ozone occurs, is attributed to the reaction with the hydroxyl radical (Niki, et al, 1972; Demerjian, et al, 1974). Olefins react rapidly with OH. Cvetanovic (1976) has shown that the mechanism is largely one of addition, with about 65% of reaction occurring by addition to the internal carbon atom, while the other 35% occurs by addition to the terminal carbon atom. The mechanism used in this study ignores any hydrogen abstraction from the olefin.

Following addition of OH and subsequently of O_2 to the radical so produced (reactions 18-20), the mechanism predicts the conversion of two molecules of NO to NO_2, which is consistent with the findings of the work of Carter, et al (1978). This is also generally consistent with

the recent studies of Niki (1977). This mechanism differs from that used by Demerjian, et al (1974), since the reaction of O_2 with the hydroxy-type radical (RCHOH), shown as reaction 21 in Table 4-2, leads to the production of HO_2 and an oxygenated species, rather than addition of O_2 to the RCHOH radical as follows;

$$RCHOH + O_2 \rightarrow RCH(O_2)OH$$

Olefin Reactions With Oxygen Atoms

Under atmospheric conditions, the major portion of the oxygen atoms generated by NO_2 photolysis combines with molecular oxygen to form ozone. However, oxygen atoms react rapidly with olefins, particularly the internally-bonded olefins, and, thus, in the early stages of reaction when the olefin concentration is reasonably high, the overall rate of reaction of O atoms with olefins can be significant and helps to initiate radical production and to commence the process of ozone formation (Niki, et al, 1972; Demerjian, et al, 1974; Hecht, et al, 1974; Whitten and Hogo, 1977; Graedel, et al, 1976; Carter, et al, 1978). Our mechanism reflects the recent work of Singleton and Cvetanovic (1976), and the reaction mechanism is shown by reaction 24 in Table 4-2. It is seen that some stable products, such as epoxides, are formed part of the time, while other products result from radical fragmentation processes. The partitioning among the two will undoubtedly change depending upon the olefins, but we have chosen to use the results for propylene as being typical of the mixture under study. This should also be a reasonable assumption for olefins encountered in ambient air.

The Photooxidation of Alkanes

It is assumed in this study that the only mechanism for the consumption of alkanes under ambient conditions is that due to reaction with OH. Since the C-H bond strengths in the paraffins are reasonably high (95-98 kcal mol^{-1}), the only species for which hydrogen abstraction reactions are significantly fast is OH. The alkane photooxidation mechanism is probably the best understood of all the hydrocarbon species (Whitten and Hogo, 1977; Carter, et al, 1978) and is represented by reactions 26-33 in Table 4-2.

The mechanism used in this study includes the results reported by Carter, et al (1976) and Darnall, et al (1976) -- namely, the formation of nitrates from the longer chain ($\geq C_4$) alkanes in the RO_2 + NO reaction, as shown below, and the isomerization of alkoxy radicals formed from C_{4+} hydrocarbons. For example, the ratio of rate constants for the reaction

$$(27) \quad PAO_2 + NO \rightarrow NO_2 + PAO$$

to that of

$$(28) \quad PAO_2 + NO \rightarrow \text{Nitrate}$$

is about 11.2, as determined earlier by Darnall, et al (1976), in a chamber study of n-butane/NO_x/air mixtures.

The mechanism also takes into account nitrate formation from the normal reaction of alkoxy radicals with NO_2 (reaction 33); in this case the alkoxy radical is denoted by PAO, which is the radical derived from the paraffins. Naturally, the choice of 11.2 for the ratio of k_{27}/k_{28} may vary in going to ambient air when significant proportions of longer-chain alkanes are present. Thus, the choice of this ratio in any model application has to be examined in light of any detailed hydrocarbon data available from urban airshed studies specific to the region under consideration. Otherwise, the value of 11.2 may be used.

Aromatic Hydrocarbon Photooxidation

At the time when this study was being carried out, very little information existed on the photooxidation of aromatic compounds under photochemical smog conditions. The mechanism shown in Table 4-2, taking toluene as a representative aromatic hydrocarbon, included the known results of that time. Thus, the mechanism reflects the known addition (Davis, et al, 1975; Hansen, et al, 1975; Doyle, et al, 1975; Lloyd, et al, 1976) of OH to the aromatic compound followed by subsequent reactions shown. In addition, it is assumed that abstraction of hydrogen atoms from the side chain occurs about 20% of the time (Perry, et al, 1977; Hendry, 1977), with the net result of the formation of an aldehyde, e.g., from toluene, benzaldehyde would be produced, as shown in Figure 4-1.

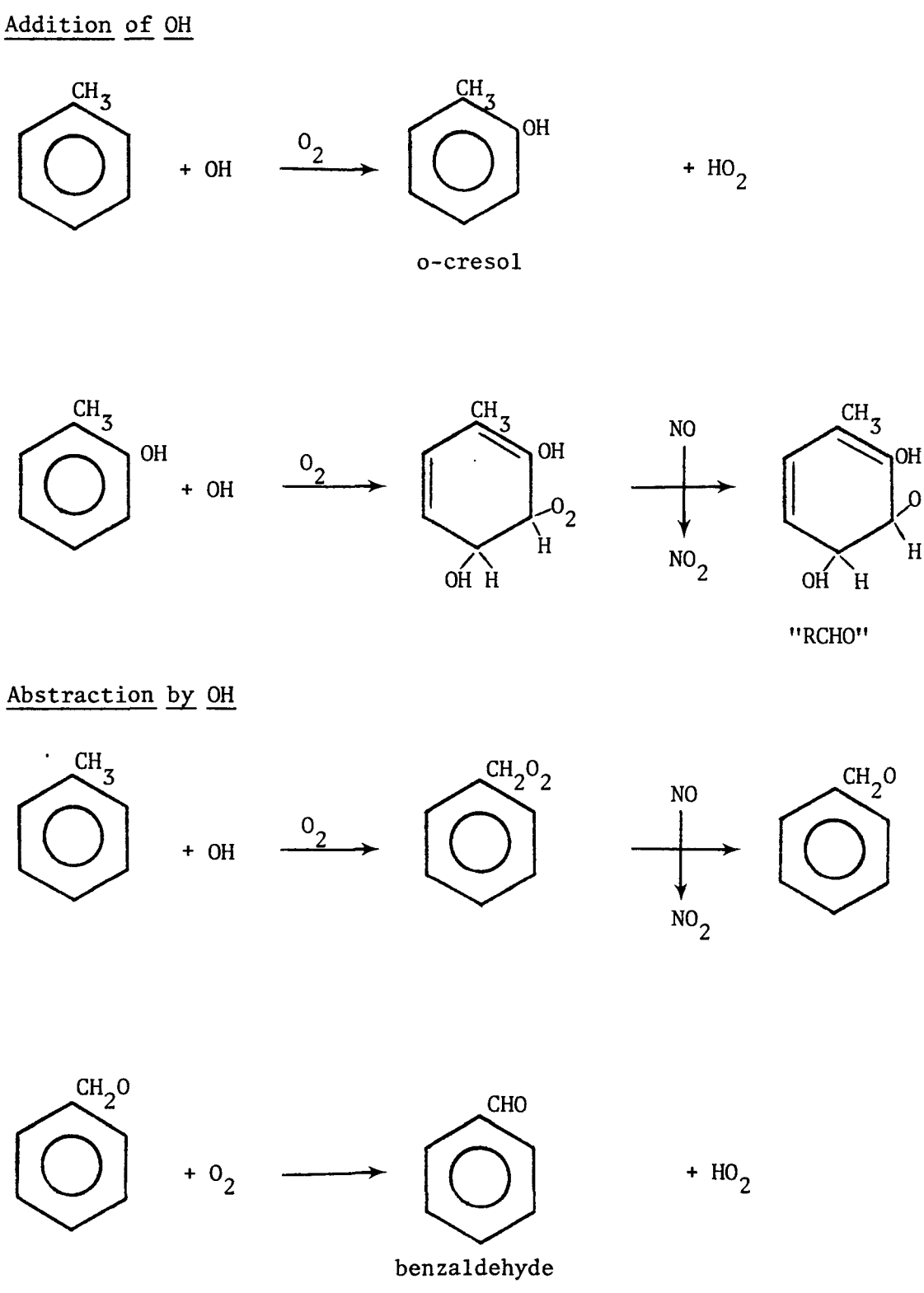

Figure 4-1 Scheme for Photooxidation of a Typical Aromatic Hydrocarbon Using Toluene as an Example

The mechanism considers the possibility of ring-opening following addition of OH and O_2 to the cresol formed from the addition of OH to toluene. Such ring-opening has been suggested by O'Brien (1975) and Hendry (1977). Likely products from ring-opening would involve multi-functional oxygenated compounds, and we have chosen to represent these compounds by an aldehyde, RCHO. This is done to conserve the number of species involved in the model, but also to take into account the possibility that the products resulting from ring-opening will be photoreactive and create further radicals. This technique has been used previously (Pitts, 1975).

The reaction mechanism is currently being refined as more data on the aromatic photooxidation steps become available. The revised mechanism is being formulated and tested under another program sponsored by the Coordinating Research Council.

Aldehyde Photolysis

It has been known for some time that aldehydes are key radical initiators in the photooxidation systems present in ambient air and in smog chambers (Pitts, et al, 1976; Demerjian, et al, 1974; Dodge and Hecht, 1975; Dodge and Whitten, 1976). Quantum yields for radical production for aldehydes in air are highly uncertain, although it has been shown that the rate constants for aldehyde photolysis are very important in terms of photochemical smog modeling (Dodge and Hecht, 1975).

Our mechanism differentiates between formaldehyde and the higher aldehydes. We feel this is important in view of the different radicals formed and the slightly different shape of the formaldehyde absorption curve compared with the higher aldehydes (Calvert and Pitts, 1966). This is most manifested by the absorption at longer wavelengths by formaldehyde compared with the other aldehydes, and this is reflected in the urban airshed model by a difference in their photolysis rate constants with altitude. In addition, by differentiating the aldehydes in this way, more realistic predictions of PAN concentrations are possible since formaldehyde does not form PAN.

Our model calculations are sensitive both to the initial concentrations used for aldehydes, as well as to the rate constants used for

photolysis. We have chosen rate constants for aldehyde photolysis based on measurements obtained in the glass chamber at UCR and the quantum yields of Lee, et al (1976). We have taken into account the recent work of Weaver, et al (1976), by combining the two possible photooxidation paths, one which is dependent on the oxygen concentration, and the other which is independent. In addition, we have assumed that the formyl radical formed upon photolysis of formaldehyde reacts with O_2 as follows:

$$HCHO + h\nu \rightarrow H_2 + HCO$$

$$HCO + O_2 \rightarrow HO_2 + CO$$

This pathway has been shown by Niki, et al (1977) to be the major one occurring under atmospheric conditions, rather than the alternative suggestion:

$$HCO + O_2 \rightarrow HCO_3$$

In view of the sensitivity of the model to both the rate constant and the initial conditions, it would be highly desirable for better data to be available both on the photochemistry of the aldehydes under ambient conditions and on measurements in ambient air under varying levels of photochemical smog intensity. Results of measurements of formaldehyde quantum yields obtained after completion of this work have been recently summarized (Lloyd, 1978).

4.1.5 Validation of Photochemical Model

A number of smog chamber runs were modeled to ascertain the appropriateness of both the inorganic mechanism and the mechanism used to describe the photooxidation of the alkanes and the alkenes. Specifically, runs were carried out for mixtures of n-butane/NO_x and propylene/NO_x in air, and a binary mixture of propylene and n-butane in air containing NO_x. These chamber data were obtained for the EPA at the smog chamber facility at the University of California, Riverside (Pitts, et al, 1977). The evacuable, teflon-lined chamber irradiated by a solar simulator was used in these runs (Beauchene, et al, 1973).

4.1.6 Results and Discussion

Figure 4-2 is included as being typical of the results obtained for the n-butane/propylene mixtures. This figure shows that the mechanism used in this study predicted well the decay of both the paraffin and the olefin, although in the later stages of the irradiation, the model slightly overpredicted the decay. While the predicted ozone initiation time was slightly shorter than the experimental value, the overall agreement between the experimental and predicted values is good. The overprediction of the PAN concentration is reflected in the underprediction of the later NO_2 concentrations. Little effort was expended in refining the details of the mechanism since the overall goal is to model a complex hydrocarbon mixture under ambient conditions.

As indicated earlier, the smog chamber data chosen to represent a complex hydrocarbon mixture was that obtained at SAPRC, under a California Air Resources Board contract. In contrast to the above data, these were obtained in an all-glass chamber operated under conditions of room temperature and pressure and irradiated externally by banks of black lights (Pitts, et al, 1975, 1976). Table 4-4 shows the specific runs chosen for model validation purposes. These span a variety of hydrocarbon/NO_x ratios to provide a reasonably stringent test for the model.

In order to employ appropriate rate constants for this complex hydrocarbon mix, the mole-weighted rate constants for the reactions of OH with alkanes, aromatics and olefins, the reactions of O atoms with olefins, and the reaction of ozone with olefins were obtained. These values were derived by weighting the appropriate rate constants of the elementary reactions to reflect the concentration of the individual components in the mix. In this way, reasonably representative rate constants were obtained. The rate constants used are shown in Table 4-5, while the mole-weighted values used in our computations and derived from these values and the individual compound concentrations present in the surrogate mixture, are included in Table 4-2.

Figures 4-3 to 4-8 show the comparison of the computed values and experimental data obtained for the various smog chamber runs selected for model validation. The mechanism used for these runs is the same as that shown in Table 4-2. The initial concentration of HONO was kept at one quarter the equilibrium value for four runs but was placed at 1/16

Figure 4-2 Simulation of Smog Chamber Experiment EC 116

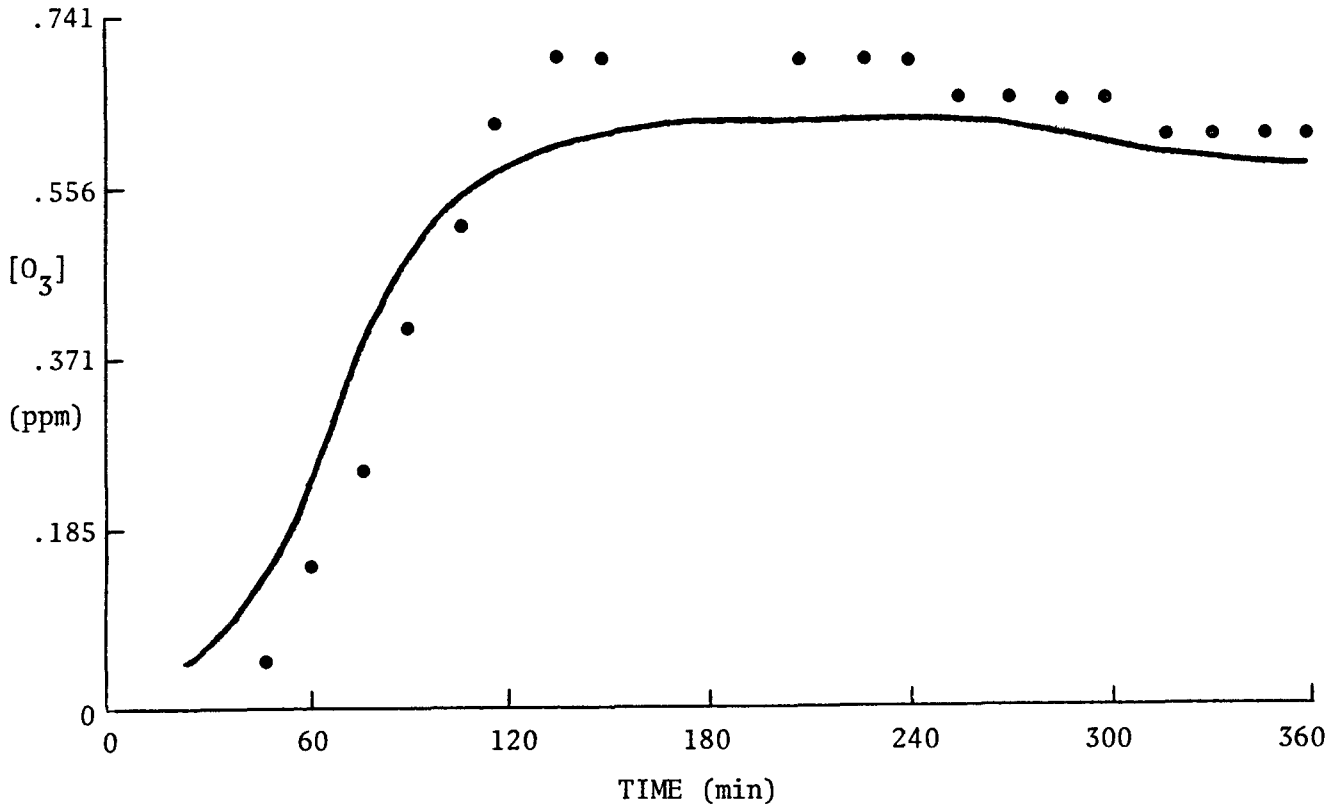

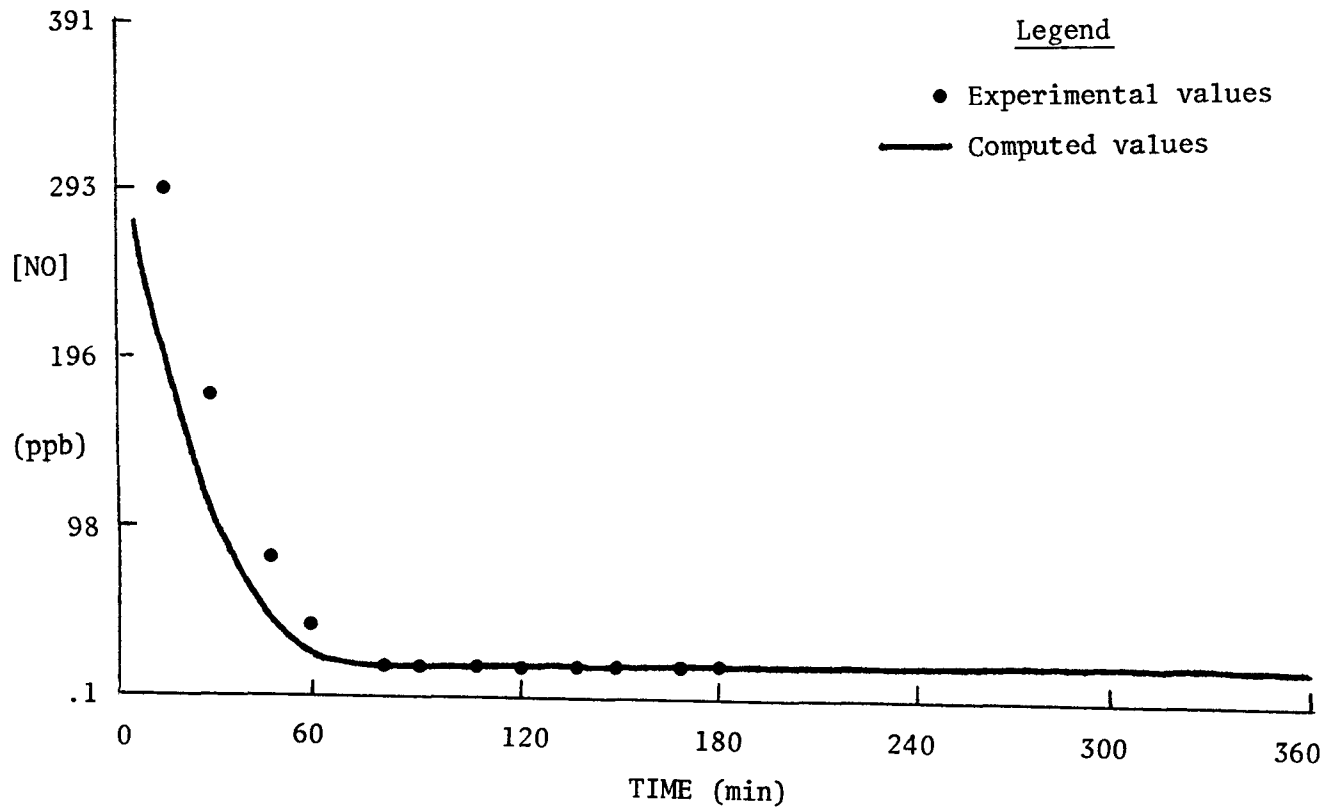

Figure 4-2 Simulation of Smog Chamber Experiment EC 116
(continued)

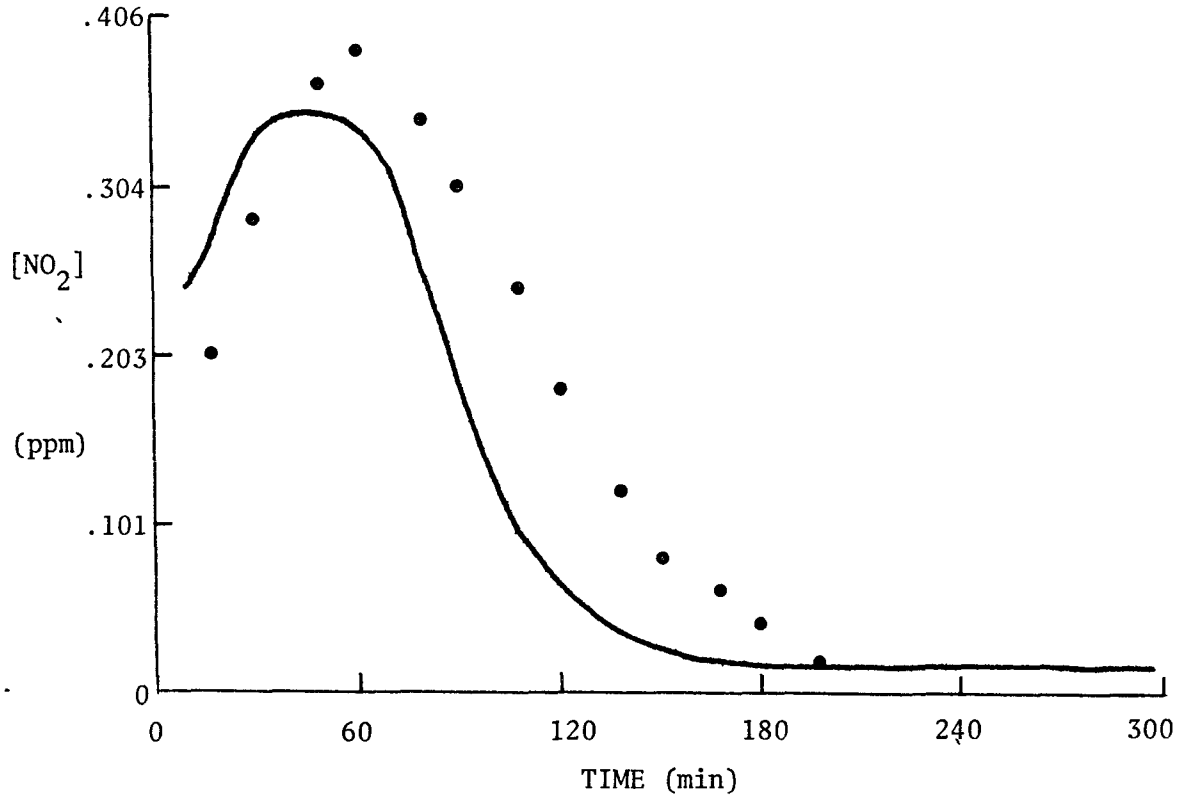

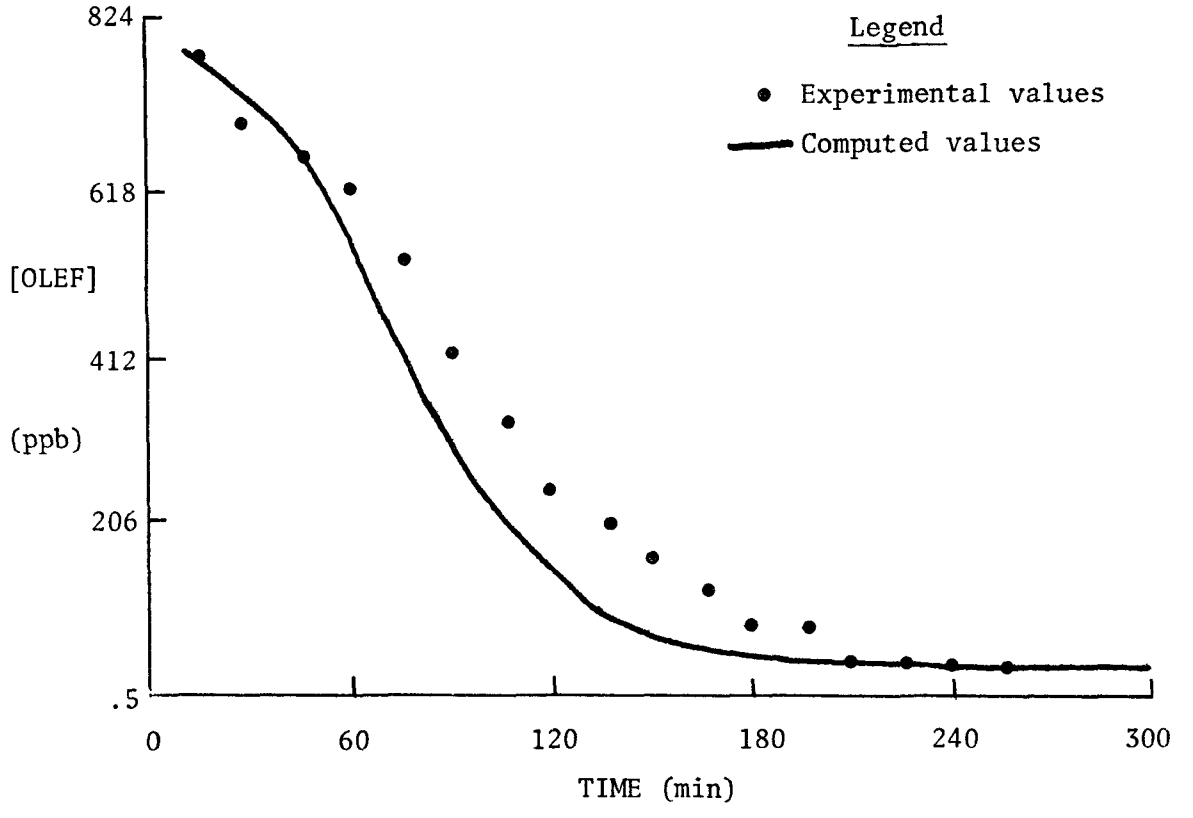

Figure 4-2 Simulation of Smog Chamber Experiment EC 116
(continued)

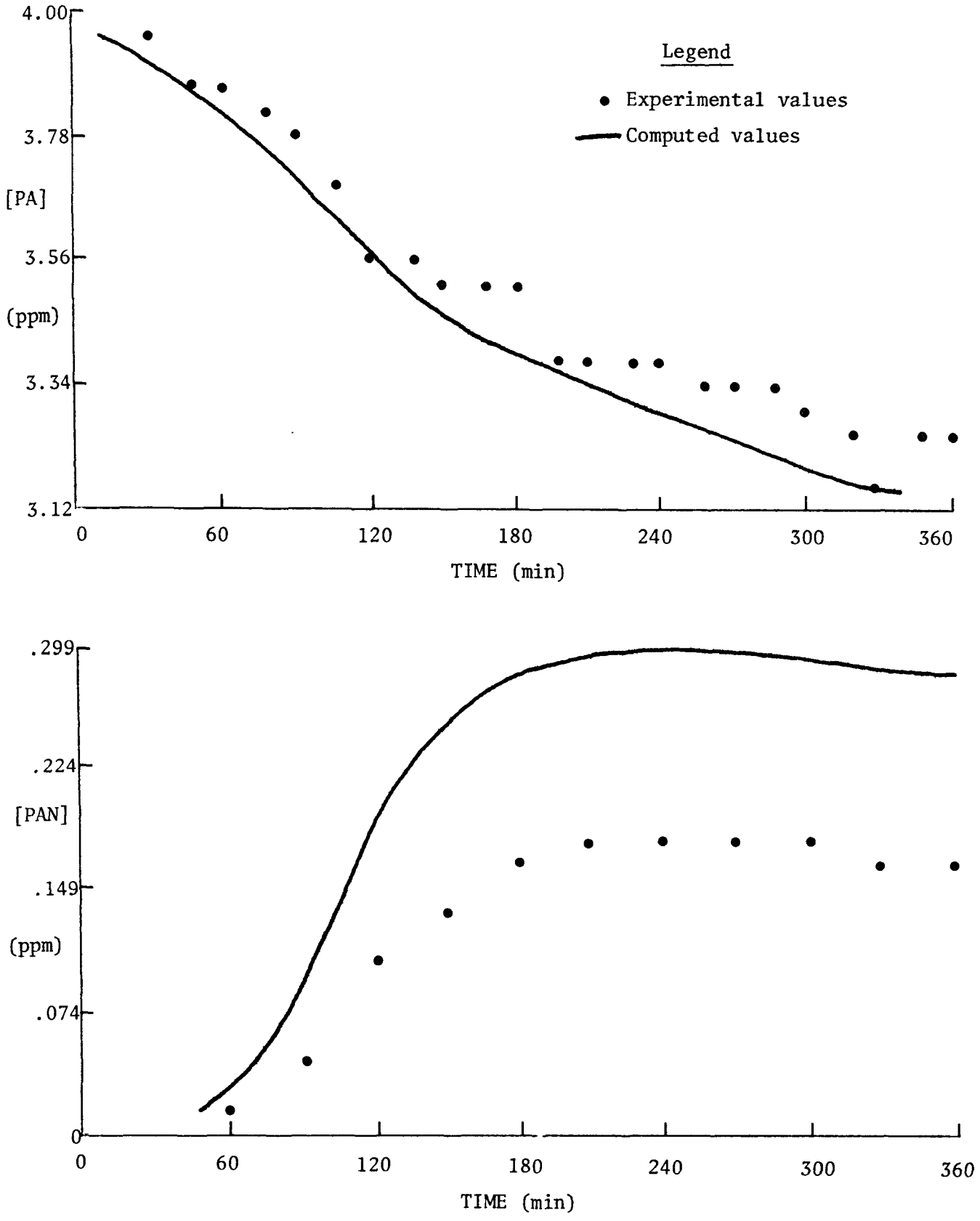

Figure 4-2 Simulation of Smog Chamber Experiment EC 116
(continued)

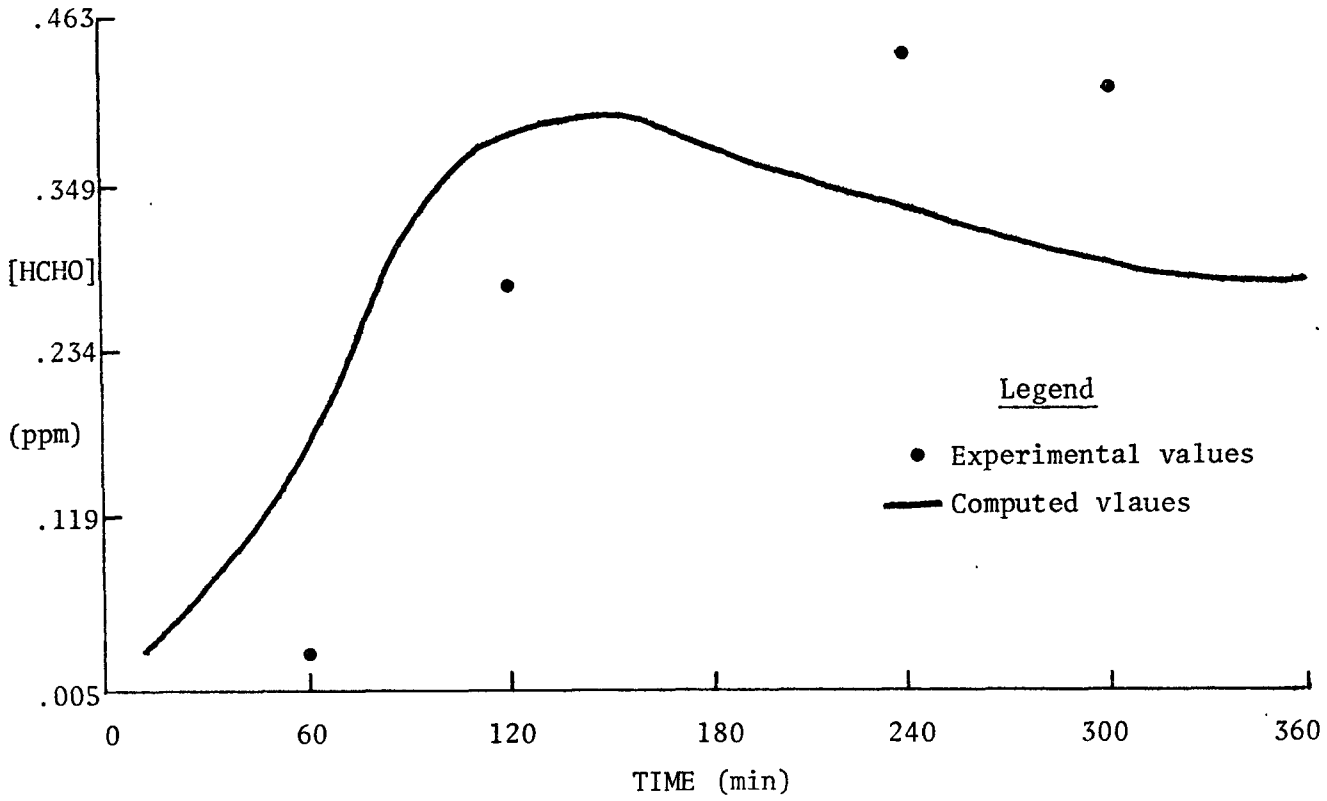

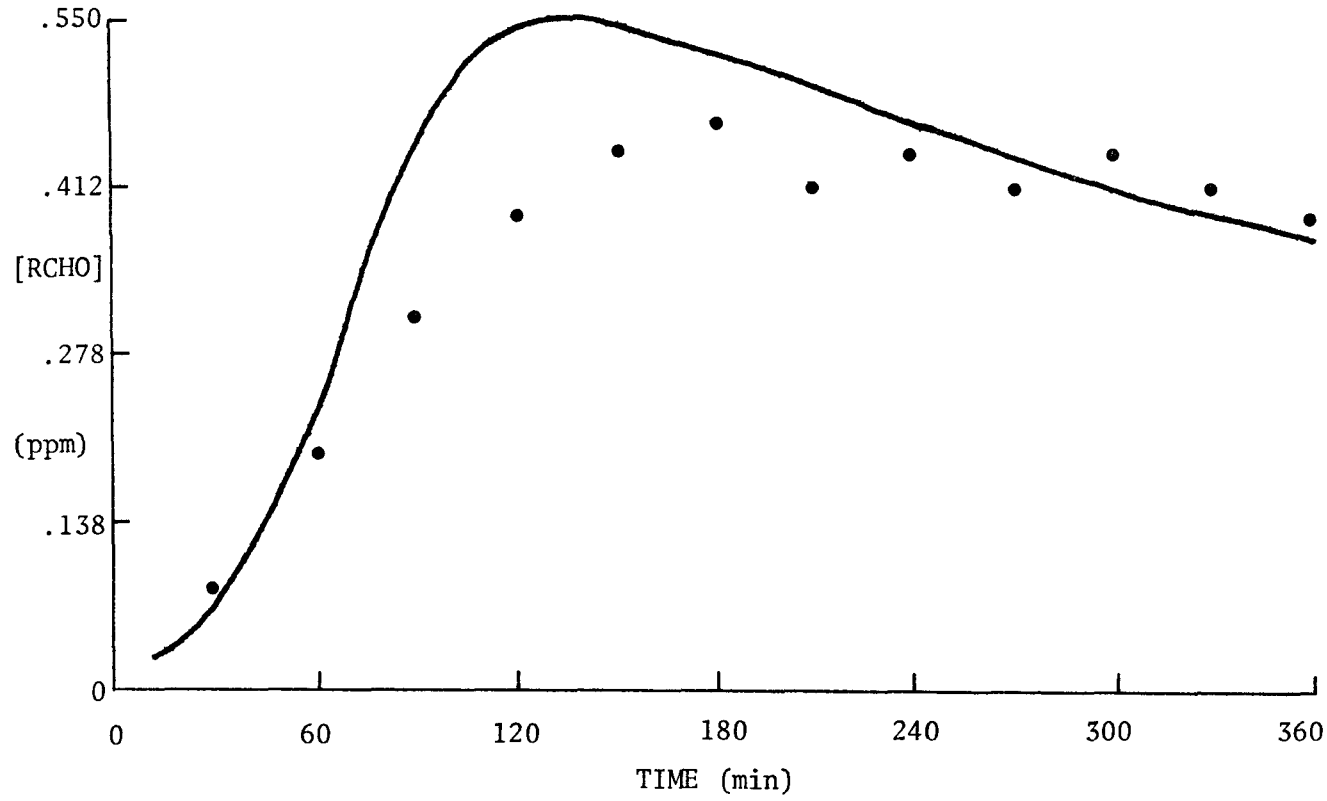

Figure 4-2 Simulation of Smog Chamber Experiment EC 116
(continued)

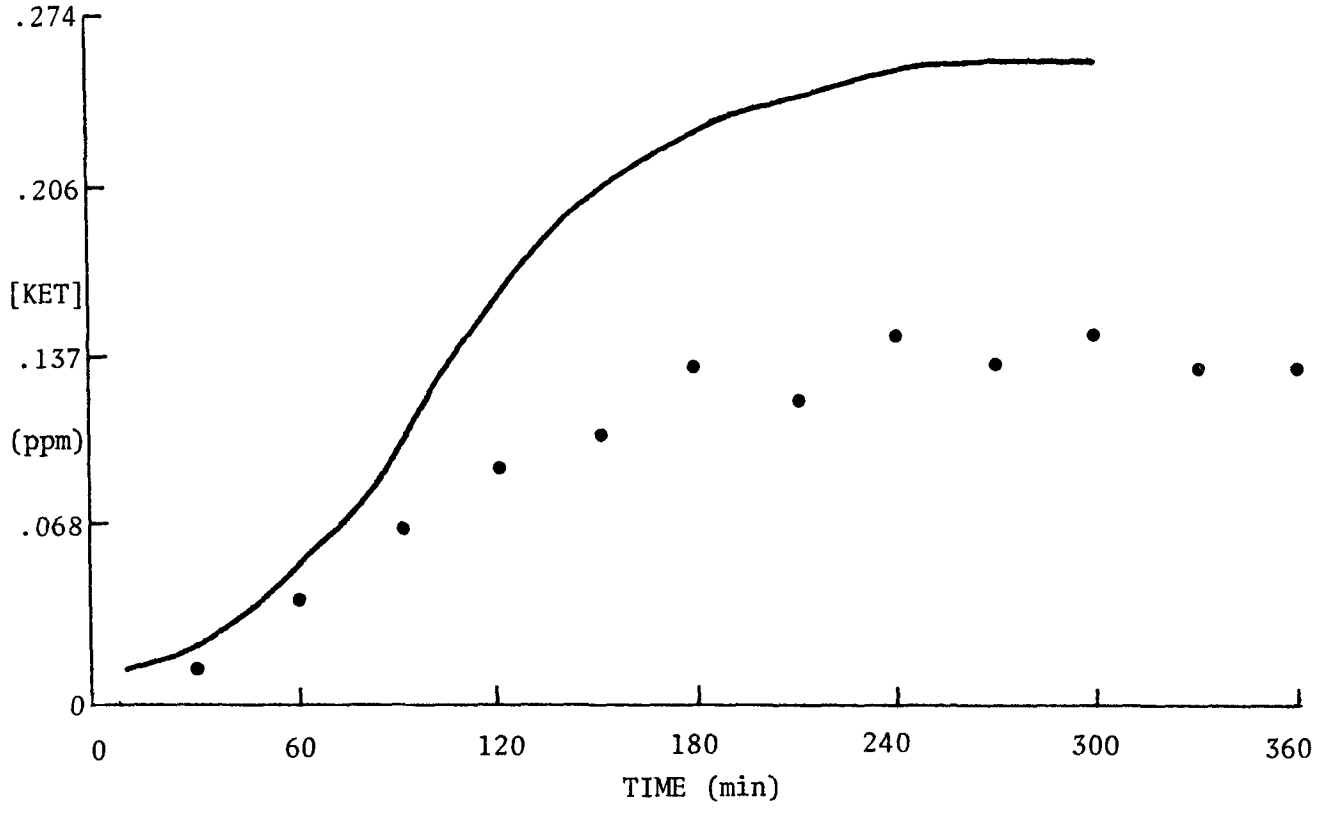

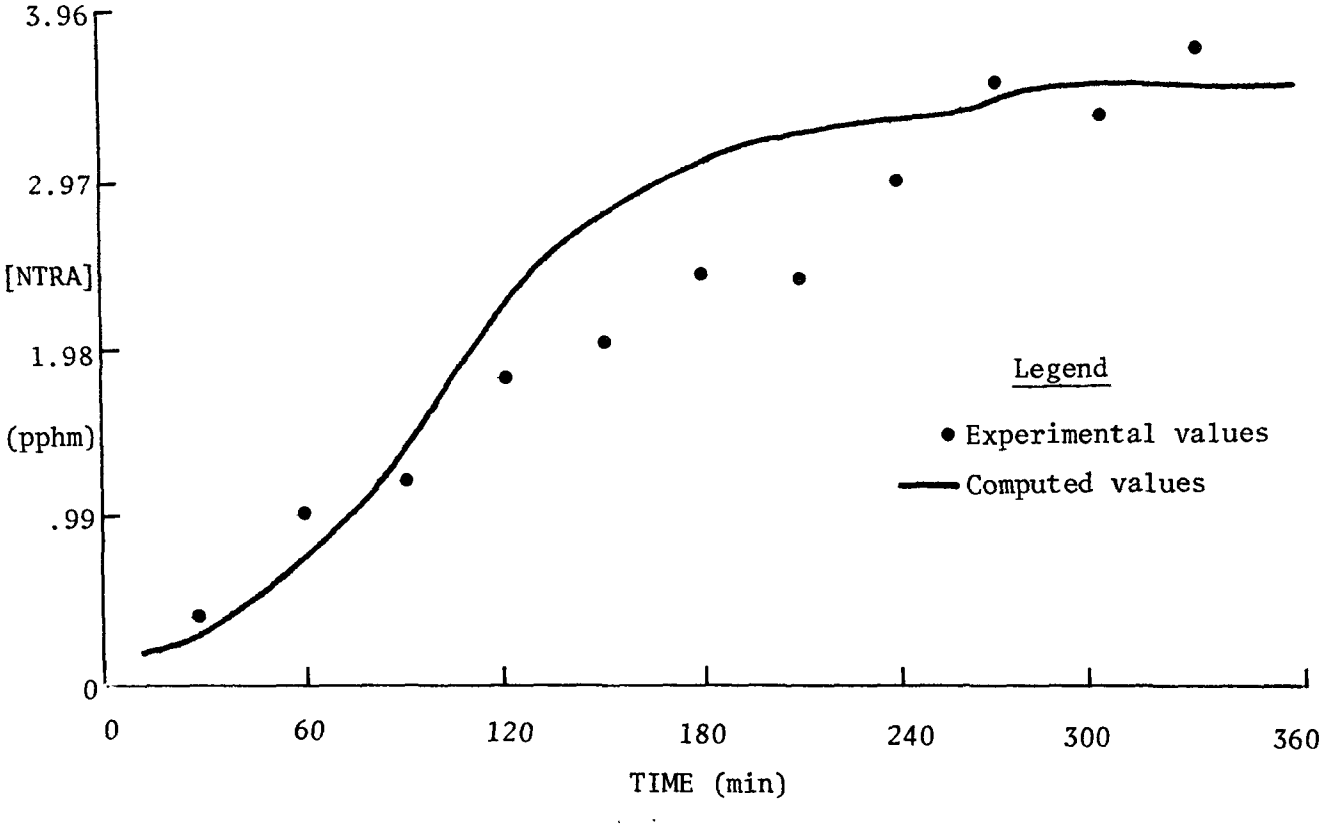

Figure 4-3 Simulation of Smog Chamber Experiment GC 119

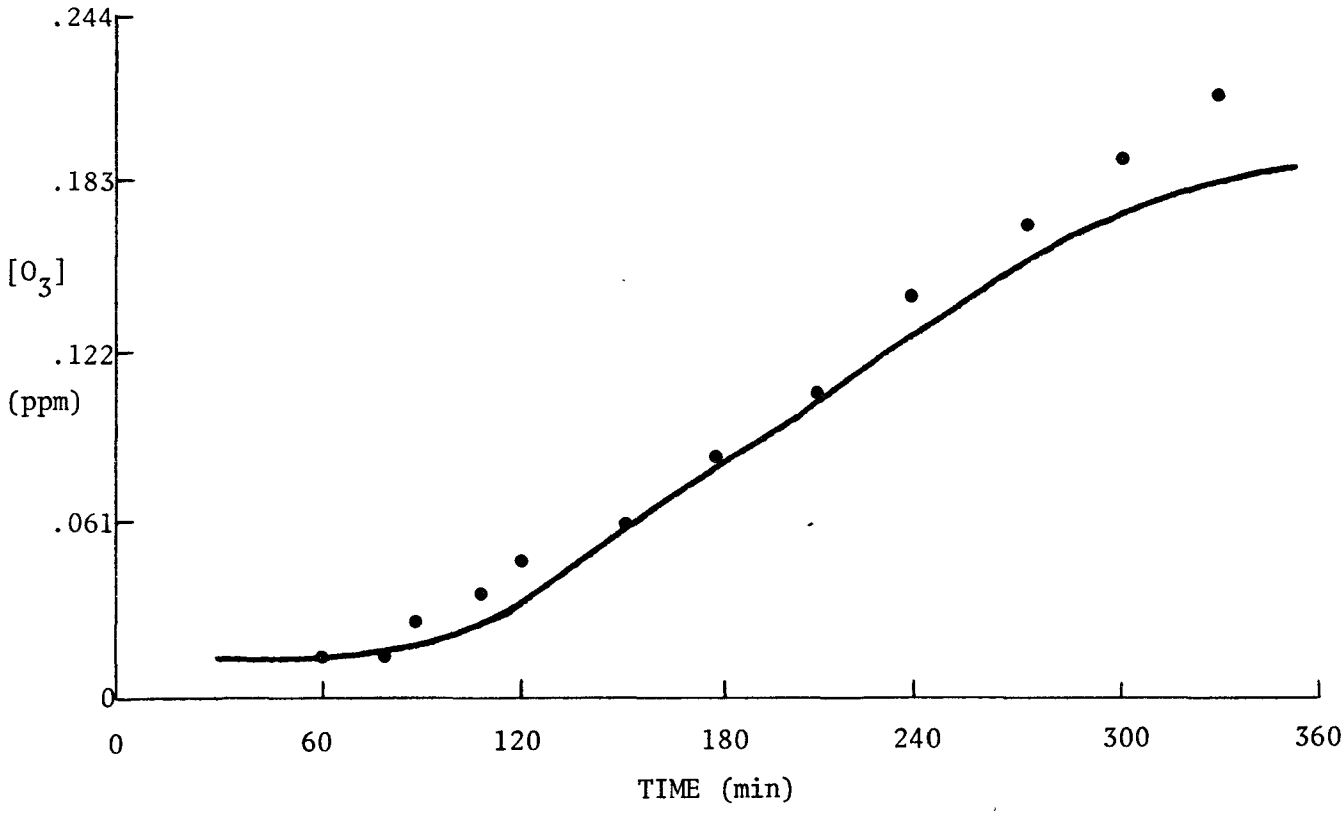

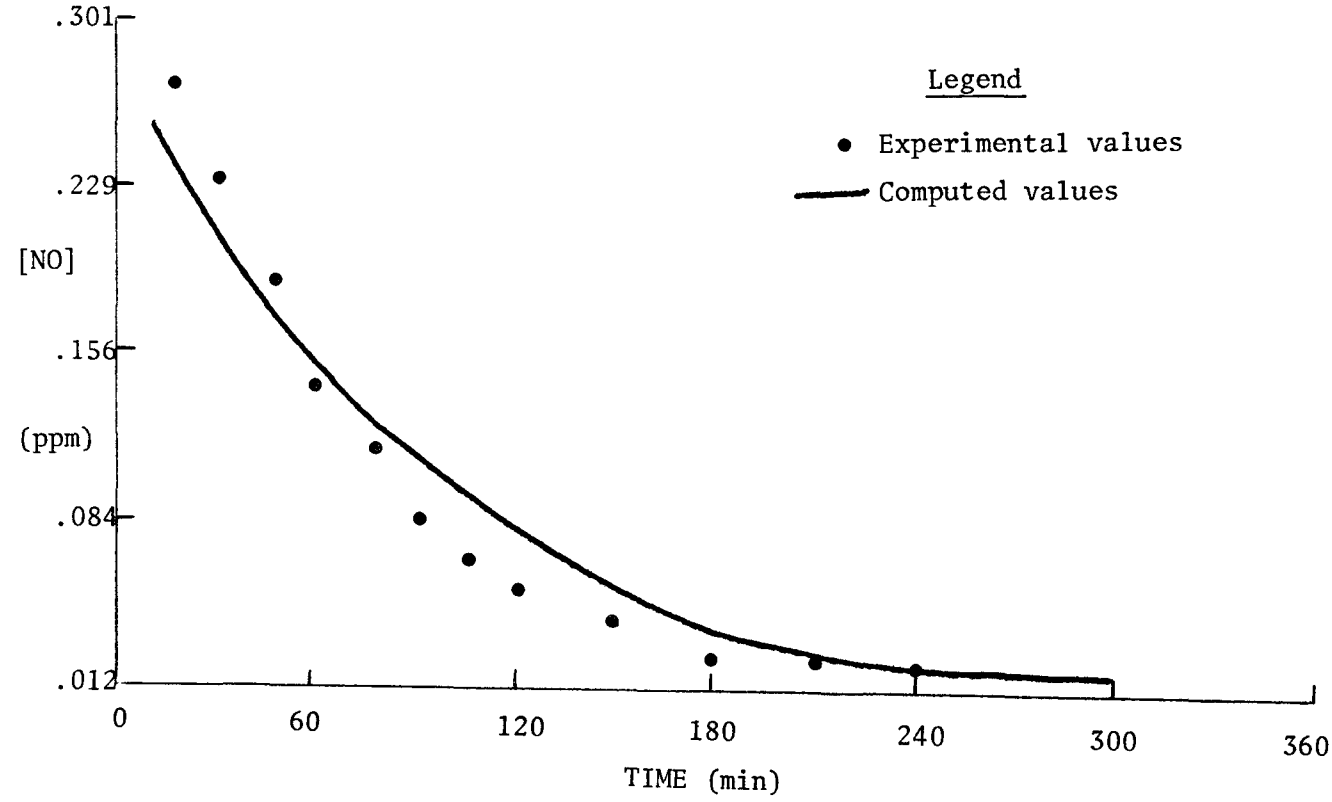

Figure 4-3 Simulation of Smog Chamber Experiment GC 119
(continued)

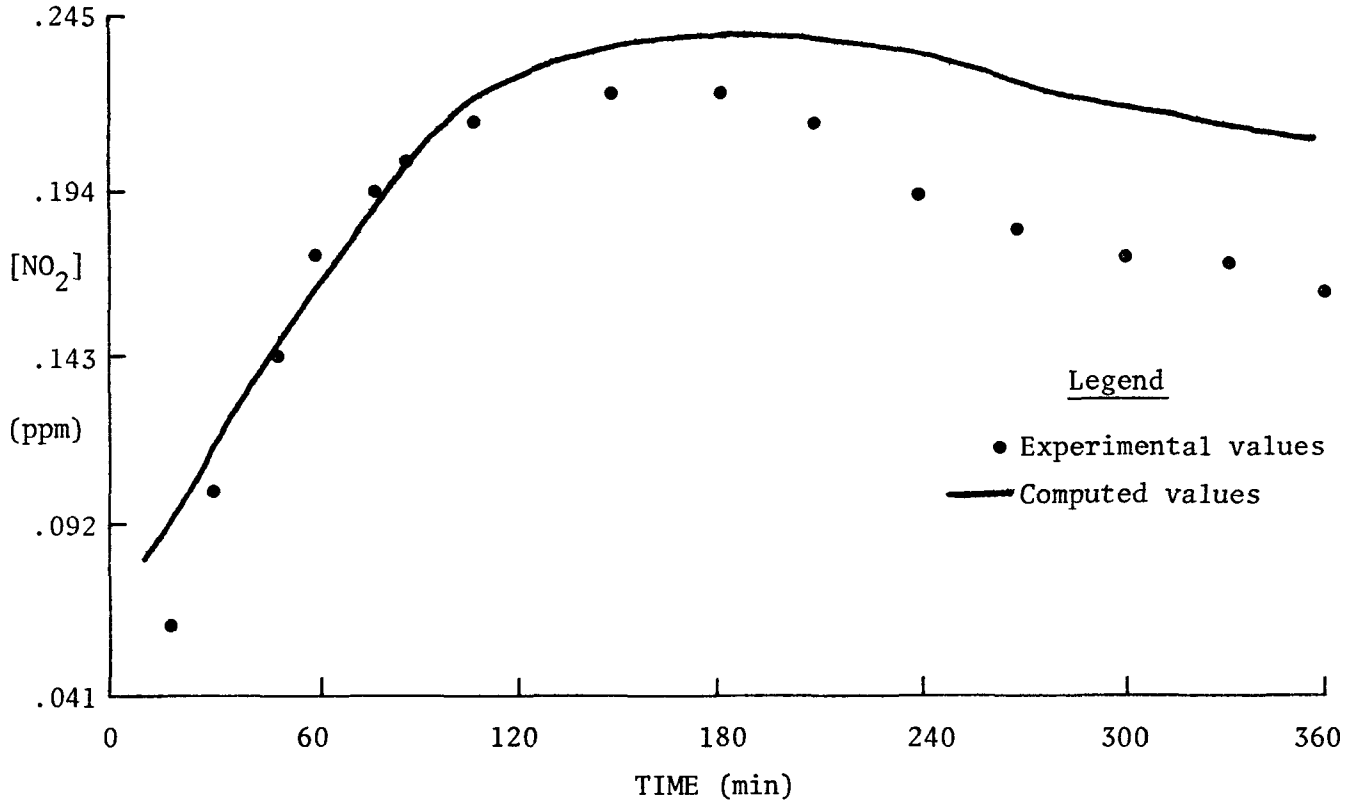

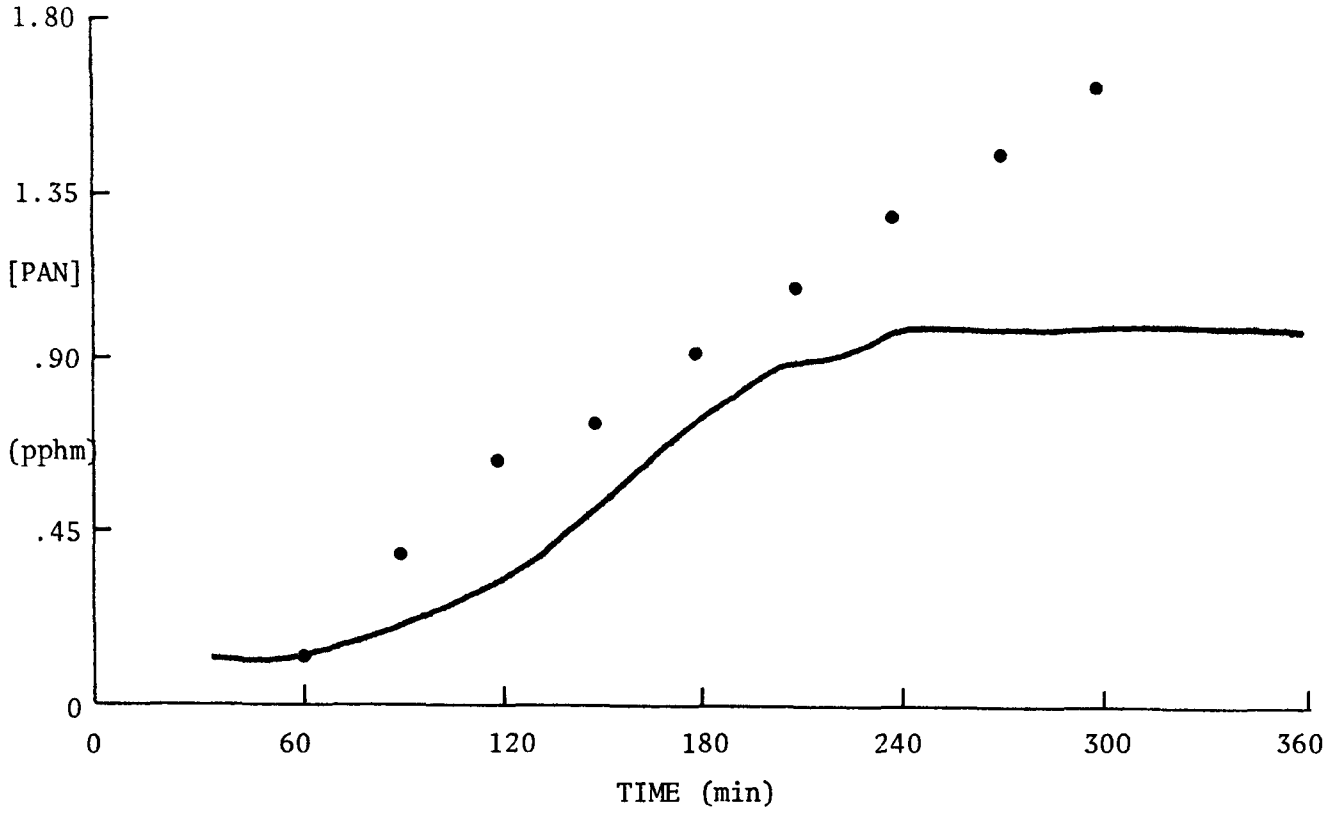

Figure 4-3 Simulation of Smog Chamber Experiment GC 119
(continued)

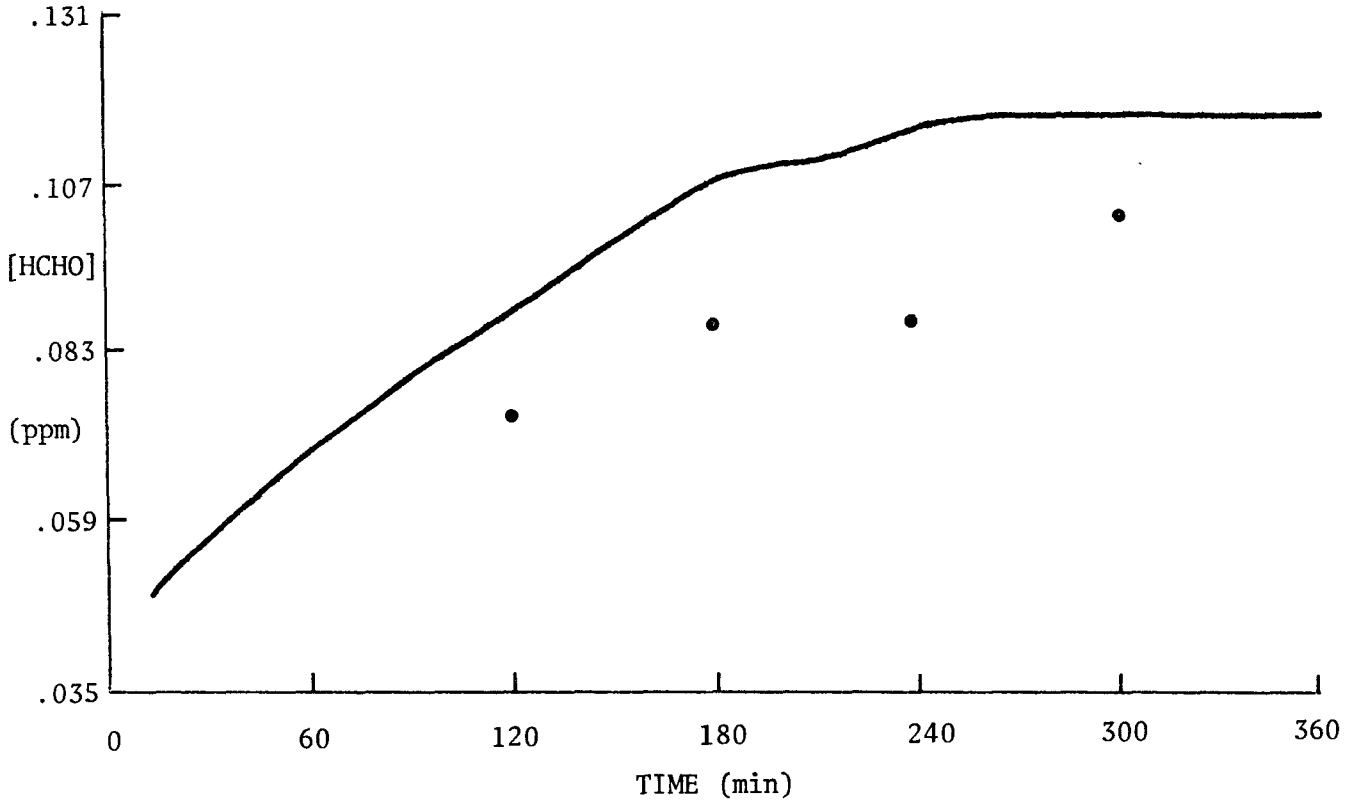

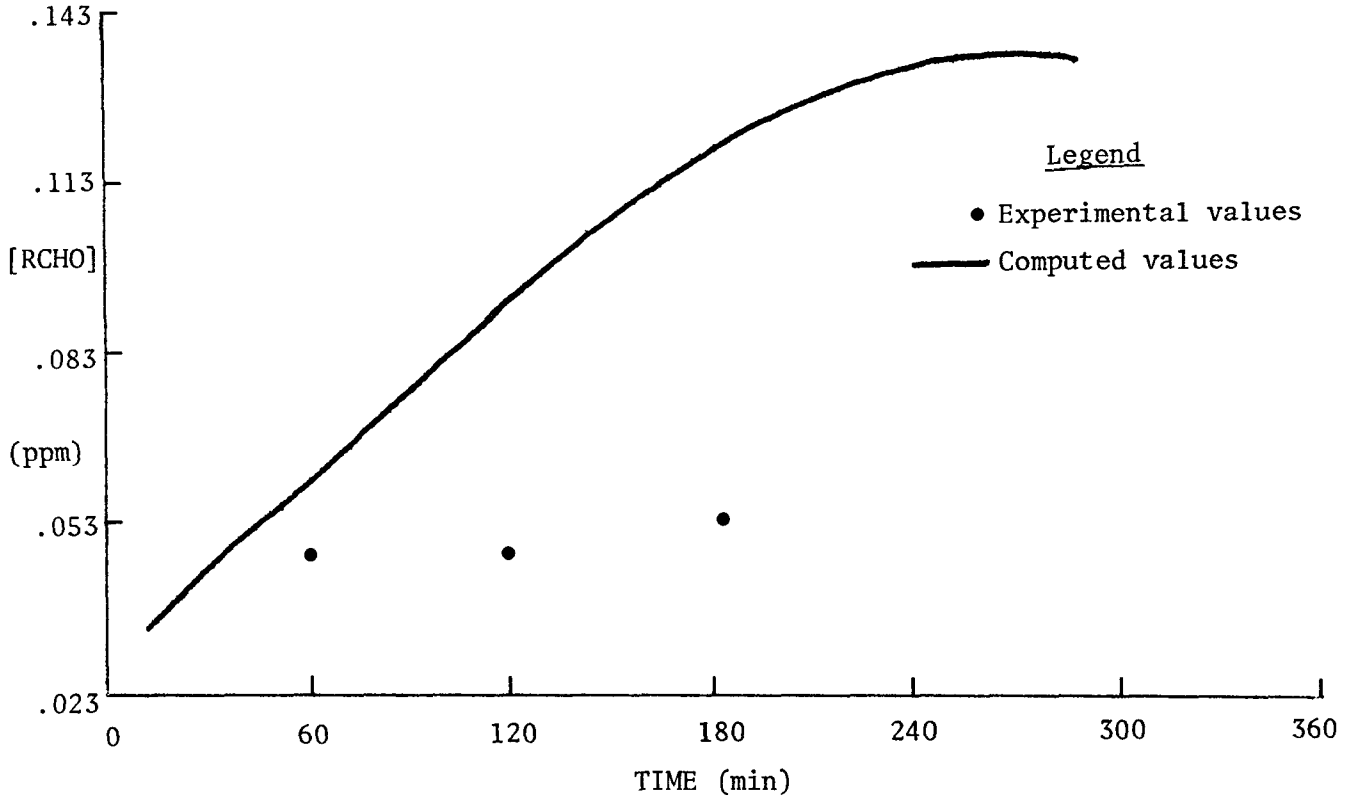

Figure 4-4 Simulation of Smog Chamber Experiment GC 133

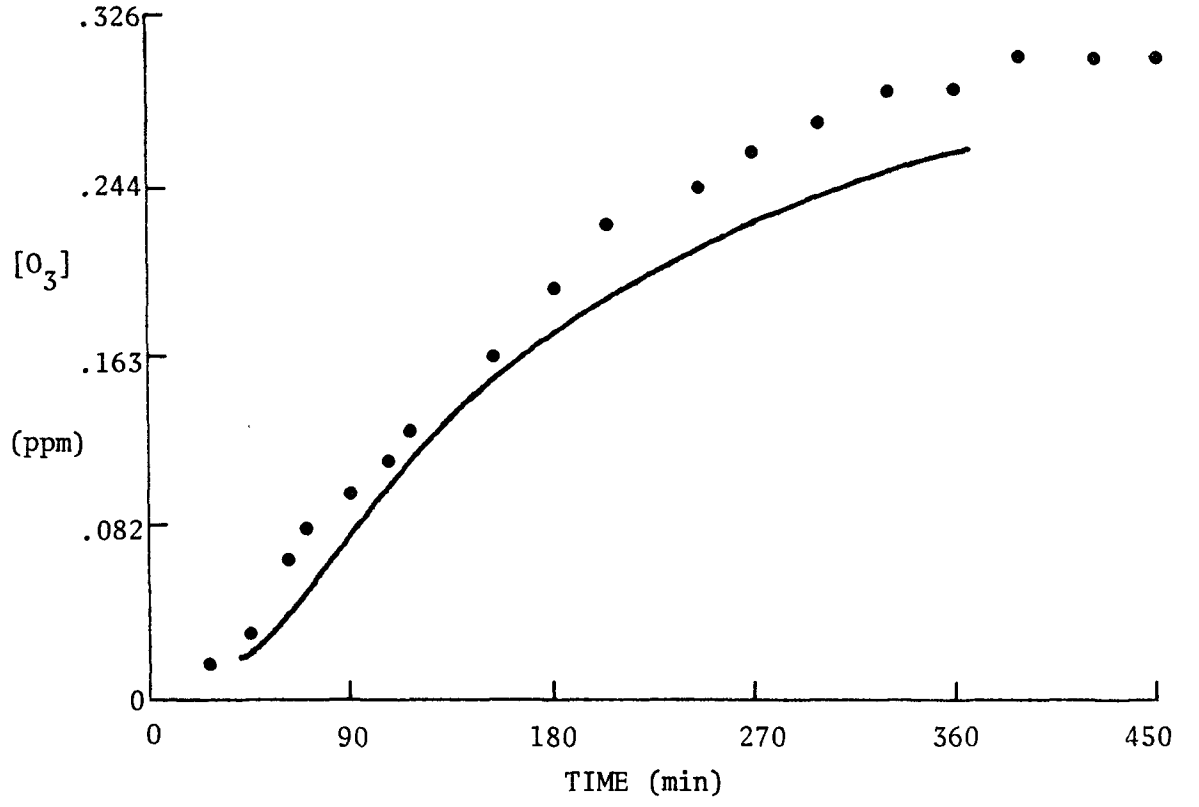

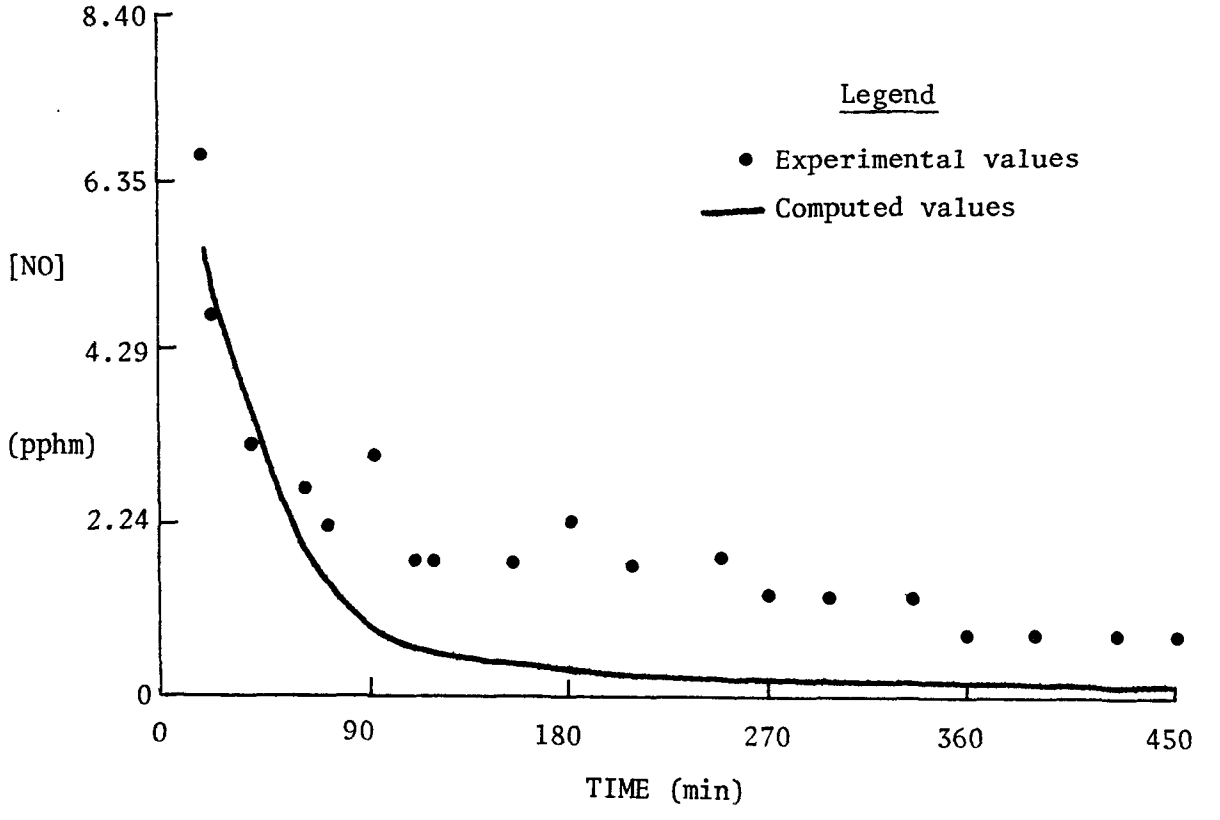

Figure 4-4 Simulation of Smog Chamber Experiment GC 133
(continued)

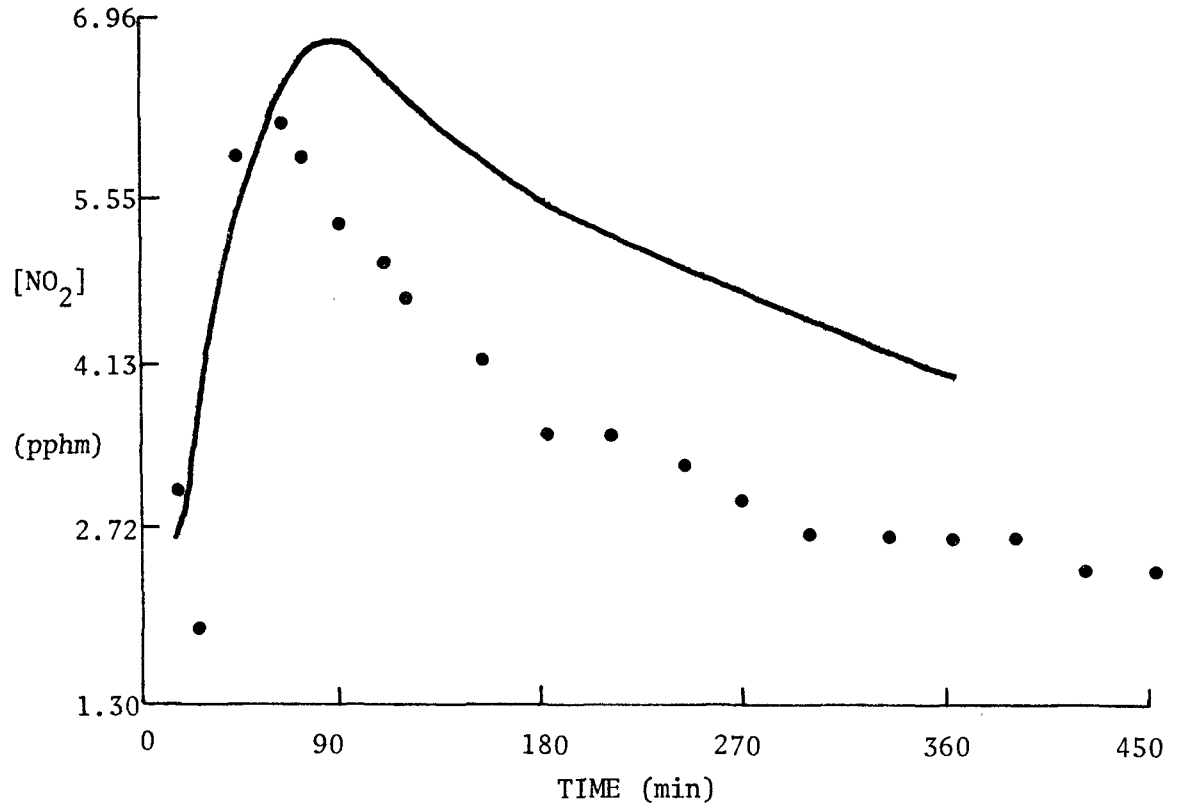

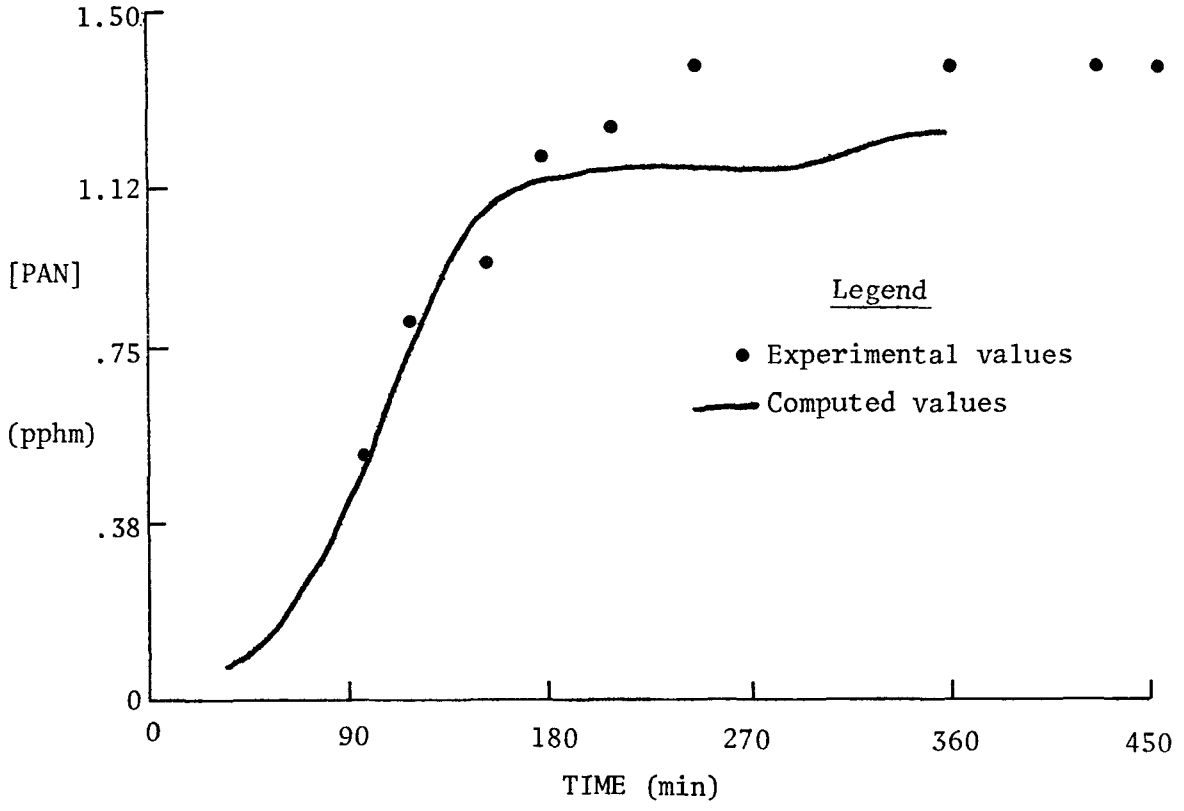

Figure 4-4 Simulation of Smog Chamber Experiment GC 133
(continued)

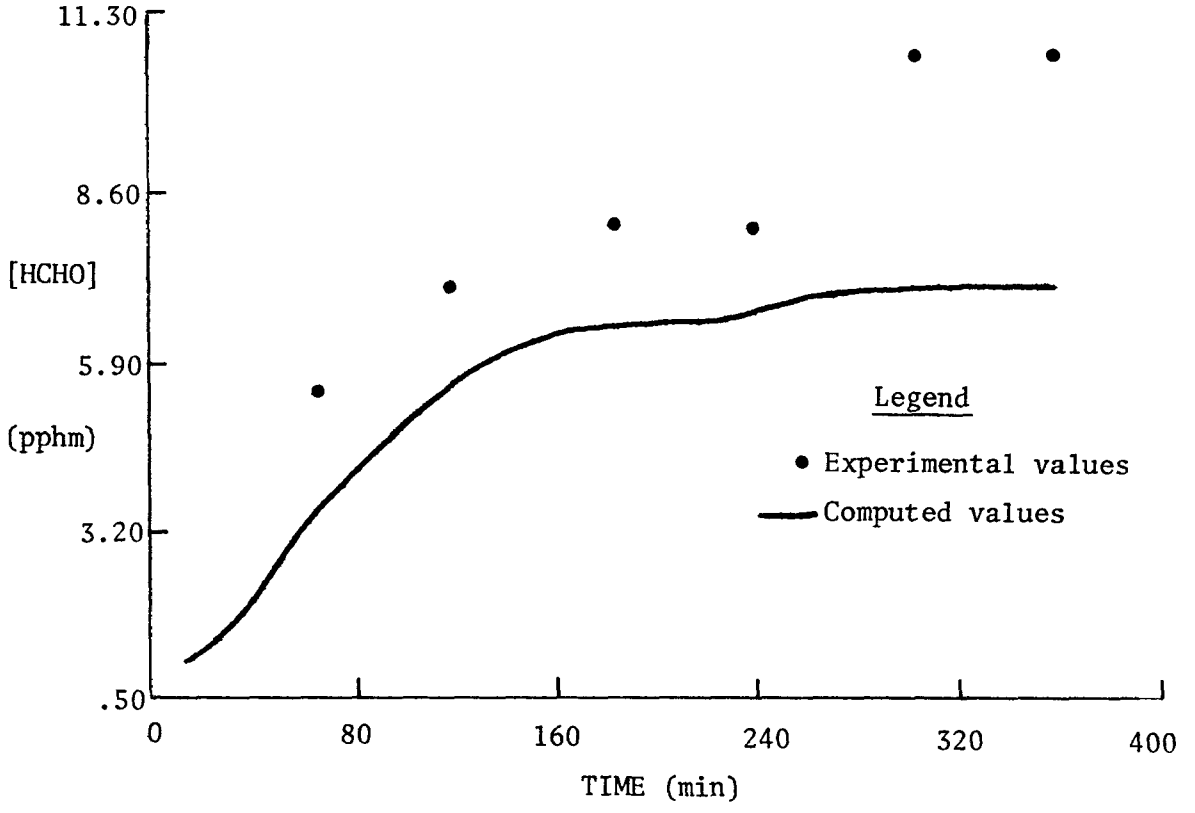

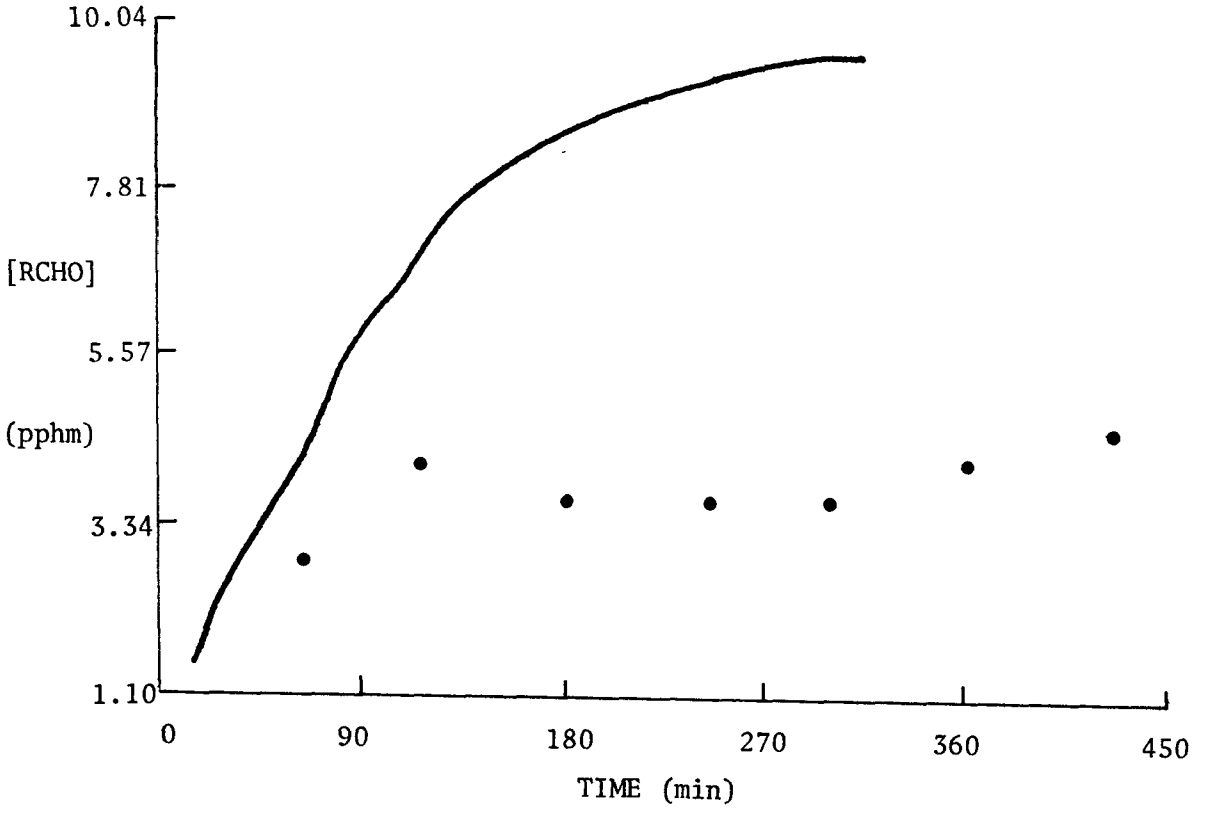

Figure 4-5 Simulation of Smog Chamber Experiment GC 135

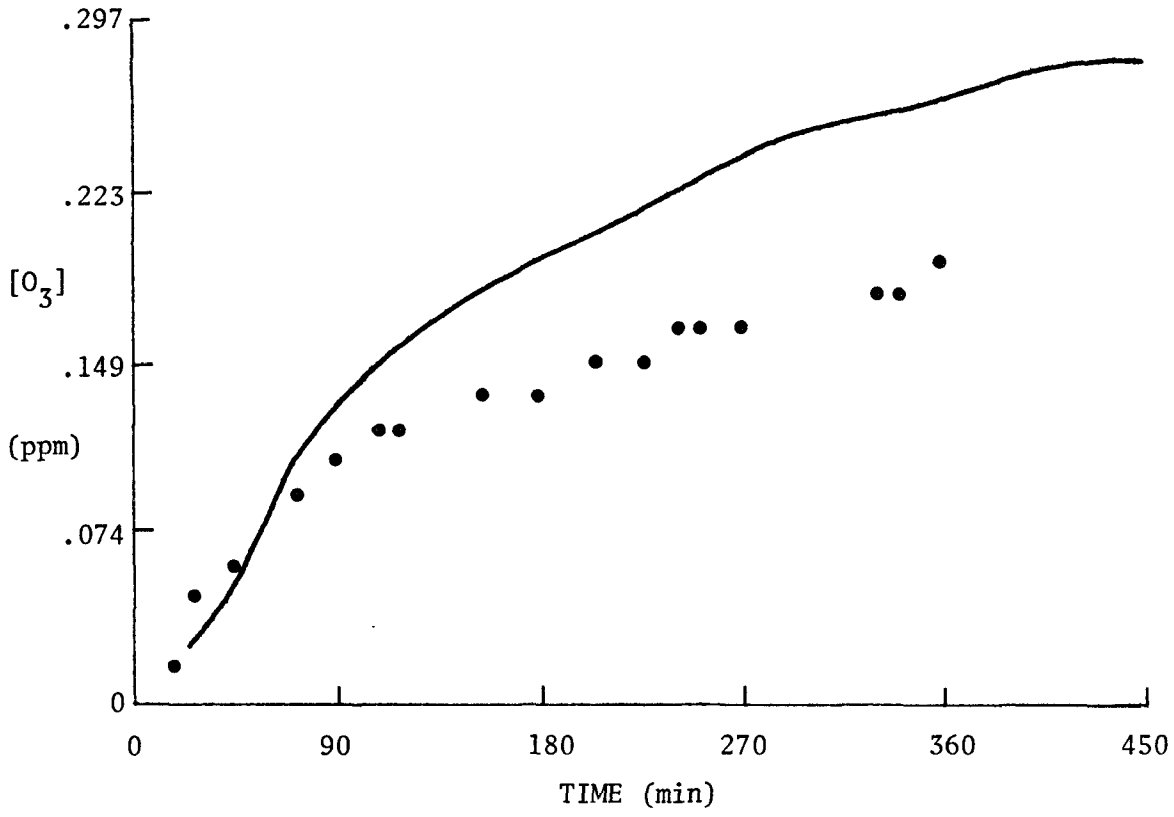

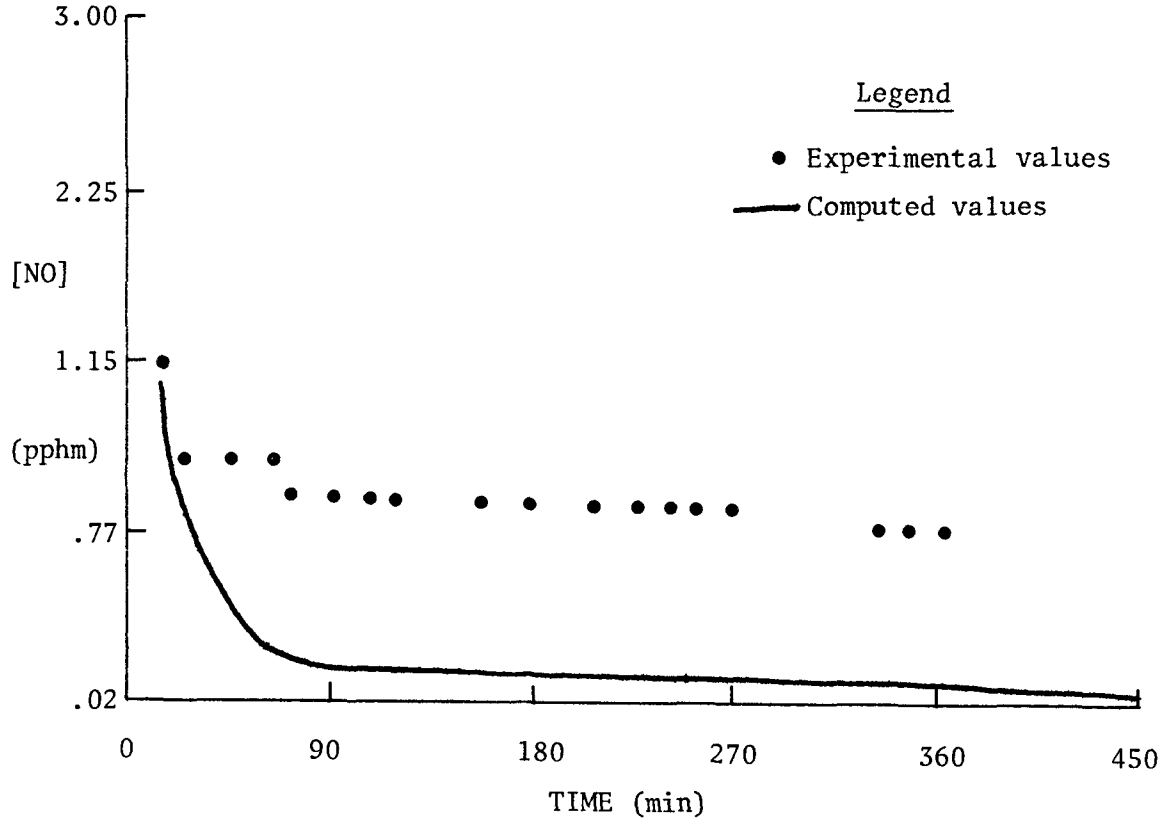

Figure 4-5 Simulation of Smog Chamber Experiment GC 135
(continued)

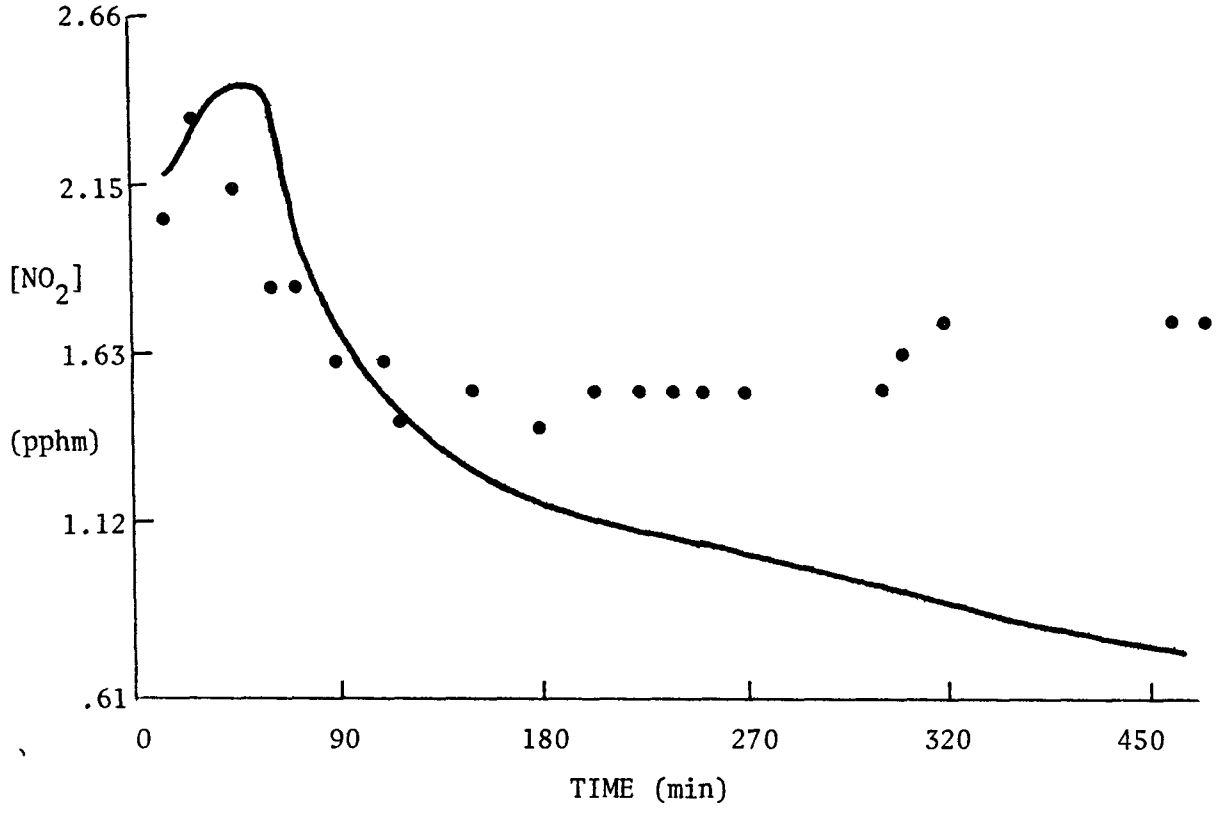

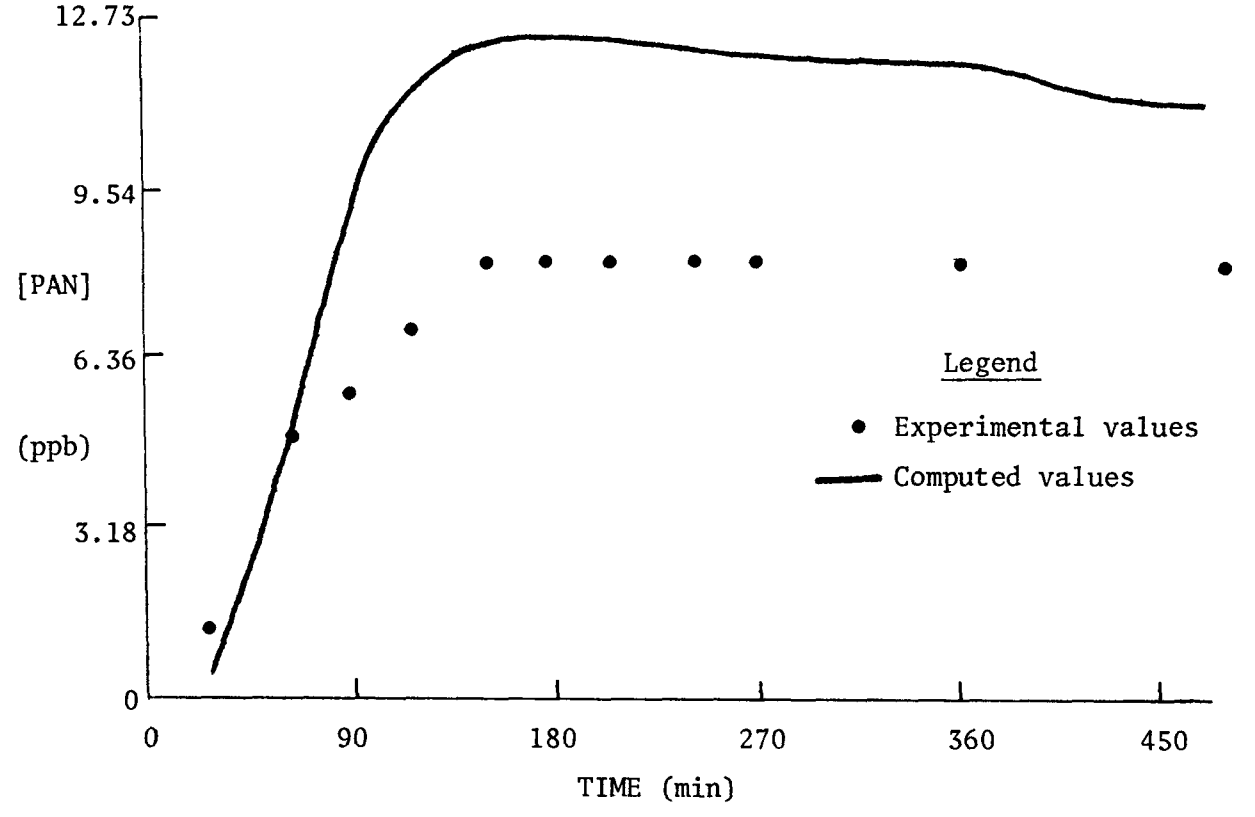

Figure 4-5 Simulation of Smog Chamber Experiment GC 135
(continued)

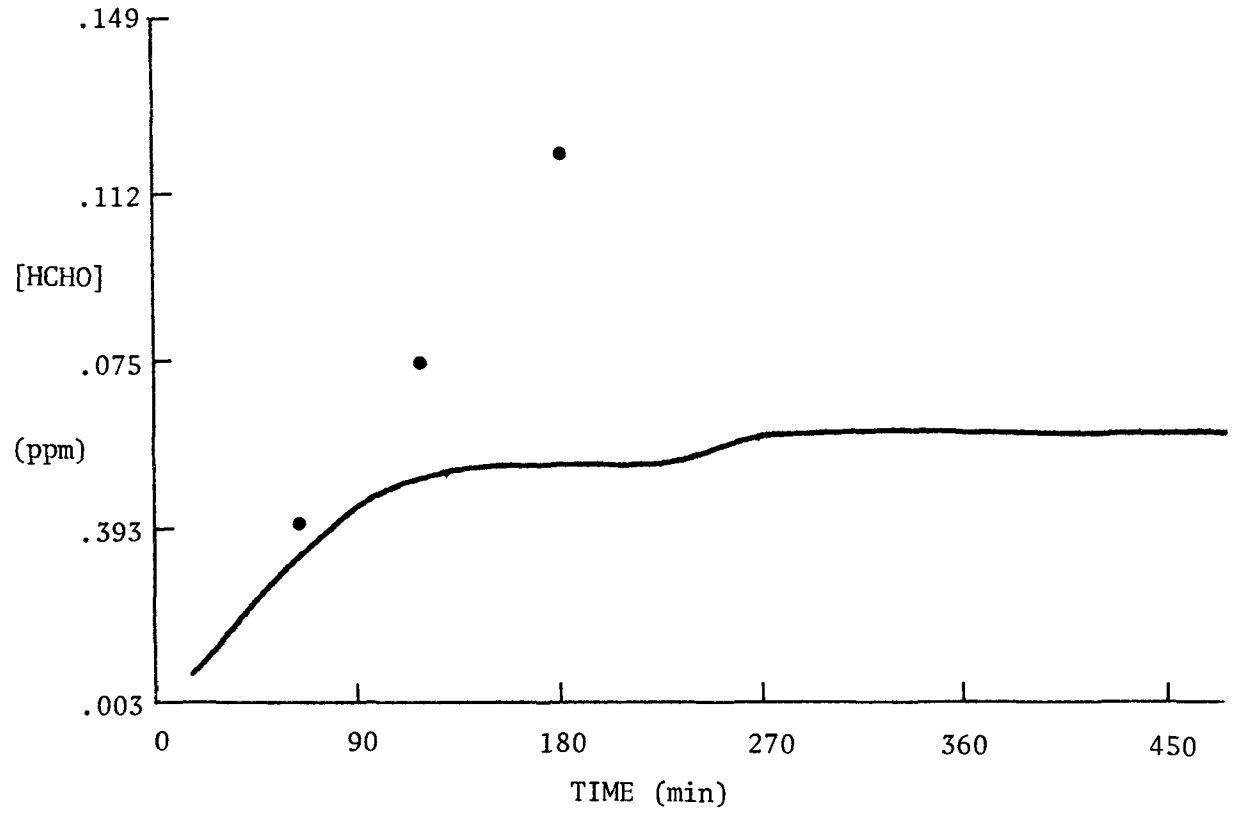

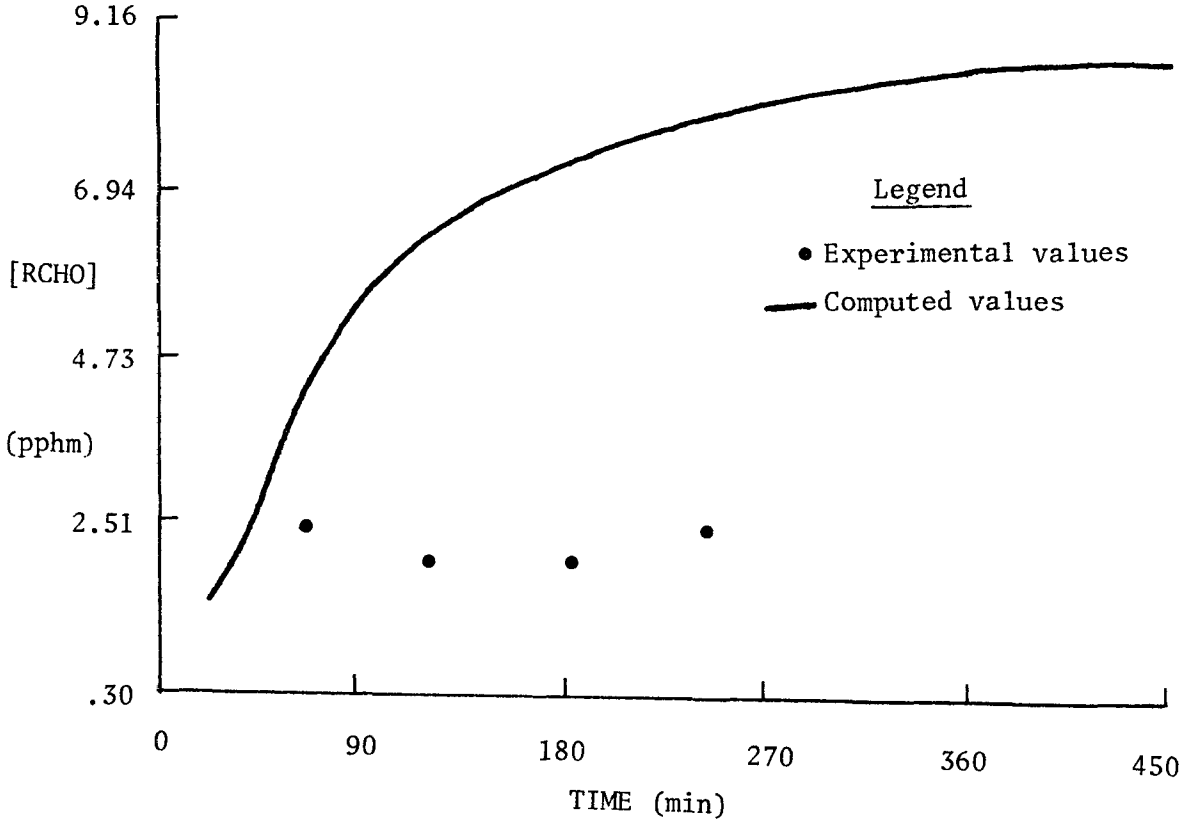

Figure 4-6 Simulation of Smog Chamber Experiment GC 138

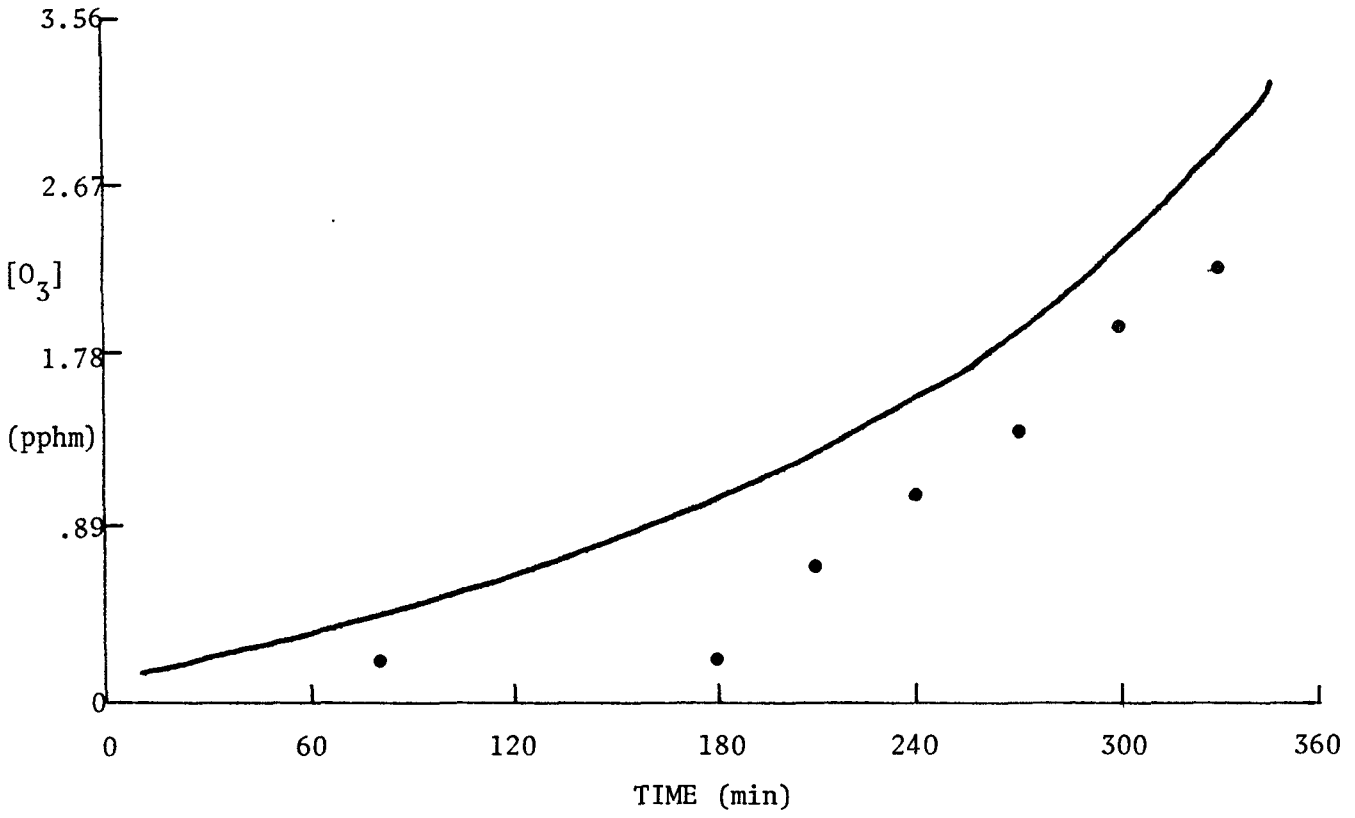

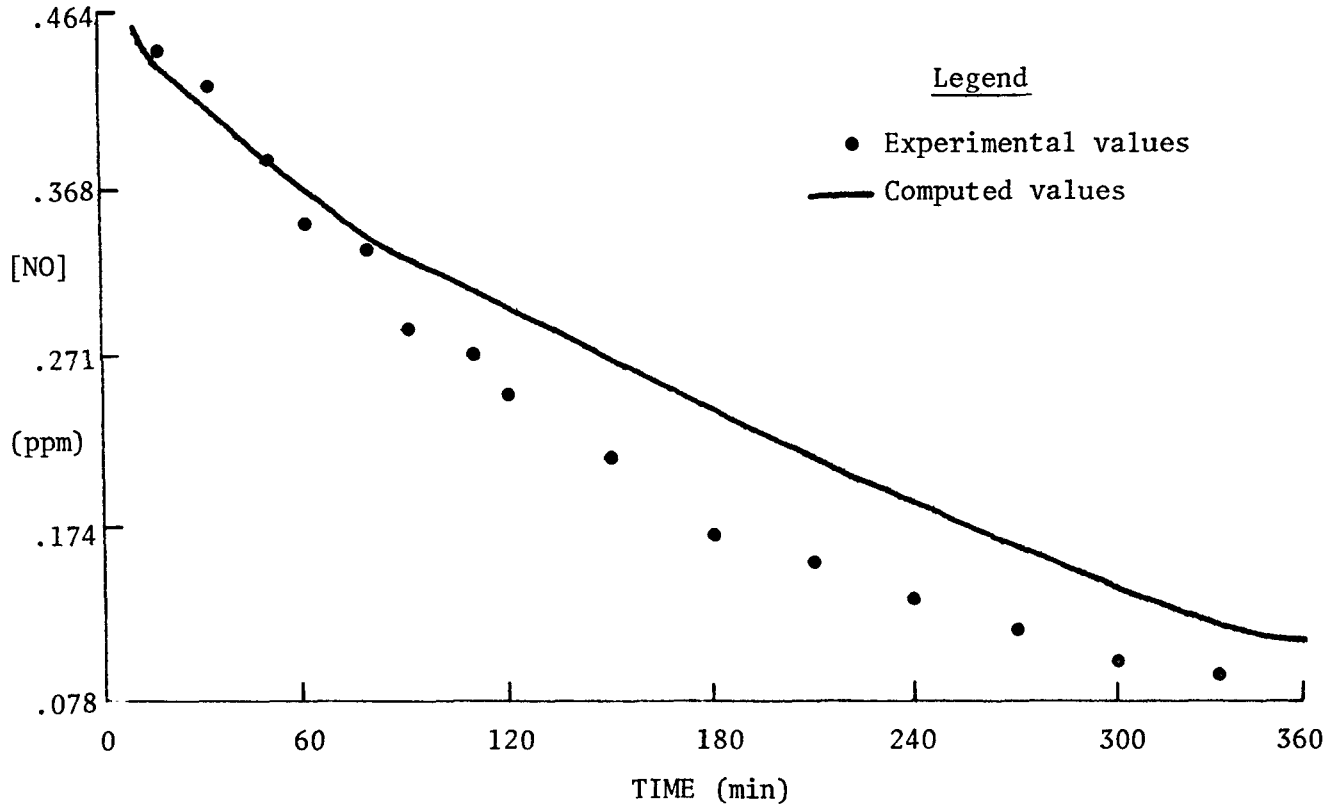

Figure 4-6 Simulation of Smog Chamber Experiment GC 138
(continued)

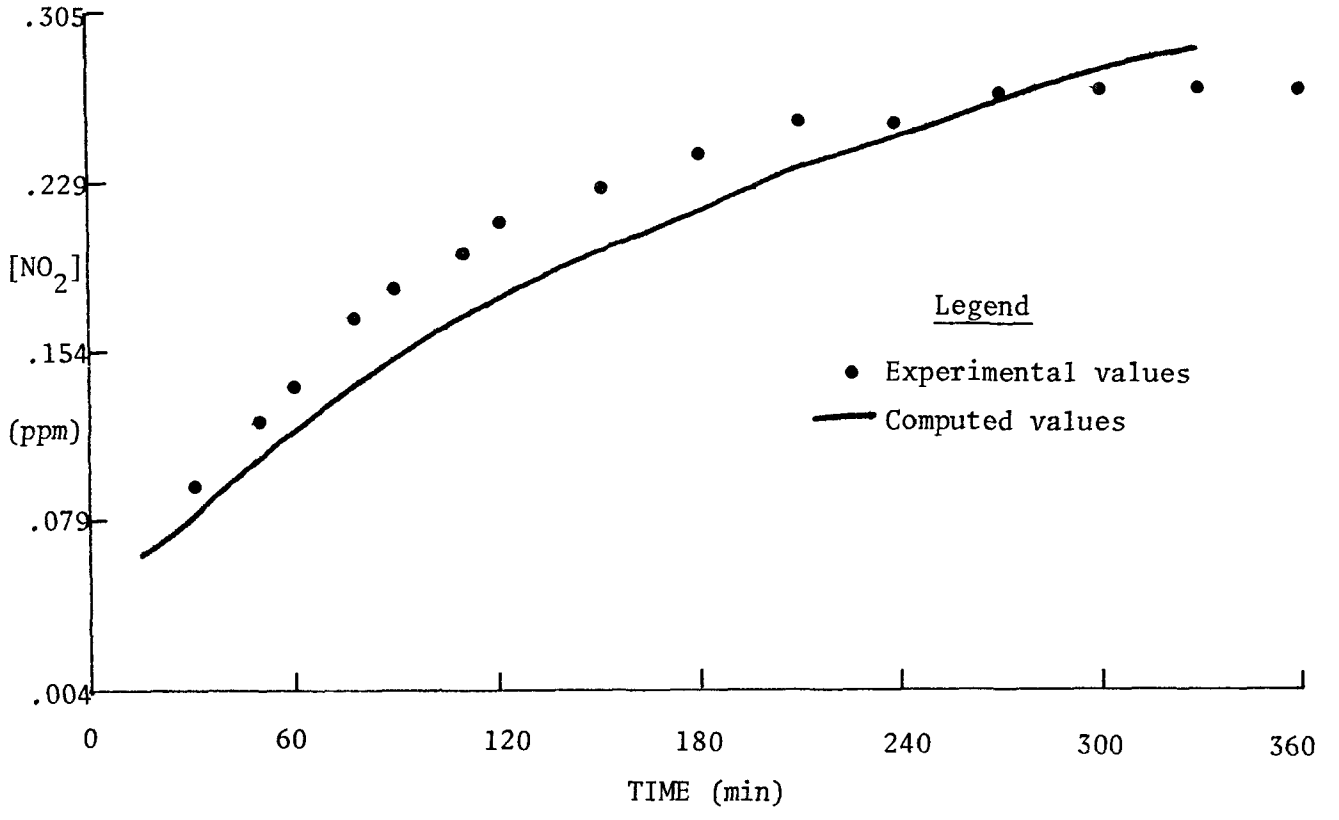

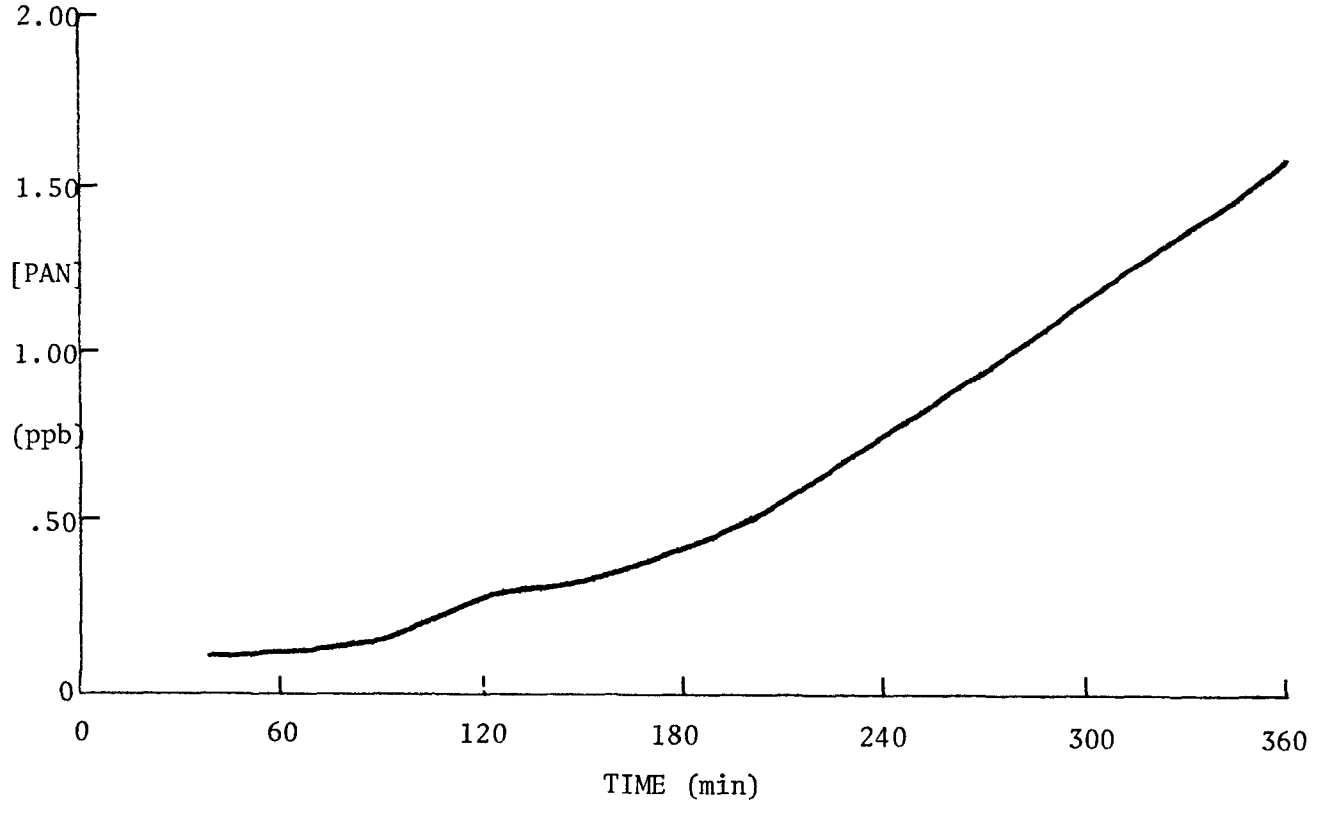

Figure 4-6 Simulation of Smog Chamber Experiment GC 138
(continued)

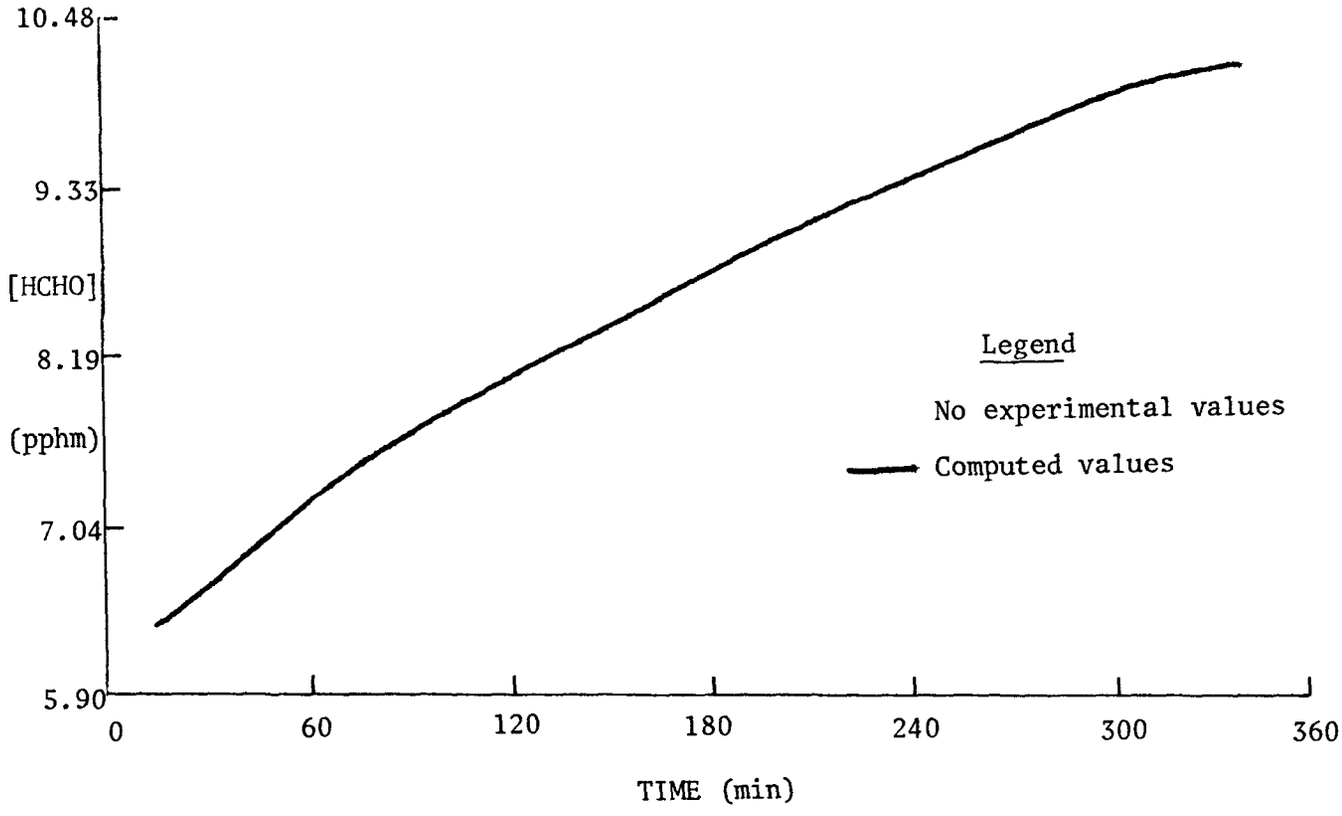

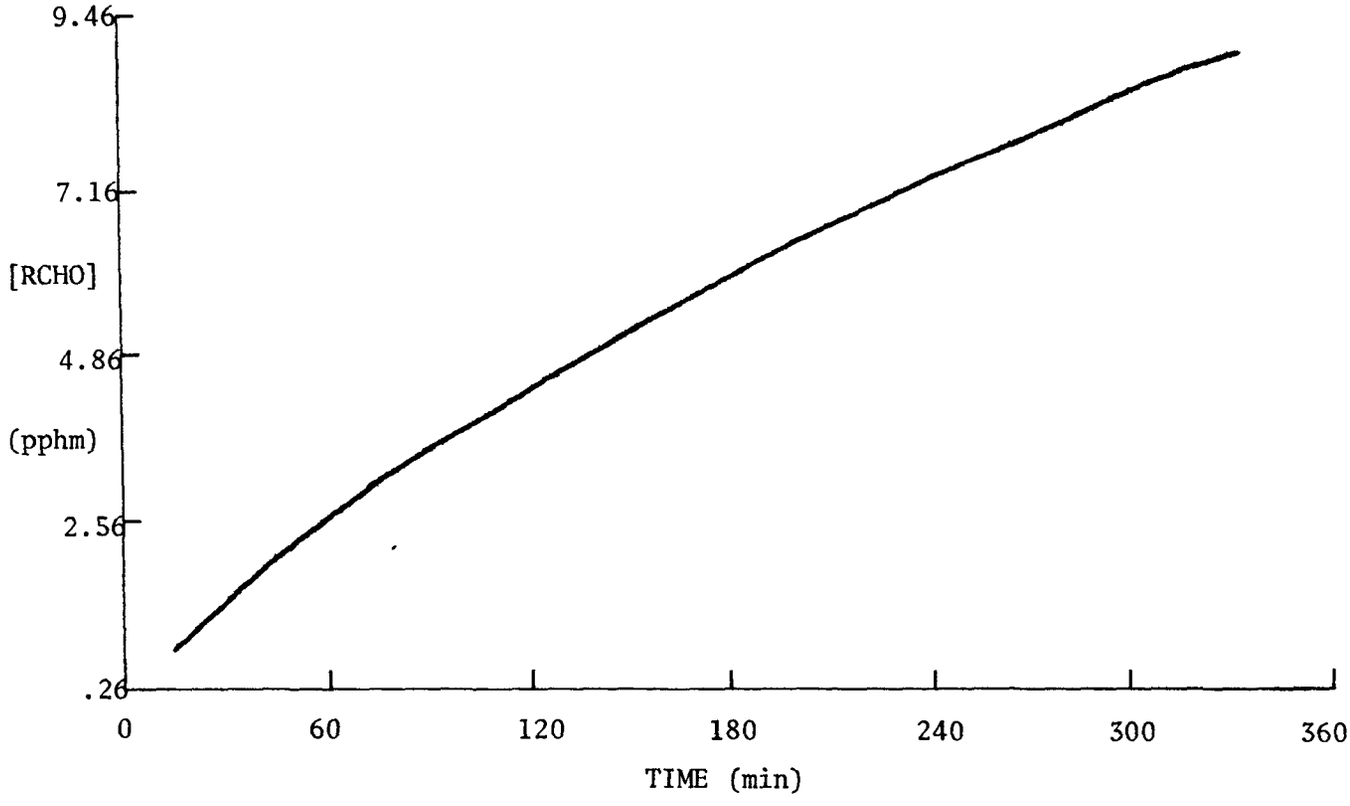

Figure 4-7 Simulation of Smog Chamber Experiment GC 150

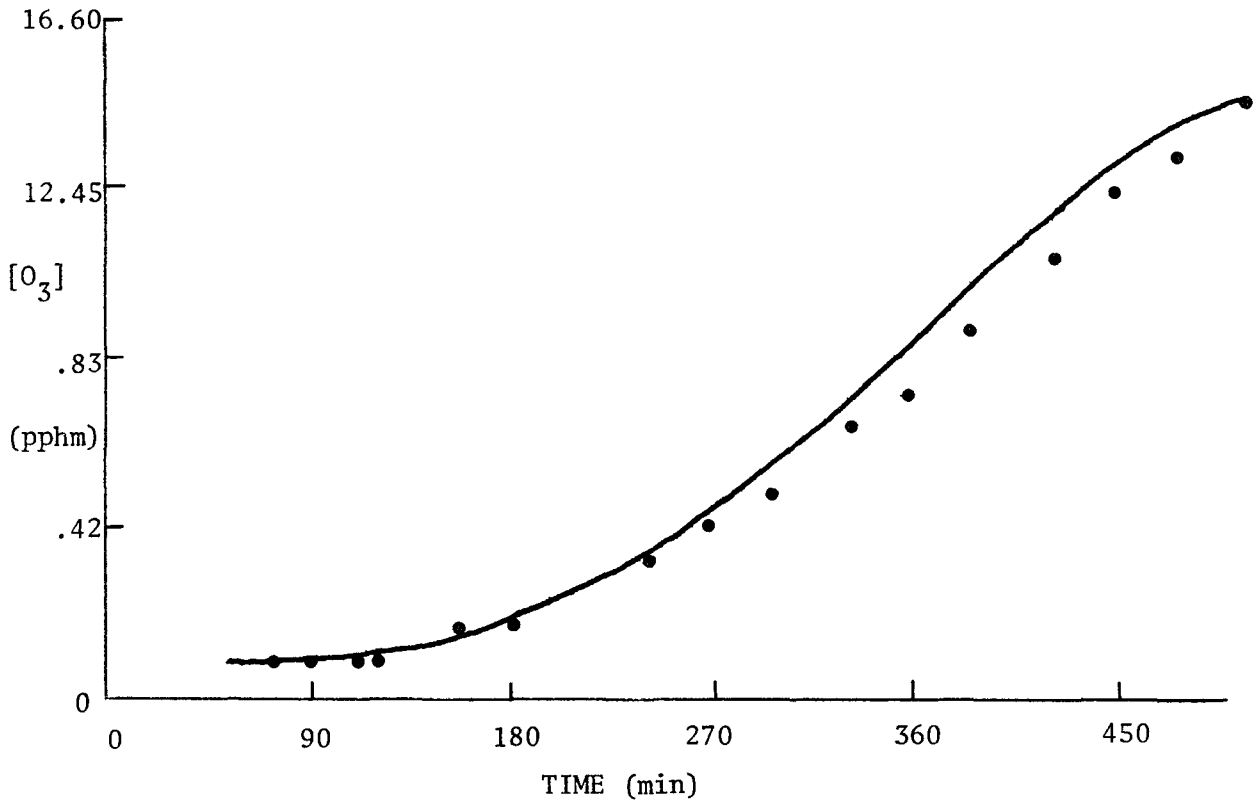

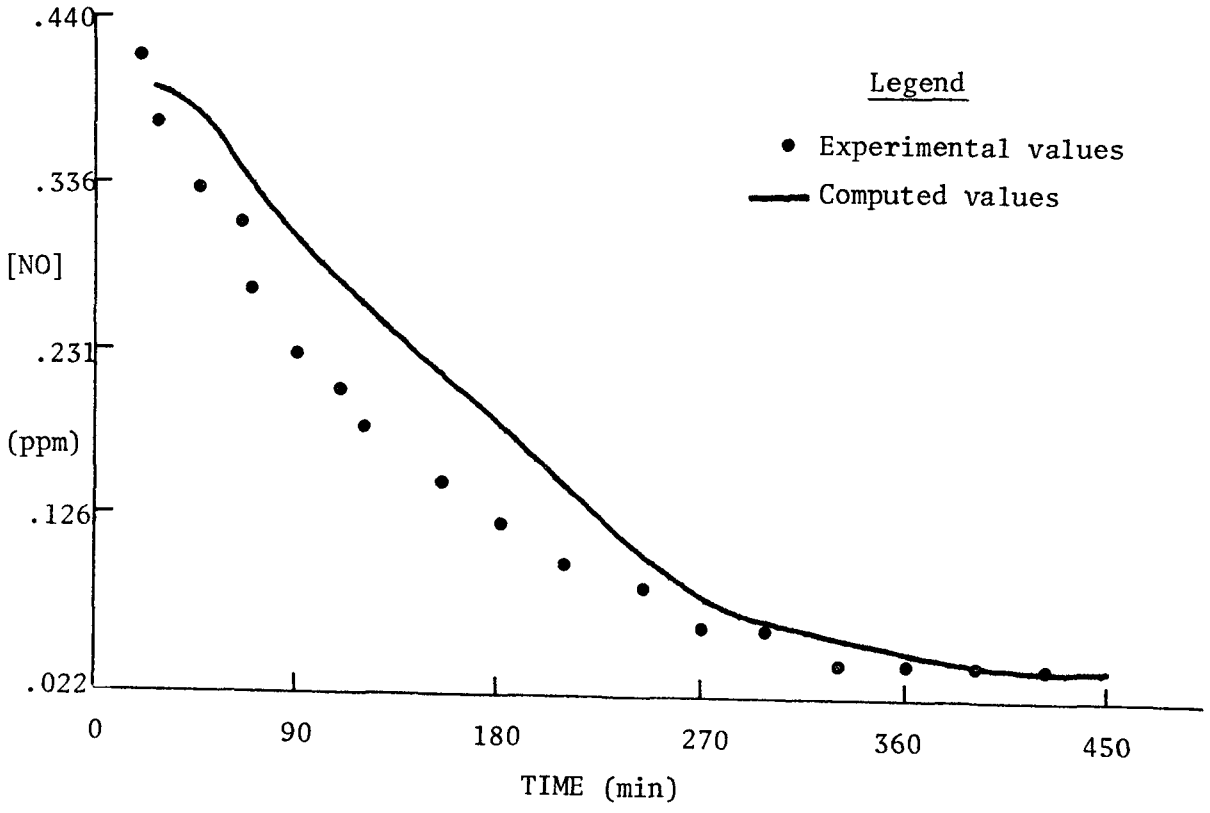

Figure 4-7 Simulation of Smog Chamber Experiment GC 150
(continued)

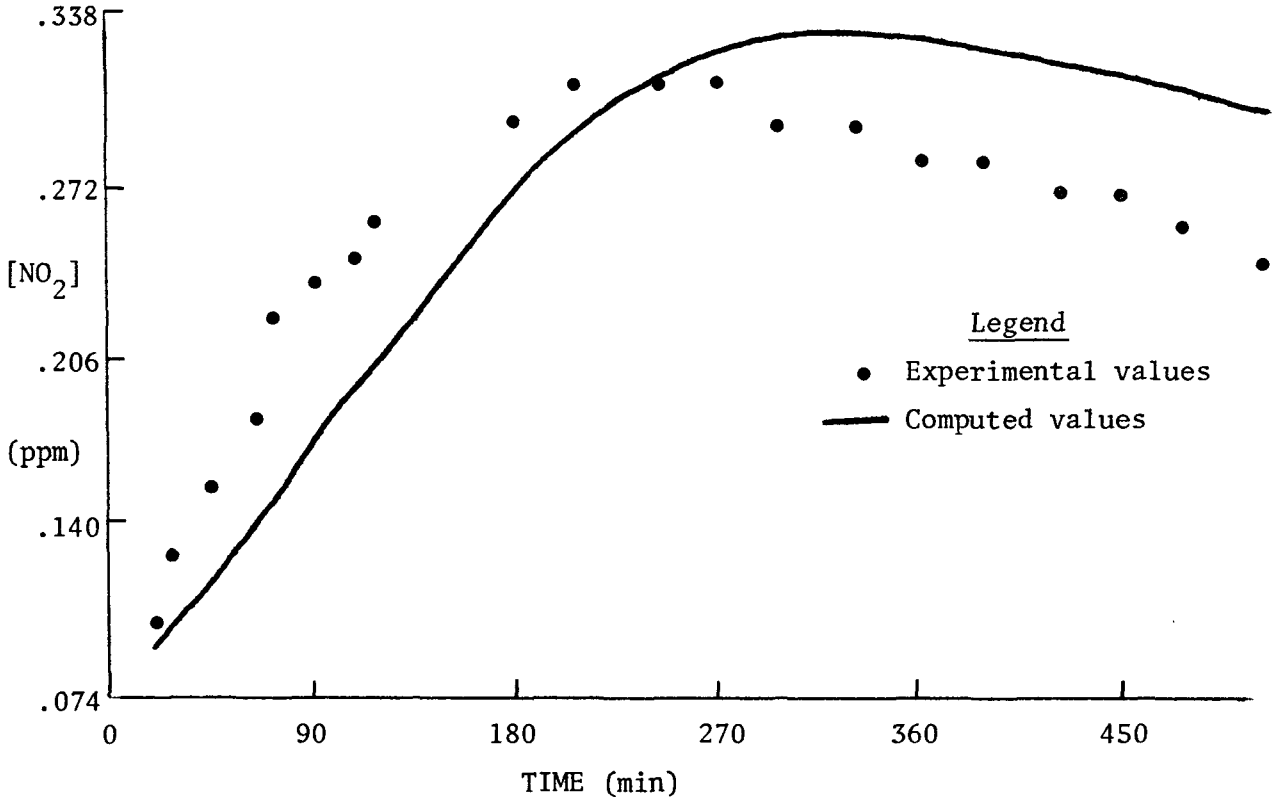

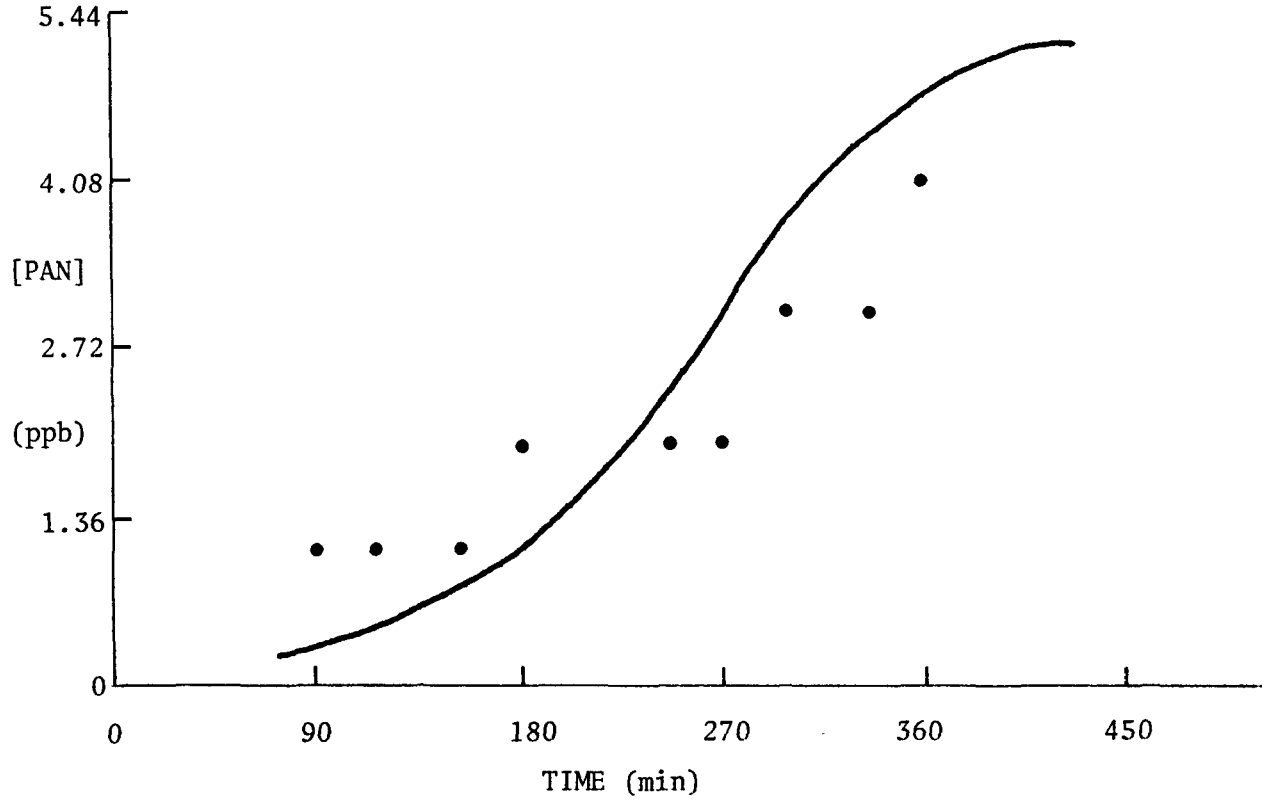

Figure 4-7 Simulation of Smog Chamber Experiment GC 150
(continued)

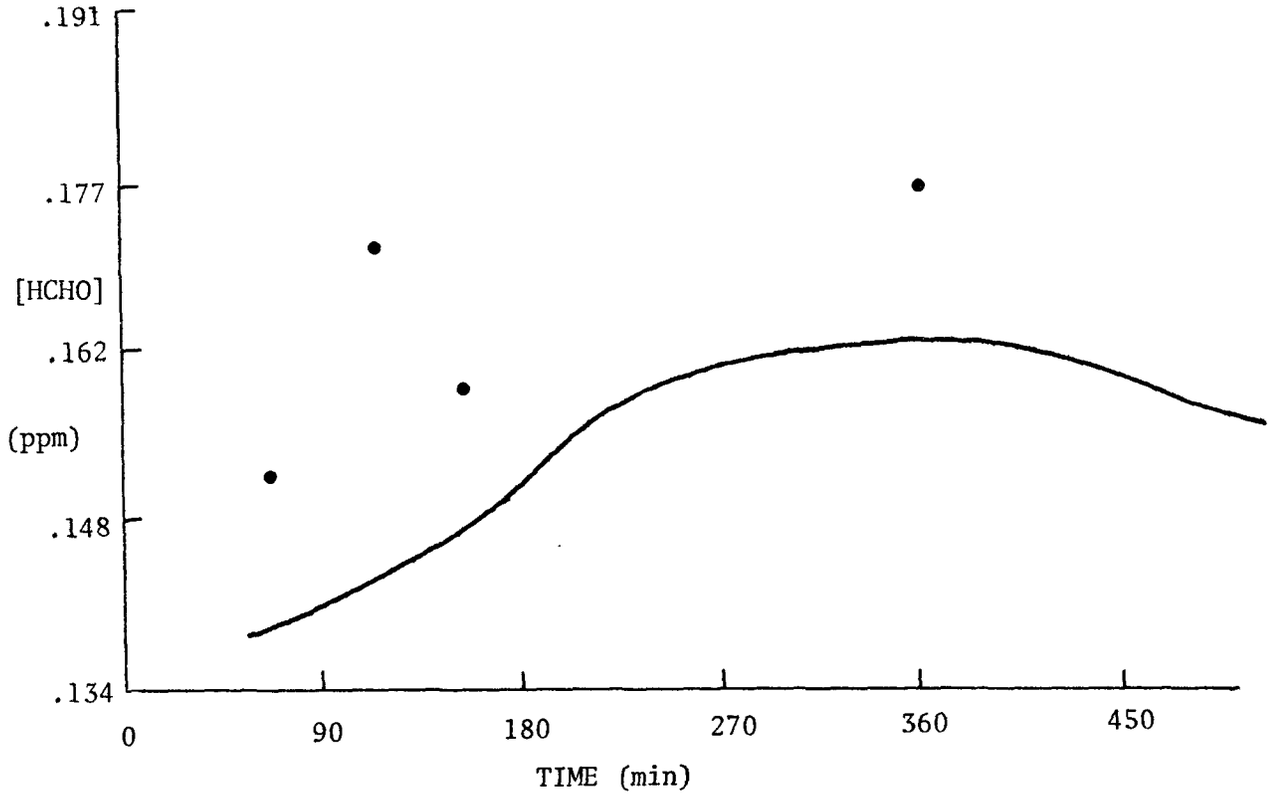

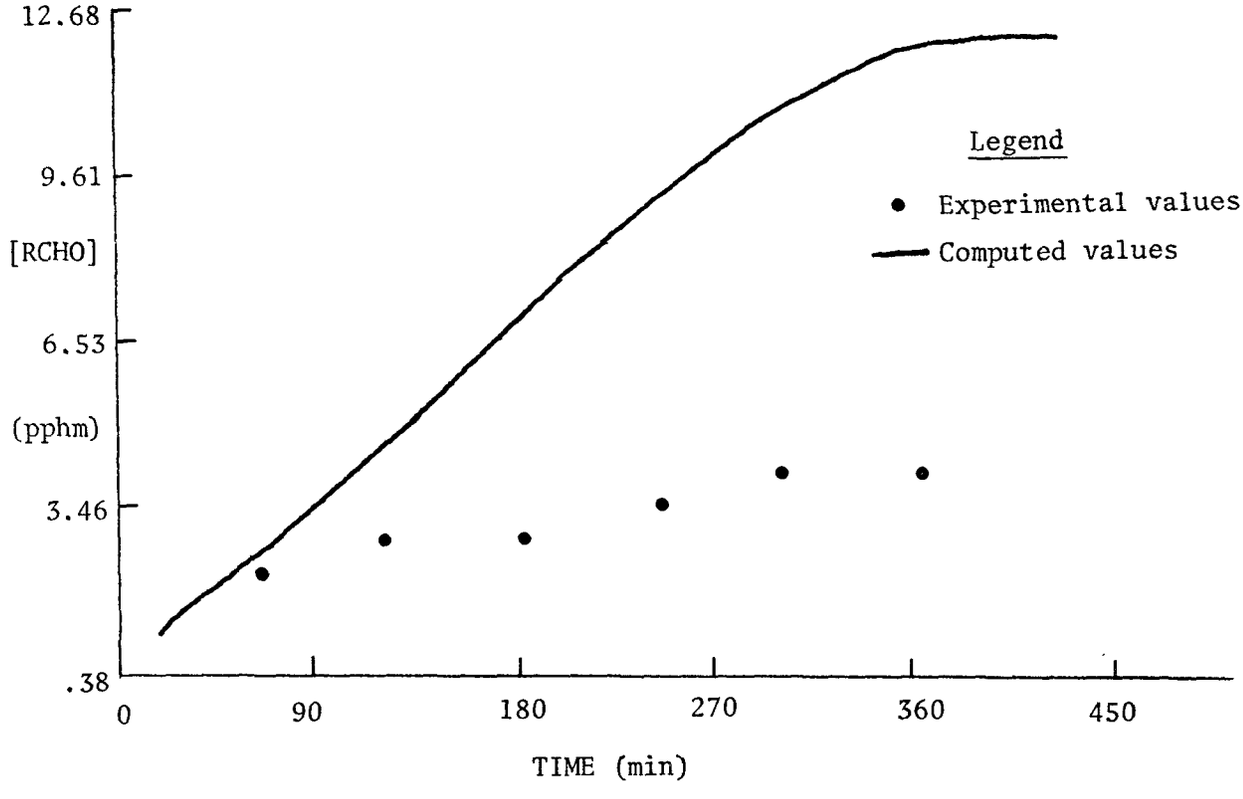

Figure 4-8 Simulation of Smog Chamber Experiment GC 156

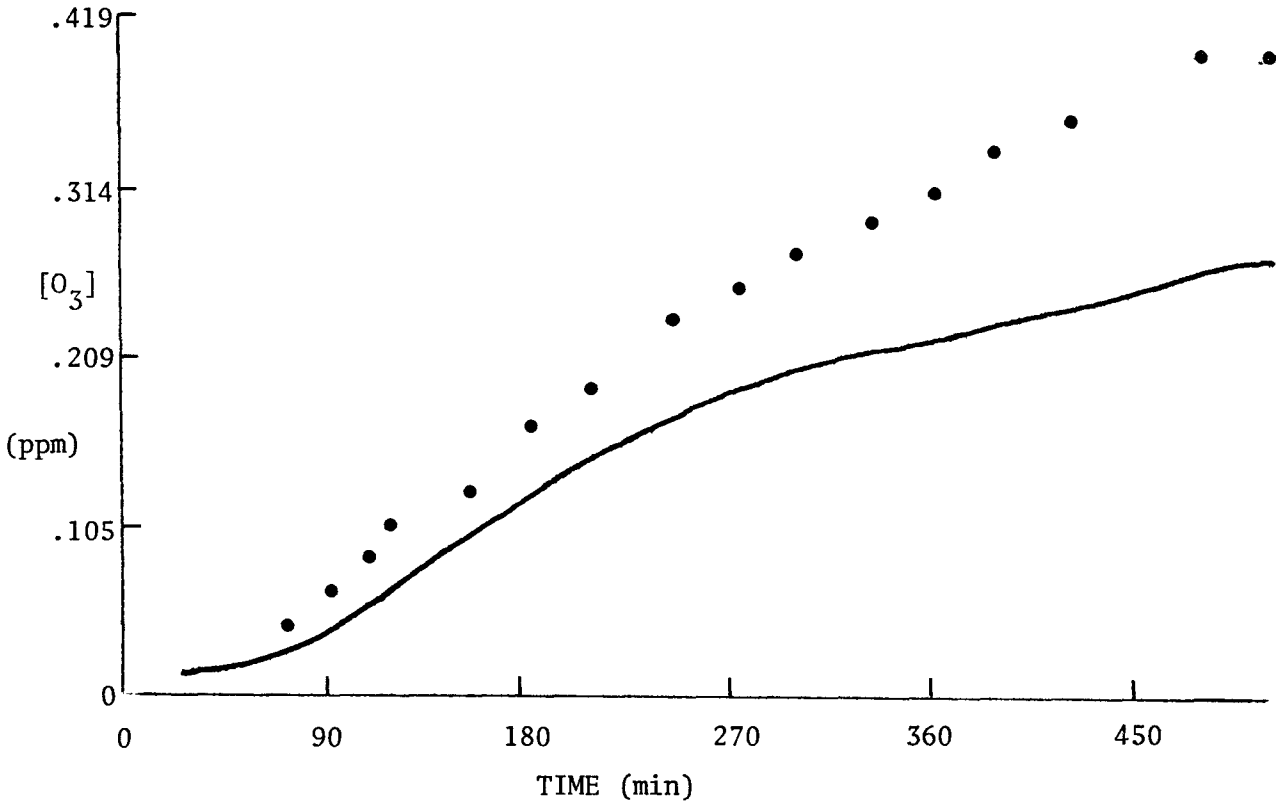

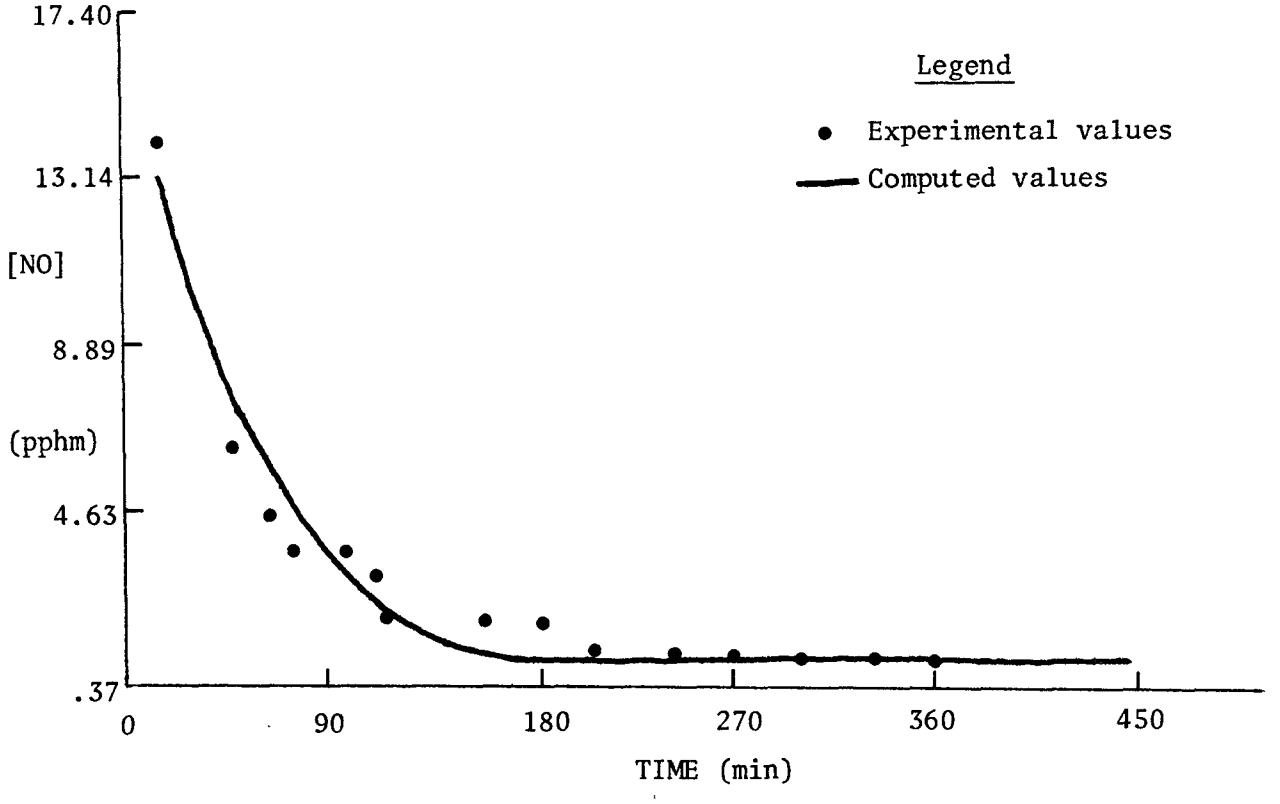

Figure 4-8 Simulation of Smog Chamber Experiment GC 156
(continued)

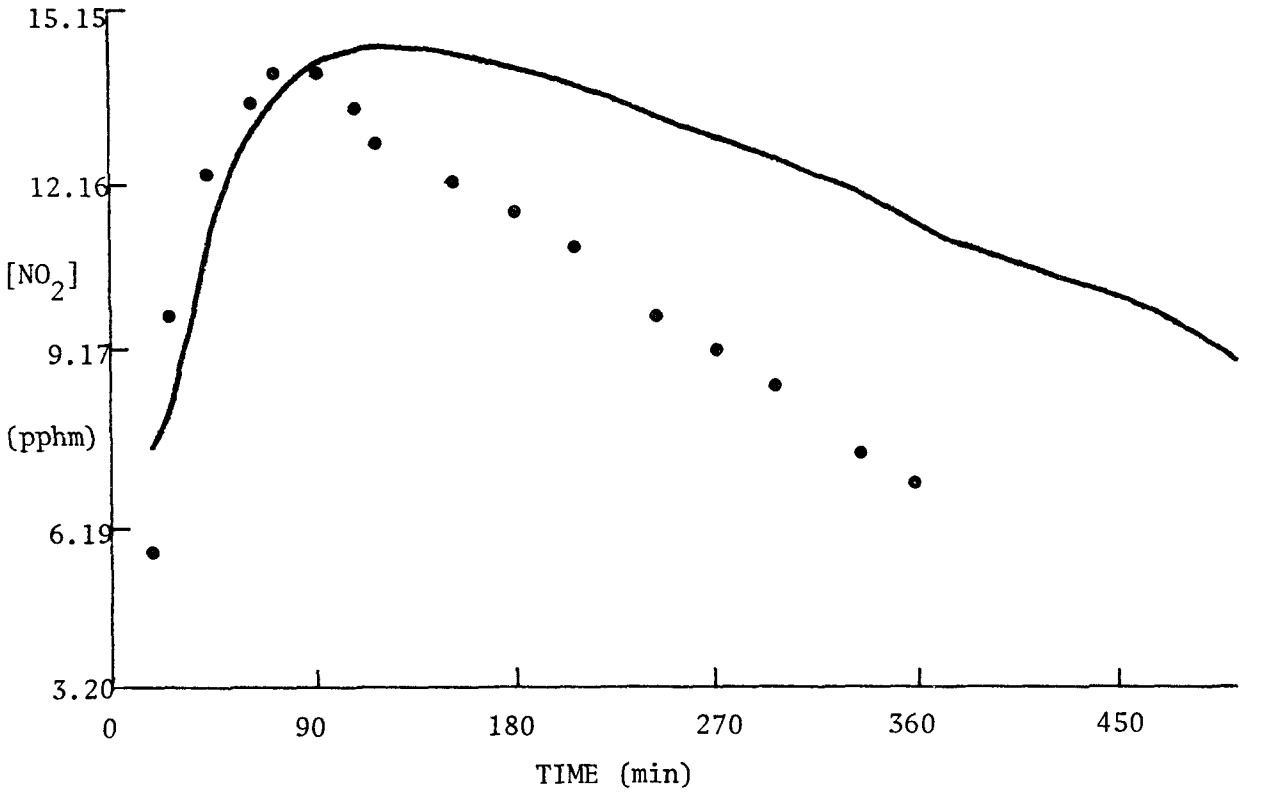

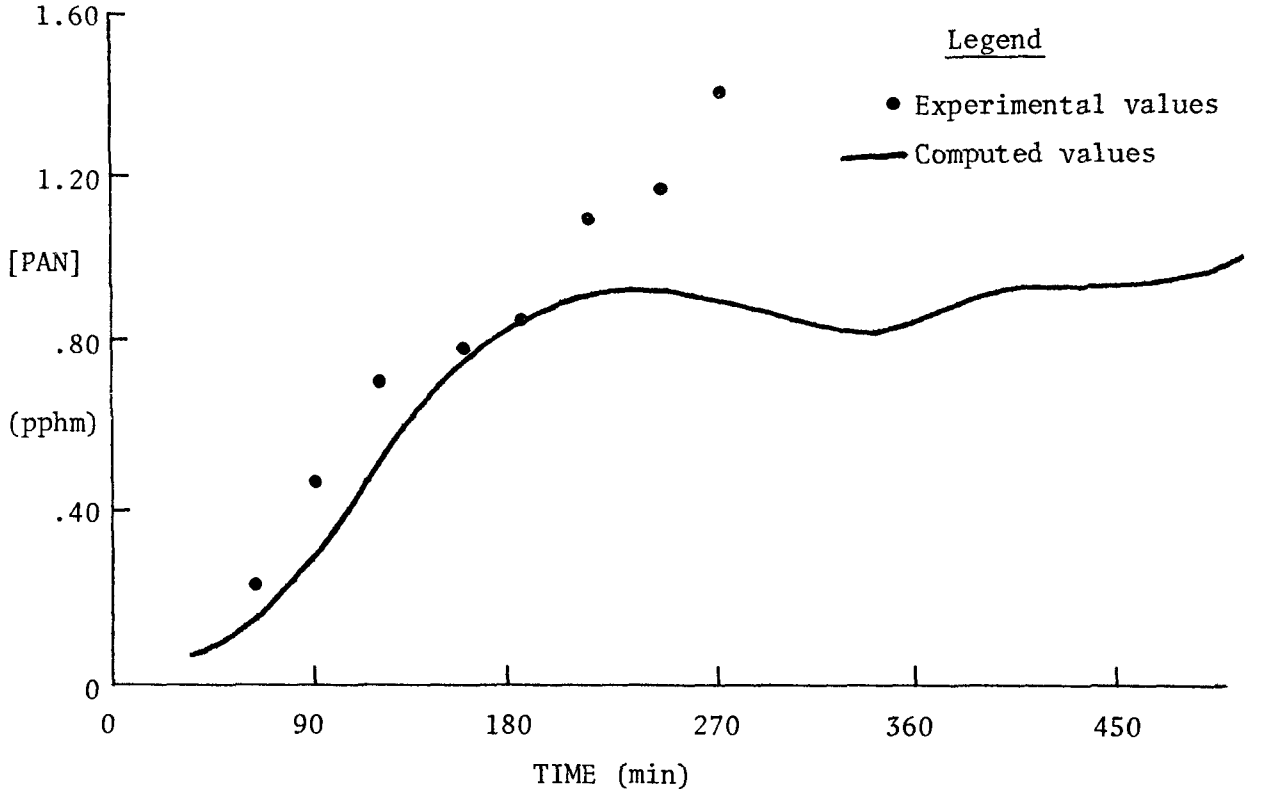

Figure 4-8 Simulation of Smog Chamber Experiment GC 156

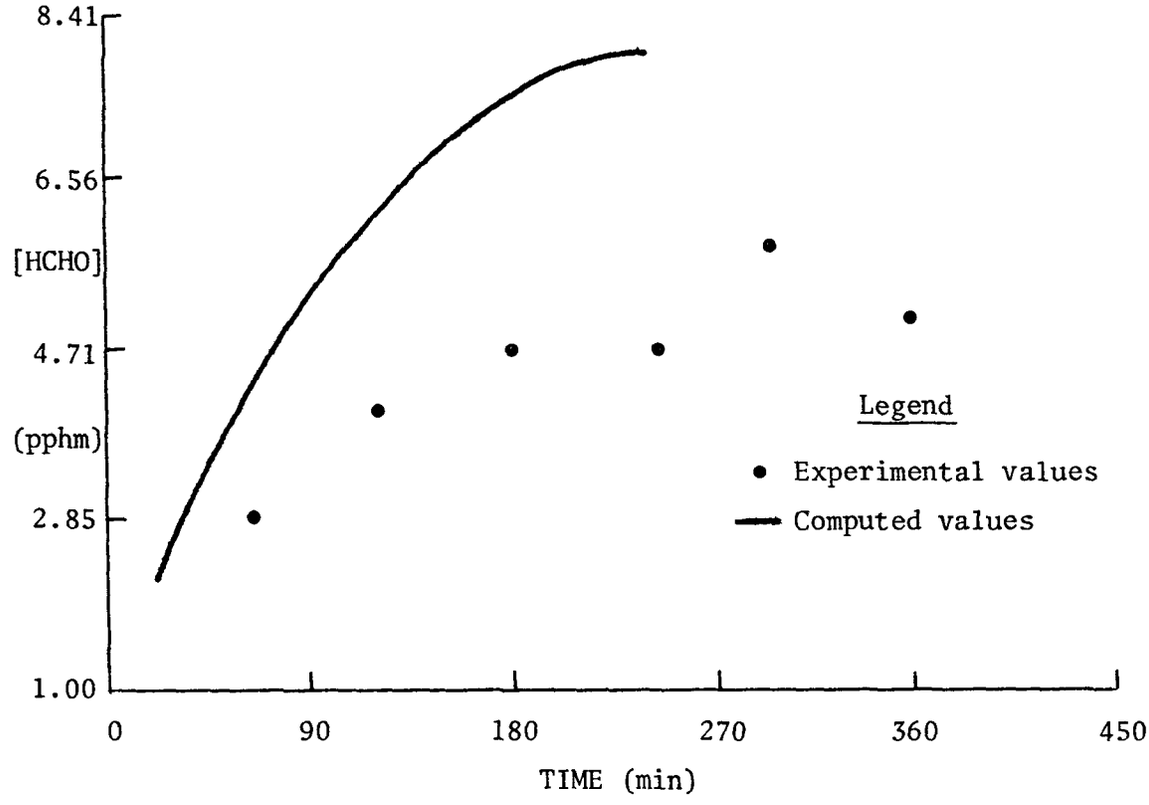

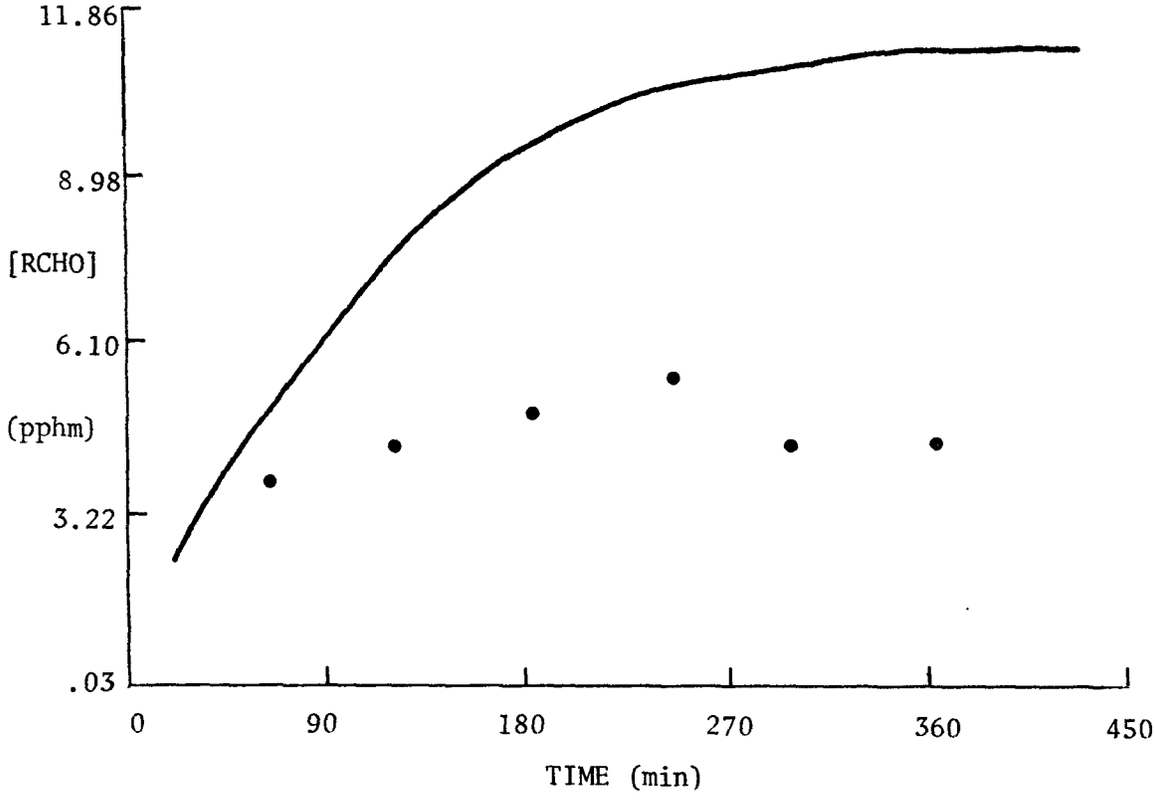

TABLE 4-4

SURROGATE HYDROCARBON SMOG CHAMBER RUNS USED FOR MODEL TESTING AND DEVELOPMENT*

Run (UCR#)	NO	NO_2	NO_x	Tot. HC	CO	HCHO	RCHO	HC/NO_x	O_3 Max
119	.301	.041	.340	.499	7.45	.038	.023	1.5	.24
133	.084	.013	.097	.318	4.05	.005	.011	3.3	.33
135	.030	.007	.037	.305	3.84	.027	.003	8.2	.22
138	.464	.050	.523	.482	7.9	.060	.003	0.92	.03
150	.440	.074	.523	.501	8.6	.134	.004	0.96	.17
156	.174	.032	.206	.471	6.8	.10	.003	2.3	.42

*All concentrations in ppm

TABLE 4-5

RATE CONSTANTS* USED FOR HYDROCARBONS (ppm^{-1} min^{-1})

Compound	OH	O_3	$O(^3P)$
Ethane	4.2×10^{2}	-	-
Propane	3.2×10^{3}	-	-
n-Butane	4.4×10^{3}	-	-
2,3,-Dimethylbutane	7.6×10^{3}	-	-
Ethene	1.2×10^{4}	2.5×10^{-3}	1.1×10^{3}
Propene	3.7×10^{4}	1.6×10^{-2}	5.2×10^{3}
Cis-2-Butene	7.9×10^{4}	1.8×10^{-1}	2.4×10^{4}
2-Methyl-2-Butene	1.2×10^{5}	8.9×10^{-1}	9.3×10^{4}
Toluene	8.8×10^{3}	-	-
m-Xylene	3.5×10^{4}	-	-

*Taken from Hampson and Garvin (1975); Pitts, et al (1976); Anderson, (1976).

and 1/2 for runs 150 and 156, respectively, to account for the reactivity of the mixture in terms of time to NO_2 maximum etc. Consequently, it can be seen that the mechanism does as well as might be expected from a lumped species mechanism although probably not as well as one with a larger number of reactions to account for all the different species involved. In general, the mechanism tends to underpredict the final O_3 slightly, but overpredicts it in the case of runs 135 and 138.

It can be seen from Figures 4-4 and 4-5 (Runs 133 and 135, respectively) that the computed NO concentration is significantly lower after about 90 minutes, than the experimental values. This is an experimental artifact whereby, at the low NO_x concentrations used for these particular experiments, there is a slow infusion of NO_x from the room air which maintains a fairly constant minimum NO_x concentration. The computed results assume that there is no introduction of NO_x during the irradiation. Consequently, the results of modeling these runs should be viewed with the above observation in mind.

In the majority of runs, the experimental values of NO_2 at the end of the irradiation are less than the computed values. This indicates that the current mechanism is not fully accounting for all the NO_x loss mechanisms. This has been rectified in the atmospheric model by increasing k_{17}.

The predicted ozone initiation times are in reasonable agreement with the experimental values and should not lead to significant problems when the mechanism is included in the atmospheric model. The O_3 initiation times are used as a guide in determining the initial HONO to be used, and this value is chosen to give the best agreement between the computed and experimental O_3 initiation times.

As indicated earlier, the formulation of so-called aldehyde production in the aromatic mechanism means that the computed PAN readings will generally be high compared with the experimental data. Thus, the scheme reflects this expectation in that the computed values are uniformly greater than the experimental measurements.

The aromatic mechanism shown is subject to large uncertainty and is being revised as new experimental data become available. A test of the aromatic mechanism could be made if the aromatic portion in the surrogate hydrocarbon data from the SAPRC smog chamber studies was varied sufficiently to be able to test the importance of aromatic hydrocarbon mechanisms in the overall hydrocarbon photooxidation and in ozone

production. The proposed reaction mechanism for aromatic photooxidation will require modification as more data become available.

Sensitivity of the results from this chemical mechanism to various input parameters and a discussion of uncertainties effecting model results are presented elsewhere (Martinez, et al, 1977).

4.2 Formulation of a Chemical Mechanism for SO_2 Oxidation

4.2.1 SO_2 Oxidation Chemistry

A discussion of the atmospheric chemistry of SO_2 should include both homogeneous and heterogeneous oxidation processes. Homogeneous processes are generally assumed to be gas phase homogeneous paths, whereas, heterogeneous processes usually include those involving aerosols, surfaces and water vapor, although by definition, both categories encompass a much broader spectrum of reactions. A crucial question in the atmospheric oxidation of SO_2 is the relative importance of homogeneous gas phase chemistry compared to the heterogeneous routes (Hidy and Burton, 1975; Calvert, 1974; Wilson, 1976). Heterogeneous reactions are assumed to be most important in areas of high relative humidity and/or aerosol loading and also in pollutant plumes, which may contain catalysts such as iron, vanadium or manganese. Homogeneous processes are generally understood to be significant in areas of high photochemical activity with elevated levels of ozone and other oxidants.

The following discussion considers homogeneous gas phase processes only. For modeling purposes, we have assumed that any reaction forming SO_3 will eventually form sulfate, SO_4. The reactions are listed accordingly.

Sulfur dioxide does absorb ultraviolet radiation (Calvert and Pitts, 1966), but unlike nitrogen dioxide, it does not dissociate to produce an oxygen atom until about 2180Å -- far shorter wavelengths than found in the lower atmosphere. However, the role played by excited SO_2 ($^3B_1$), formed in the atmosphere by absorption of the available radiation, is insignificant, and Calvert, et al (1978) estimate that the maximum rate of oxidation of SO_2 by direct photo-absorption is less that 0.02% per hour. In view of the fact that atmospheric oxidation rates ranging anywhere from .1% to > 10% per hour have been observed, it is apparent

that the direct photo-absorption reaction will be of very minor significance. Thus, other processes make the major contribution towards the atmospheric oxidation of SO_2. These processes have been listed previously by other workers (e.g. Calvert, 1975; Wilson, 1976; Hidy and Burton, 1975) and involve inorganic radical intermediates, such as O atoms, OH, HO_2, and NO_3 radicals, and organic radical intermediates, such as RO, RO_2, and RCO_3. The importance and occurrence of these species as contributors to SO_2 oxidation are discussed separately below.

We have postulated a number of reactions, which on the basis of current information we feel to be important in the conversion of SO_2 to sulfate in the presence of hydrocarbons and NO_x: these six reactions, shown in Table 4-6, have been added to the previous list of 46 reactions used to model the hydrocarbon/NO_x system. The importance of various reactions are discussed initially, while subsequent discussions in this report describe the ability of this reaction scheme to reproduce the results of selected smog chamber studies.

$\underline{OH + SO_2 + M \rightarrow HSO_3 + M \twoheadrightarrow SO_4}$

It is generally recognized (Calvert and McQuigg, 1975; Sander and Seinfeld, 1976; Calvert, et al, 1978) that this is the most important single gas phase reaction consuming SO_2 in the atmosphere. The rate constant for this reaction has been studied by many workers, but a reliable value applicable to atmospheric conditions is less easy to obtain since the reaction is in the pressure dependent region for pressures normally studied under laboratory conditions. In addition, several workers (Davis and Klauber 1975; Payne, et al, 1973; Cox, 1974, 1975; Wood, et al, 1975; Castleman, et al, 1975; and Castleman and Tang, 1977) studied this reaction in competition with the reaction

$$OH + CO \rightarrow CO_2 + H$$

which is shown as reaction (9) in Table 4-2. This reaction has been shown to exhibit a pressure dependence at the low pressure often used in laboratory studies (Sie, et al, 1976; Cox, et al, 1976; Chan, et al, 1977). Consequently, the rate constants obtained for OH + SO_2 from the competitive rate studies must be increased by approximately a factor of 2 to bring them in line with the new measurements of k_9.

In addition to these competitive rate studies, several results have been obtained using the flash photolysis-resonance fluorescence technique. These results include studies by Davis and Schiff (1974), Harris and Wayne (1975), and Atkinson, et al (1976). The latter workers obtained a high pressure limit of 8.3×10^{-13} cm^3 mol^{-1} sec^{-1} by extrapolation of their data to the high pressure limit. The study of Gordon and Mulac (1975) was carried out at one atmosphere total pressure and 435° K, and they obtained a value of 1.8×10^{-12} cm^3 mol^{-1} sec^{-1}.

We have chosen the value of 1.2×10^{-12} cm^3 mol^{-1} sec^{-1} (using a corrected value for k_9) in our model calculations. This is equivalent to 1.76×10^3 ppm^{-1} min^{-1}. This value is about the same as that obtained by Calvert, et al, (1978), by taking an average of the results of the most comprehensive data sets at atmospheric pressure.

For modeling purposes, we have assumed that this reaction will eventually produce sulfate, although it is recognized that intermediary steps are involved. The specific reactions are shown in Table 4-6.

$$\underline{HO_2 + SO_2 \rightarrow OH + SO_3 \twoheadrightarrow SO_4}$$

It is evident from this reaction that OH radicals are produced in the oxidation of SO_2 by HO_2. The only reported determination of the rate constant for this reaction is that by Payne, et al (1973). They obtained a rate constant for this reaction relative to the reaction $HO_2 + HO_2 \rightarrow H_2O_2 + O_2$ and obtained a value of $8.7 \times 10^{-16} cm^3$ mol^{-1} sec^{-1}. However, if the value for k ($HO_2 + HO_2$) recommended by Hampson and Garvin (1975) is used, a value of 1.5×10^{-15} cm^3 mol^{-1} sec^{-1} (2.2 ppm^{-1} min^{-1}) is obtained. However, a recent preliminary result obtained by Thrush, et al, (Atkinson, 1978), suggests that the rate constant is at least two orders of magnitude less than this. We have used a value of 0.03 ppm^{-1} min^{-1} for the rate constant in our model. This preliminary value is likely to be modified slightly as more work is carried out.

It has been suggested that the product of this reaction could be one of addition, giving HO_2SO_2. However, there is little evidence for this. Thus, Calvert, et al (1978) estimate that this reaction would make only a very minor contribution to the overall measured rate for $HO_2 + SO_2$.

$O + SO_2 + M \rightarrow SO_3 + M \rightarrow\rightarrow SO_4$

This reaction of ground state oxygen atoms with SO_2 is generally regarded to be of little significance in the atmospheric oxidation of SO_2. This is because most of the oxygen atoms produced from the photolysis of ambient NO_2 react with oxygen molecules to produce ozone.

The rate constant for this reaction has been measured by a number of people and these determinations have been summarized and/or evaluated by Schofield (1973), Hampson and Garvin (1975), and Westenberg and DeHaas (1975). The recent experimental work of Westenberg and DeHaas indicates that the earlier measurements were a factor of 2 too high. The measurements of Westenberg and DeHaas give a value of 4.9×10^{-14} cm^3 mol^{-1} sec^{-1} for an atmosphere of nitrogen. Calvert, et al (1978) using data for nitrogen and oxygen as third bodies, obtained a value of 5.7×10^{-14} cm^3 mol^{-1} sec^{-1} applicable to atmospheric conditions. We have used the latter value in our calculations. Whichever value is used, the contribution of this reaction to atmospheric SO_2 oxidation is negligible, although in theory its importance in SO_2 oxidation in stack gas plumes may be more significant.

$NO_3 + SO_2 \rightarrow SO_3 + NO_2$

The oxidation of SO_2 by NO_3 radicals formed largely by the reaction of NO_2 with O_3, has been invoked in some modeling studies, e.g. Durbin, et al, (1975) as contributing in a major way to SO_2 oxidation; this would be particularly true in the later stages of photooxidation of hydrocarbon/ NO_x/SO_x mixtures where the NO_3 concentration increases significantly. However, studies by Daubendiek and Calvert (1975) and Davis and Klauber (1975) find that the rate constant for this reaction has a value of around 10^{-21} cm^3 mol^{-1} sec^{-1}. Thus, this reaction is unlikely to be of any significance during the daytime oxidation of NO_2, although it is possible that if the NO_3 concentration increases significantly during nighttime hours (as a result of the reaction of O_3 with NO_2), then this reaction could assume more importance in the oxidation of SO_2. This reaction has not been included in our model.

Reactions of Organic Radicals with SO_2

The reactions which may be considered to be of importance for SO_2 oxidation by organic radicals include the alkylperoxy radicals, acylperoxy radicals and the Criegee intermediates formed in the reaction of ozone with olefins.

Previous modeling studies (Calvert, 1974; Calvert and McQuigg, 1975) have shown that alkylperoxy radicals could play a significant role in terms of SO_2 oxidation. However, it is only recently that an estimate has been obtained for the rate constant for the reaction

$$CH_3O_2 + SO_2 \rightarrow SO_3 + CH_3O$$

This has been obtained by Whitbeck, et al (1976), who observed the kinetics of the decay of methylperoxyl radicals spectroscopically following its generation in the flash photolysis of a mixture of azomethane, oxygen and SO_2. A rate constant of $(5.3 \pm 2.5) \times 10^{-15}$ cm^3 mol^{-1} sec^{-1} was obtained for a combination of this reaction and the alternative pathway

$$CH_3O_2 + SO_2 \rightarrow CH_3O_2SO_2$$

However, Calvert, et al (1978), estimate that the latter pathway will make only a minor contribution to the overall rate constant. Thus, this rate constant is sufficiently large to make the reaction of alkylperoxy radicals contribute about the same amount to SO_2 oxidation as that contributed by HO_2 based on these calculations.

The reaction of acylperoxy radicals with SO_2 has not been studied directly and the contribution which it makes to SO_2 oxidation is subject to some uncertainty. However, it now appears that the reaction

$$CH_3CO_3 + SO_2 \rightarrow CH_3CO_2$$

makes a negligible contribution to SO_2 oxidation under ambient conditions. This conclusion is based largely on the studies of Pate, el al (1976), who showed that the introduction of SO_2 into a PAN mixture had no effect on the kinetics observed for PAN decomposition. In addition, it has been shown that SO_2 introduction into a synthetic photochemical smog

mixture has a negligible effect upon the PAN yields (Fox and Wright, 1977). If the reaction

$$RCO_3 + SO_2 \rightarrow SO_3 + RCO_2$$

was important, then it would compete with the reaction $RCO_3 + NO_2$ to produce PAN. Thus, a change in PAN concentration should be noted upon the introduction of SO_2 if indeed the reaction of RCO_3 with SO_2 were important. Since this is not the case, the results give the same conclusion as that obtained by Pate, et al, and this reaction has not been included in our simulations.

Reaction of SO_2 with the Products of Ozone/Olefin Reactions

It is well known that the direct reaction of SO_2 with O_3 is slow. However, Cox and Penkett (1971) found that the addition of an olefin to a mixture of SO_2 and ozone led to a rapid increase in the SO_2 oxidation rate. This has been interpreted as being due to the oxidation of SO_2 by products of the ozone/olefin reaction, such as the Criegee intermediate, $RCHO_2$. However, later studies (Calvert and McQuigg, 1975; Calvert, et al, 1978) suggest that most of this increased oxidation is due to other products of the ozone/olefin reaction, such as hydroxyl radicals and hydroperoxyl radicals. The contribution of the Criegee intermediate to SO_2 oxidation is uncertain. In this current model we have assigned a value of 2.9×10^3 ppm^{-1} min^{-1} for the rate constant for SO_2 oxidation by the Criegee intermediate. This value is a factor of 10 less than the rate constant for $RCHO_2$ reacting with NO. This chosen value may be high, but was chosen on the basis of comparison with predicted and experimental smog chamber data for sulfates.

4.2.2 Validation of $HC/NO_x/SO_x$ System

Table 4-6 shows the additional chemical reactions and rate constants which have been utilized to predict the homogeneous gas phase conversion of SO_2 to sulfates in the presence of hydrocarbon/NO_x mixtures. It was assumed that all the SO_3 formed would eventually produce sulfates and this supposition is apparently a reasonable one to make (Calvert, et al, 1978). It can be seen that the species chosen for the oxidation process

TABLE 4-6

ADDITIONAL REACTIONS USED FOR $HC/NO_x/SO_x$
HOMOGENEOUS REACTION MECHANISM

Reaction			Rate Constant $ppm^{-1}\ min^{-1}$
$O + SO_2 + M$	→	$SO_4 + M$	8.40E+1
$OH + SO_2$	→	SO_4	1.76E+03
$HO_2 + SO_2$	→	$OH + SO_4$	3.0E-02
$RCHO_2 + SO_2$	→	$SO_4 + RCHO$	2.9E+03
$RO_2 + SO_2$	→	$RO + SO_4$	8.0E+00
$AO_2 + SO_2$	→	$AO + SO_4$	8.0E+00
SO_4 + Wall	→	Loss of SO_4	3.12E-05

NOTE: SO_4 is defined as being any ultimate sulfate species. The initial product in most cases will be SO_3, which will then convert to sulfate, SO_4.

(1). AO_2 is the product of the addition of OH to an olefin in the presence of O_2. (See above).

are O, OH, HO_2, RO_2 (including AO_2 formed from the addition of OH to an olefin in the presence of oxygen), as well as the Criegee intermediates. The basis for the choice of rate constants has been detailed above.

The data base initially used to test the reaction mechanism was that obtained from the Battelle chamber simulations and supplied to us by Dr. B. Dimitriades of the EPA. These results were obtained in a 17.8 cubic meter smog chamber. SO_2 concentrations were measured using a Beckman 906 analyzer, while sulfate concentrations were obtained from aerosol size distributions measured with a Thermosystems electrical aerosol analyzer, using the assumption that equilibrium existed between sulfuric acid aerosol in the condensed and vapor phases. Independent chemical measurements of sulfate apparently showed that this method was very accurate. The measured sulfate concentration-time history proved to be very difficult to reproduce with the model in spite of numerous changes in the mechanism and rate constants to try to obtain a good fit with the sulfate experimental data.

The initial conditions for the specific chamber runs chosen to test the mechanism are shown in Table 4-7. Unfortunately, at the time of this model development exercise a paucity of reliable and comprehensive smog chamber data for systems including SO_2 existed. Thus, the task of obtaining a reliable chemical mechanism, tested in detail against an extensive smog chamber data base could only represent a preliminary study.

In order to check our chemical mechanism against the Battelle chamber data, we chose Battelle run #114, which contained propylene in a mixture of NO_x in air. Our complete chemical mechanism was modified by zeroing the rate constants associated with the reactions of the paraffins, aromatics and SO_2; in addition, the rate constants for the reactions of O, OH and O_3 with olefins were modified from Table 4-5 to make them applicable to propylene. Since the initial values of HCHO and RCHO were not given in the experimental details, we chose values which appeared reasonable based on the experimental data from the U.C. Riverside smog chamber facility. Of course, such a procedure is far from satisfactory, but faced with a lack of experimental measurements, there appeared little alternative.

TABLE 4-7

INITIAL CONDITIONS FOR BATTELLE
SMOG CHAMBER SIMULATIONS

Battelle Run #	Initial Concentrations of Reactants (ppm)			
	NO	NO_2	Propylene	SO_2
S - 107	0.328	0.113	1.03	0.474
S - 110	0.392	0.099	1.10	0.480
S - 114	0.414	0.095	0.95	0.0

4.2.3 Results and Discussion

Reasonable agreement was obtained between the predicted and experimental data as shown in a typical plot, Figure 4-9, although full equilibrium value of HONO was required to produce sufficient initial radicals to match the experimentally observed initial rate of NO oxidation. Even then, later in the run, the mixture appears more reactive than the computed predictions, indicating that a continuous wall radical or molecule flux may be a better approach to modeling these results than choosing a high initial concentration of HONO.

The effect of adding SO_2 to the propylene/NO_x mixture in air was modeled by including the SO_2 reactions in the chemical mechanism and testing the predictions against Battelle data, such as runs S-107 and S-110. Two plots, typical of the many obtained, are shown in Figures 4-10 and 4-11. The major conclusion from these calculations is the fact that it proved impossible to get a reasonable fit simultaneously for NO, NO_2 and O_3 in addition to that for SO_2 and SO_4.

It is evident from the results shown in the figures that much work remains to be carried out to elucidate the mechanism of homogeneous gas phase sulfate formation. Such work should encompass smog chamber studies, as well as basic kinetic and mechanistic studies involving SO_2.

4.2.4 Conclusions of Current Modeling of Homogeneous SO_2 Oxidation

While progress is being made in our understanding of the homogeneous processes controlling the oxidation of SO_2 under atmospheric conditions, many areas require further detailed study. Thus, more information is required in order to develop and test a reliable chemical mechanism to describe the homogeneous transformation of SO_2 to sulfate under ambient conditions. Among the areas for research are the following:

- The kinetics of the reaction of SO_2 with intermediates, such as $RCHO_2$, and AO_2 (which is the product of the addition of OH to an olefin in the presence of O_2), are not known and require study.

Figure 4-9 Simulation of Smog Chamber Experiment B-S-114

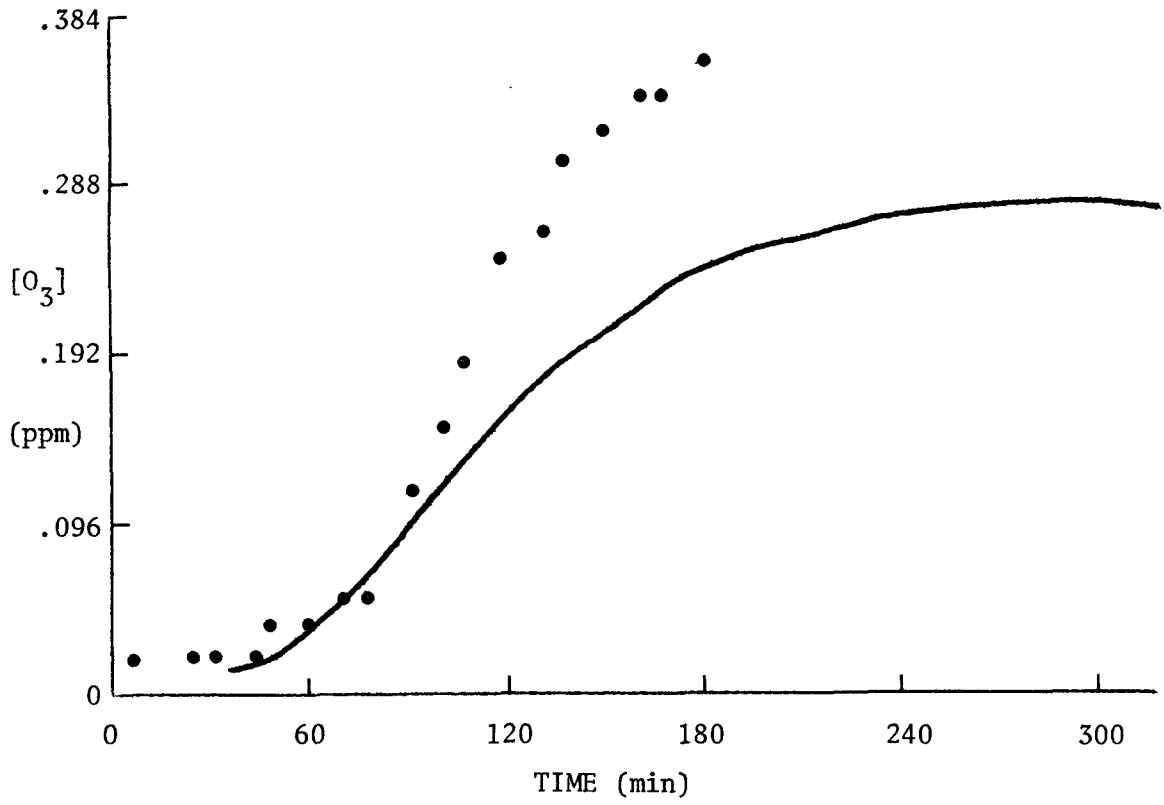

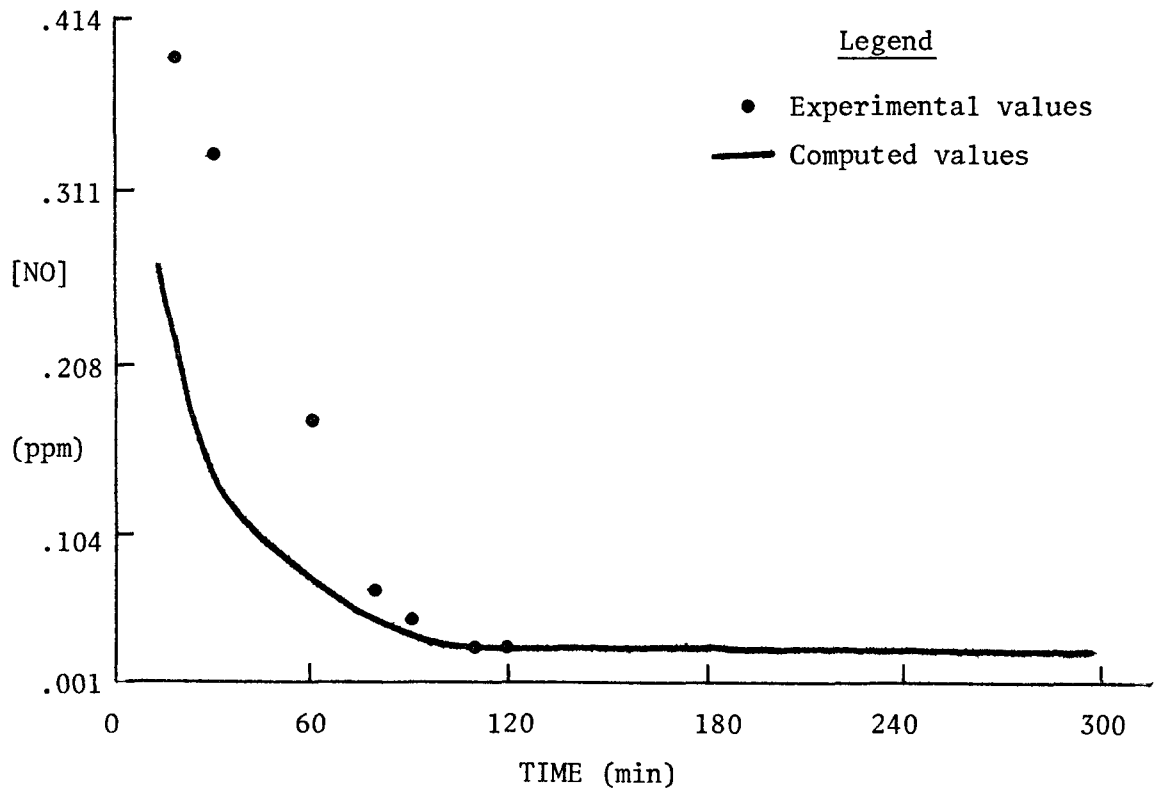

Figure 4-9 Simulation of Smog Chamber Experiment B-S-114
(continued)

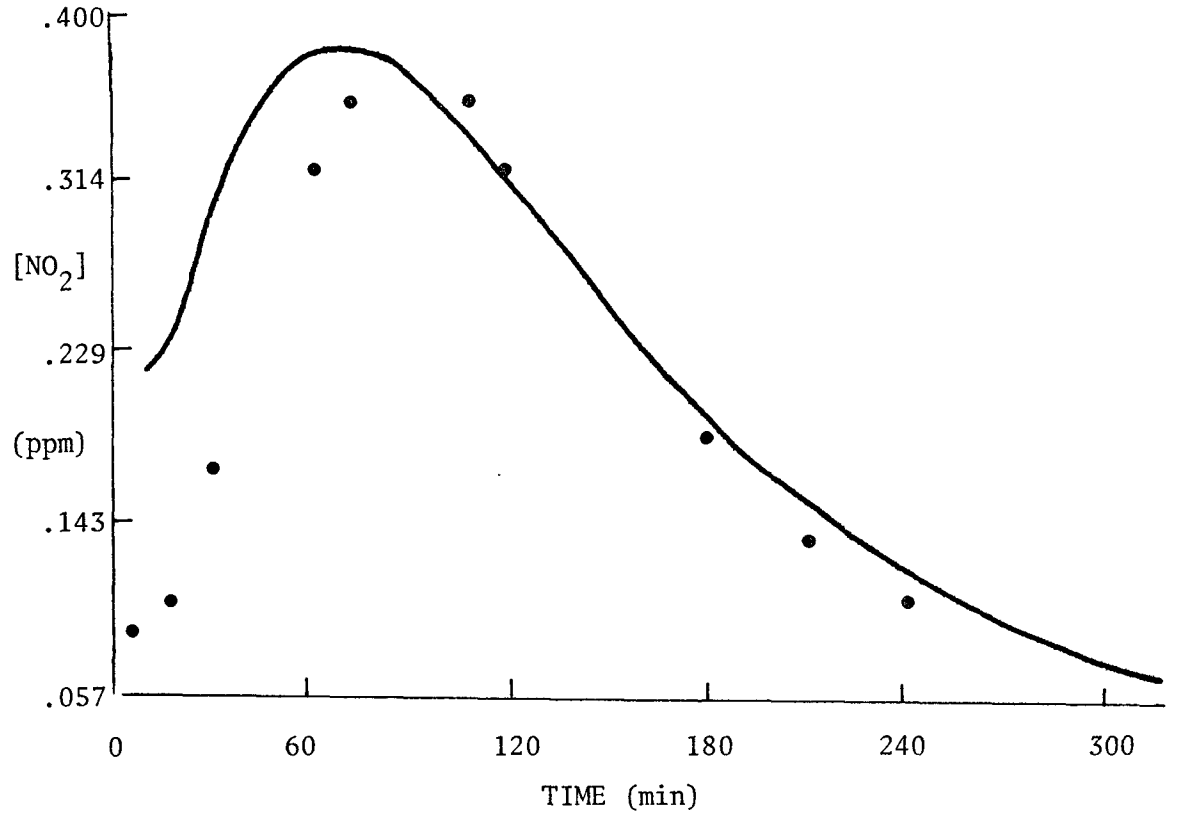

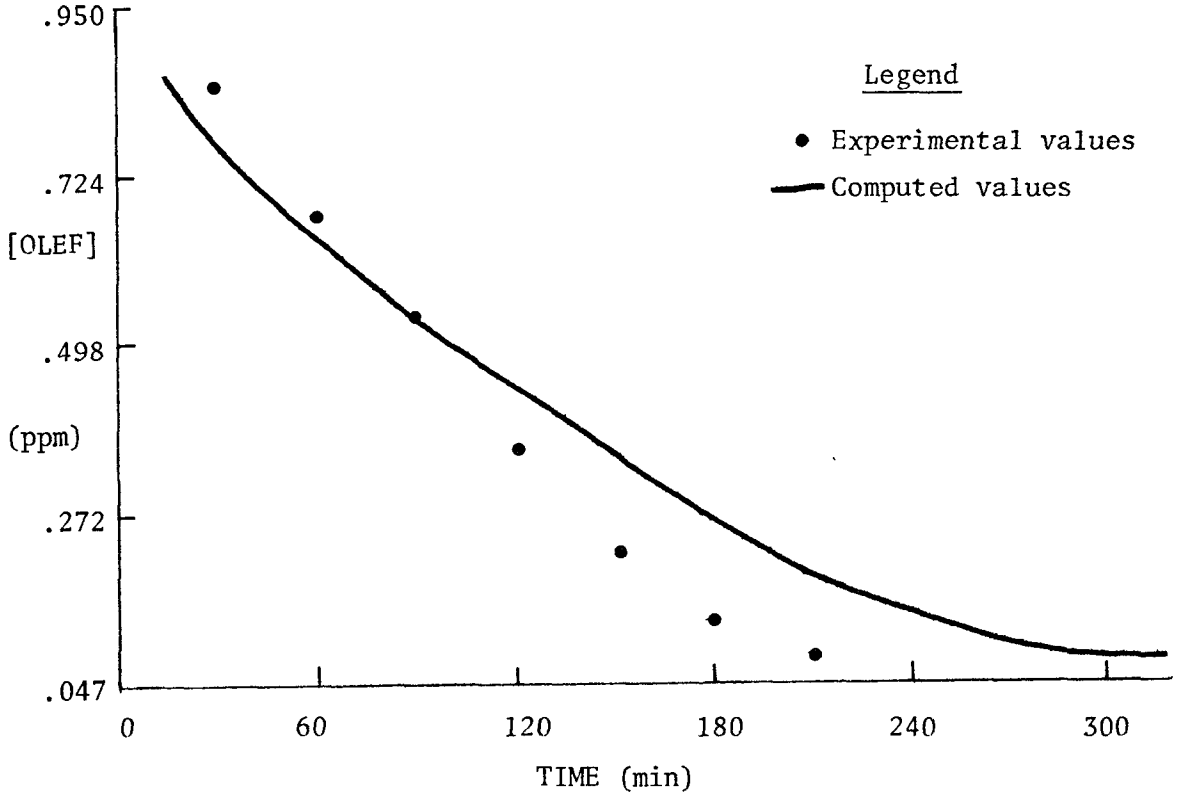

Figure 4-10 Simulation of Smog Chamber Experiment B-S-110

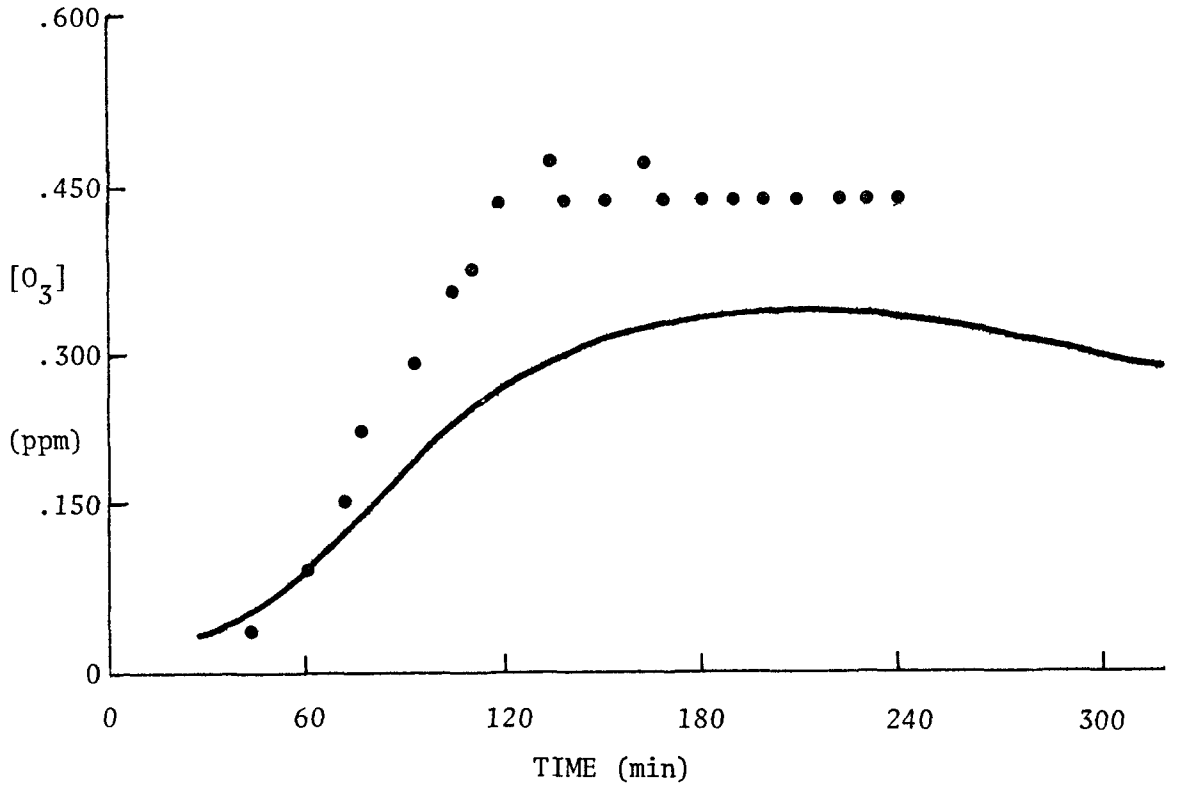

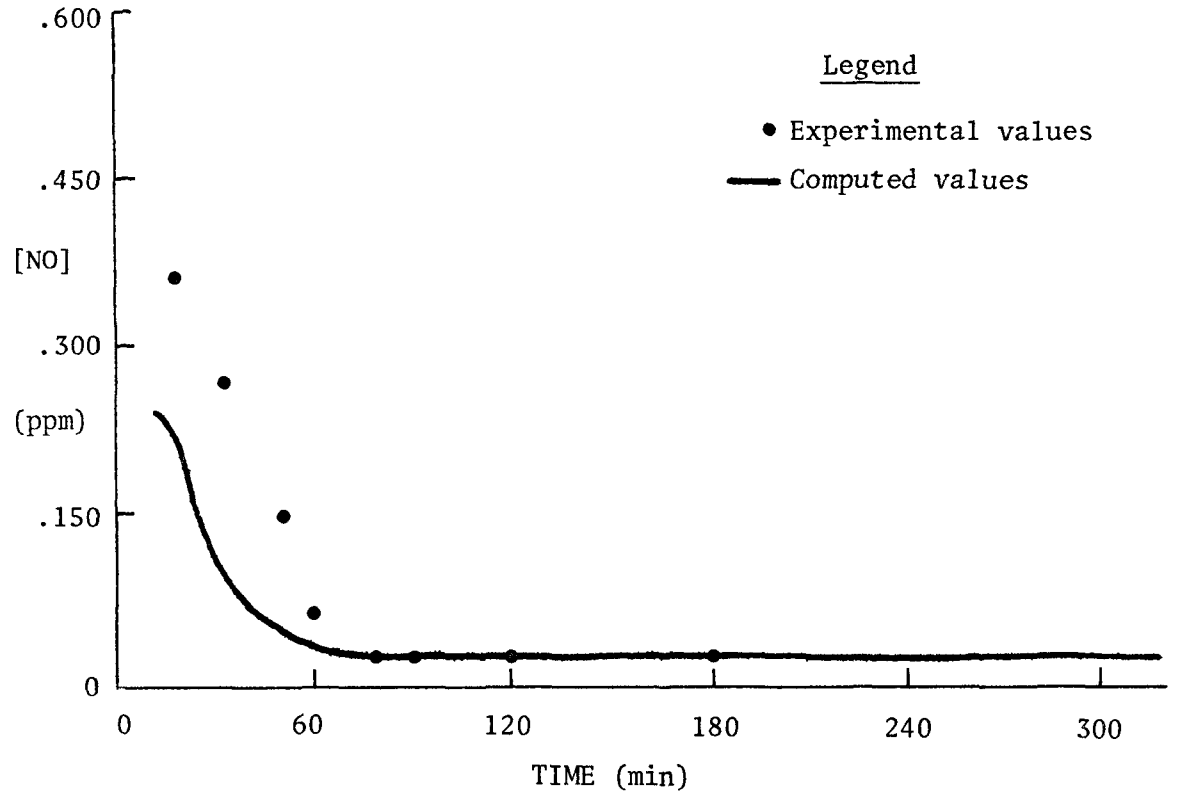

Figure 4-10 Simulation of Smog Chamber Experiment B-S-110
(continued)

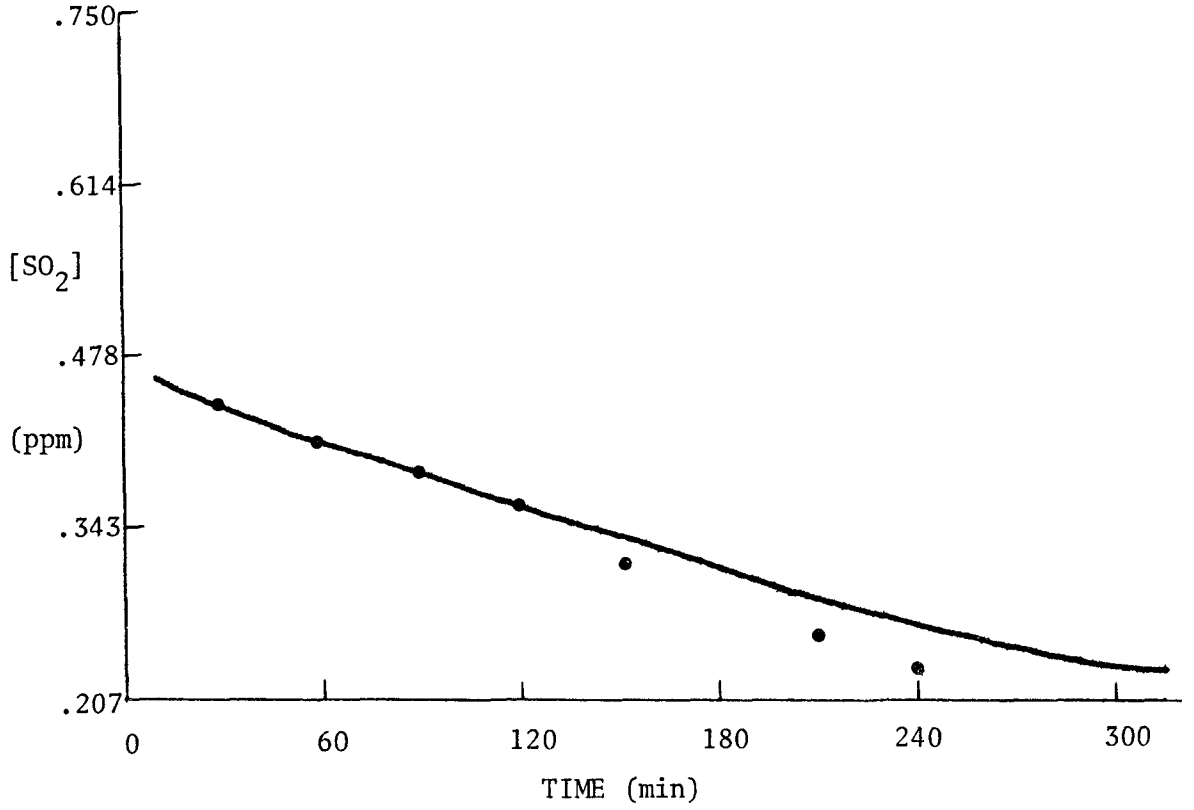

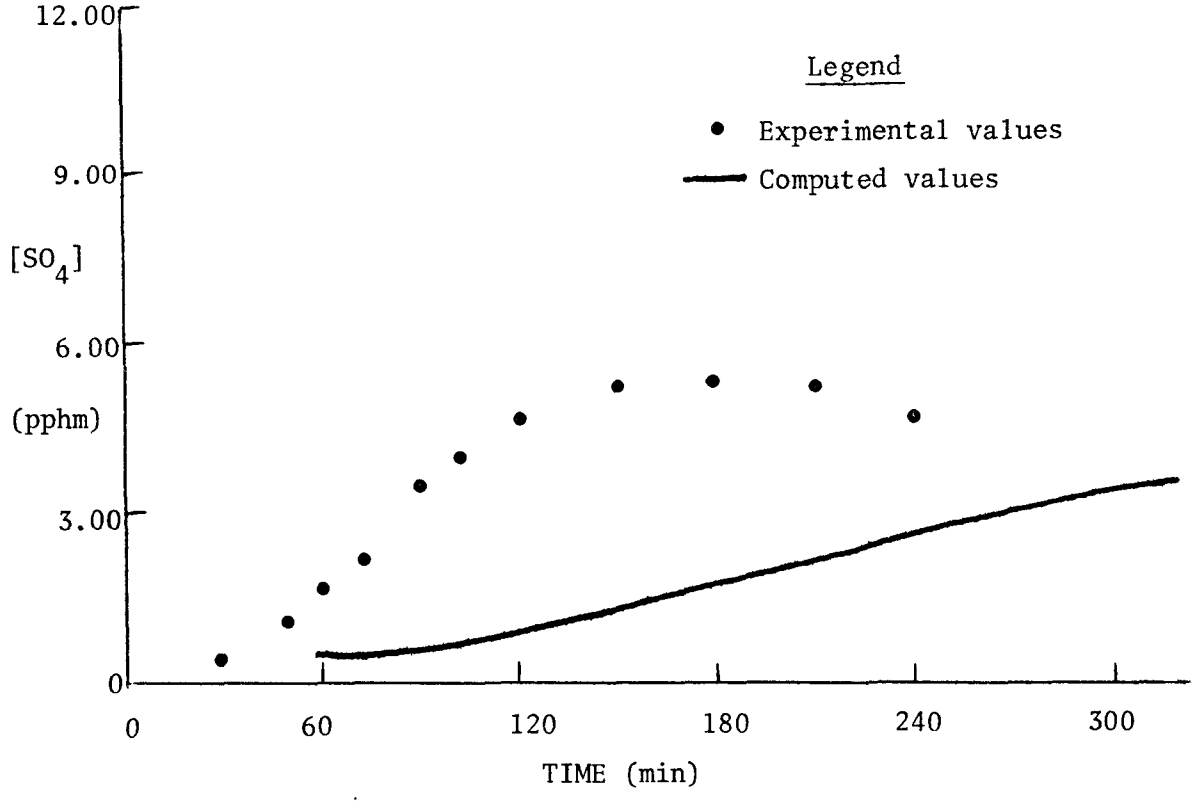

Figure 4-10 Simulation of Smog Chamber Experiment B-S-110
(continued)

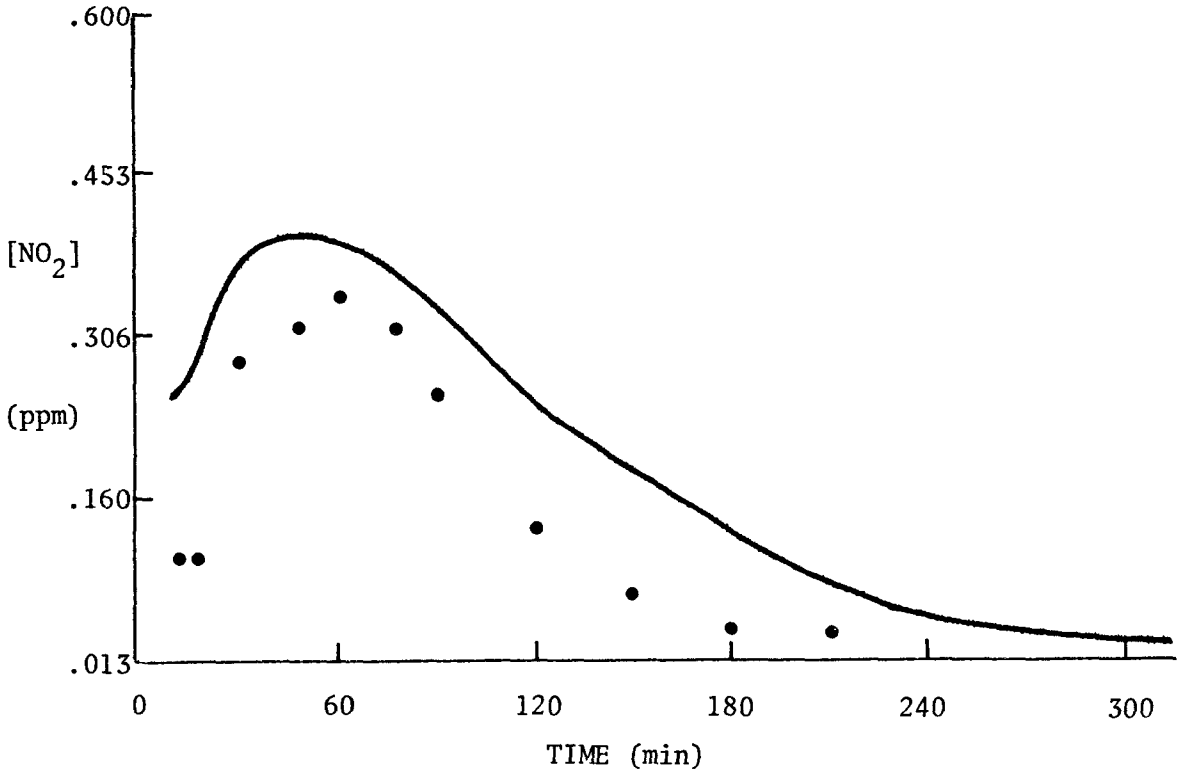

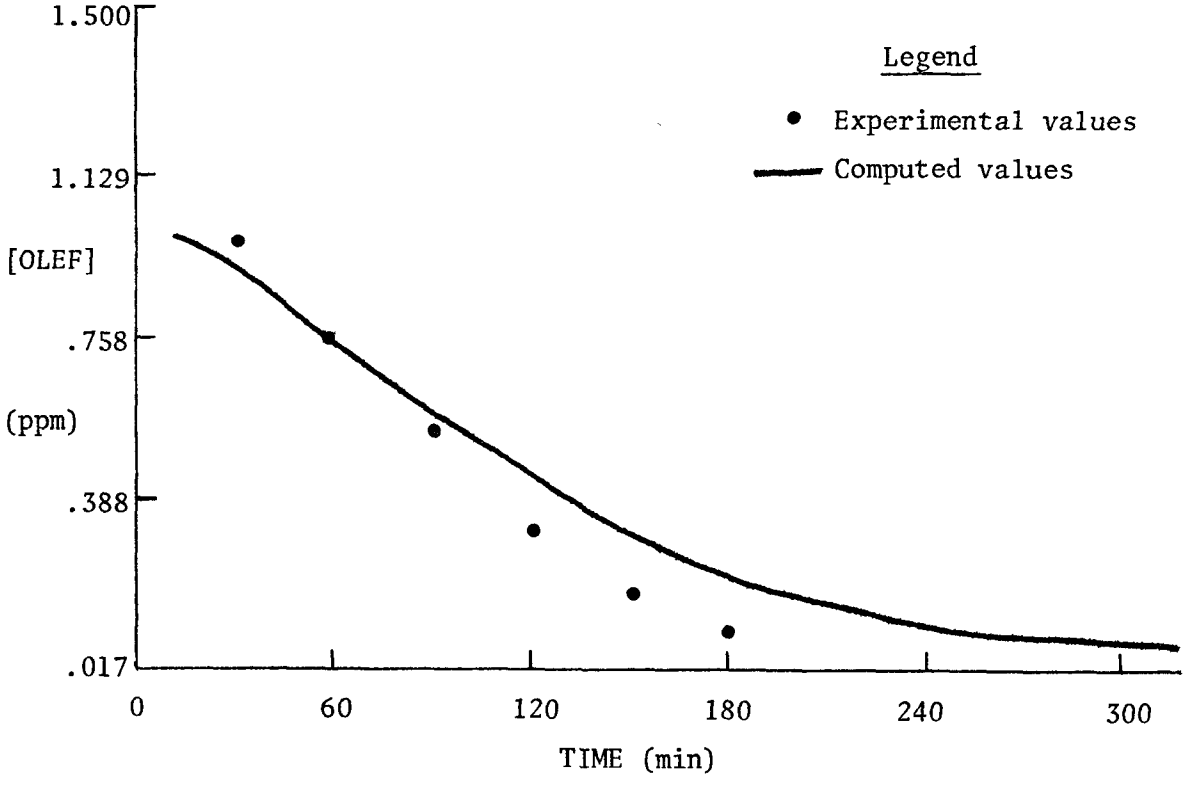

Figure 4-11 Simulation of Smog Chamber Experiment B-S-107

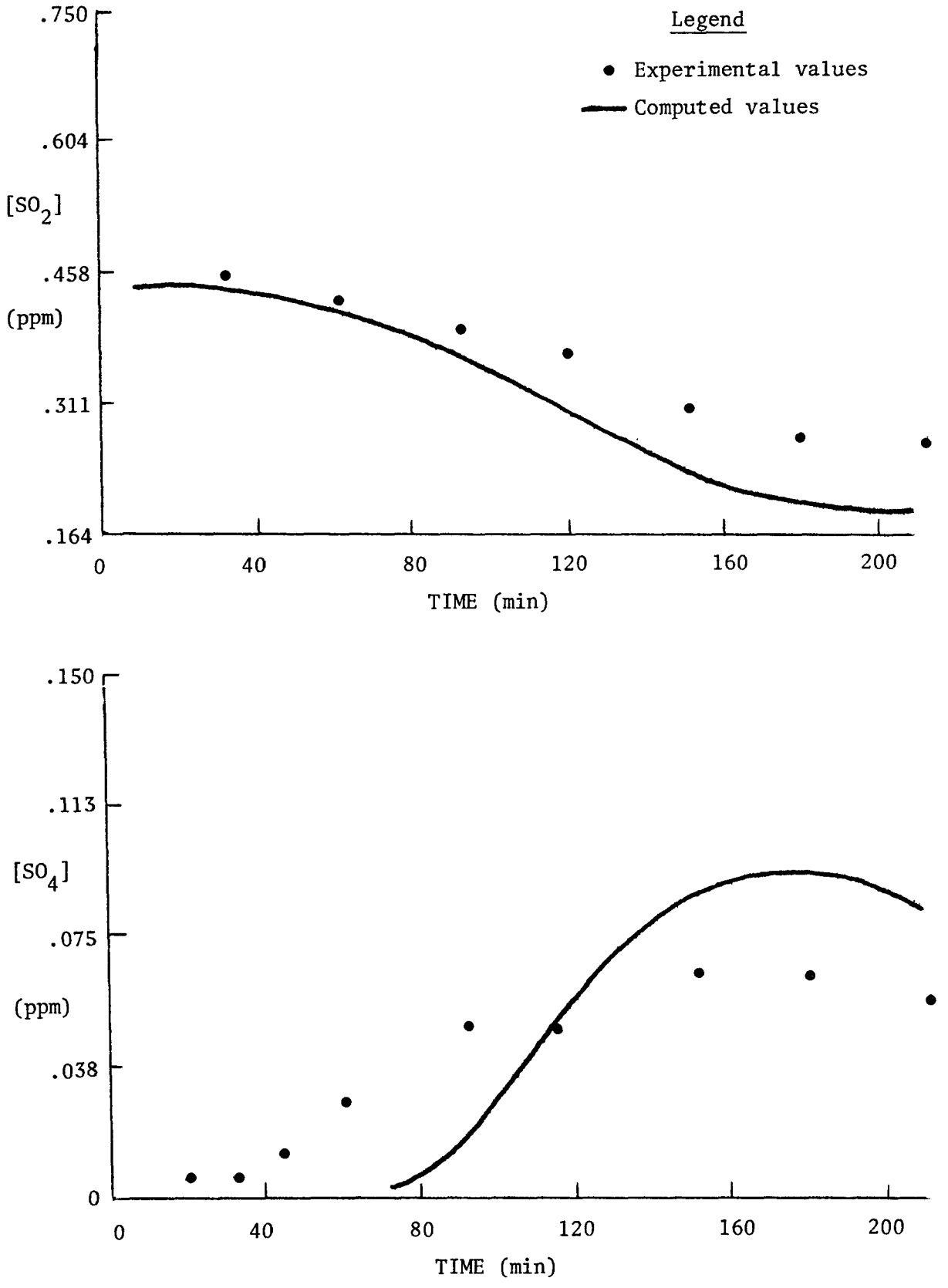

- product data for systems containing mixtures of hydrocarbons, nitrogen oxides and SO_2 in air are practically nonexistent. A detailed search should be made for organic sulfur compounds and organic-sulfur-nitrogen compounds.
- the smog chamber data for the $HC/NO_x/SO_2$ system are much less extensive than those available for the HC/NO_x system. Thus, more smog chamber studies are required which contain a variety of mixed hydrocarbons, as well as single hydrocarbons in the presence of NO_x and SO_2. Only when the results of such studies become available, can the proposed mechanism for the homogeneous oxidation of SO_2 be rigorously tested.
- until the type of data outlined above become available, studies using the best currently available data, together with sound estimates of unknown parameters, should continue to be used to advance our knowledge of the behavior of SO_2 and sulfates in HC/NO_x mixtures in air.

5. ADAPTATION OF THE MODEL TO THE ST. LOUIS REGION AND RAPS DATA BASE

The adaptation of the trajectory model to the St. Louis region involved not only development of software to interface the programs with the RAPS data base, but also development of procedures to account for the unique characteristics of the region and the data base.

The RAPS meteorological data base includes surface data from the Regional Air Monitoring System (RAMS) stations and data for higher elevations from the Upper Air Sounding Network (UASN) stations. The locations of these measurement stations are shown in Figure 5-1. The RAMS meteorological data used in the modeling includes surface wind speed, wind direction, temperature, near surface vertical temperature gradient, and solar radiation data. Retrieval software was developed to directly interface the RAMS data archive (on magnetic tape) with the meteorological module of the code. The data requirements from the UASN data archive were vertical temperature profiles (0-3000 meter elevations). Automated interfaces were not developed for the UASN data retrieval since the data requirements were quite small.

In adapting the model to the RAMS wind data, procedures were employed to account for differences in wind measurement heights above the surface. Since most of the instruments were positioned on 30-meter towers, the wind speed data from stations with 10-meter towers were adjusted to equivalent 30-meter wind speeds. The formulation of this adjustment is based on a stability-dependent power law wind profile (Sellers, 1965), as shown below:

$$u_{z_2} = u_{z_1} \left(\frac{z_2}{z_1} \right)^a$$

where $$a = \begin{cases} .33 \text{ , stable} \\ .18 \text{ , neutral} \\ .14 \text{ , unstable} \end{cases}$$

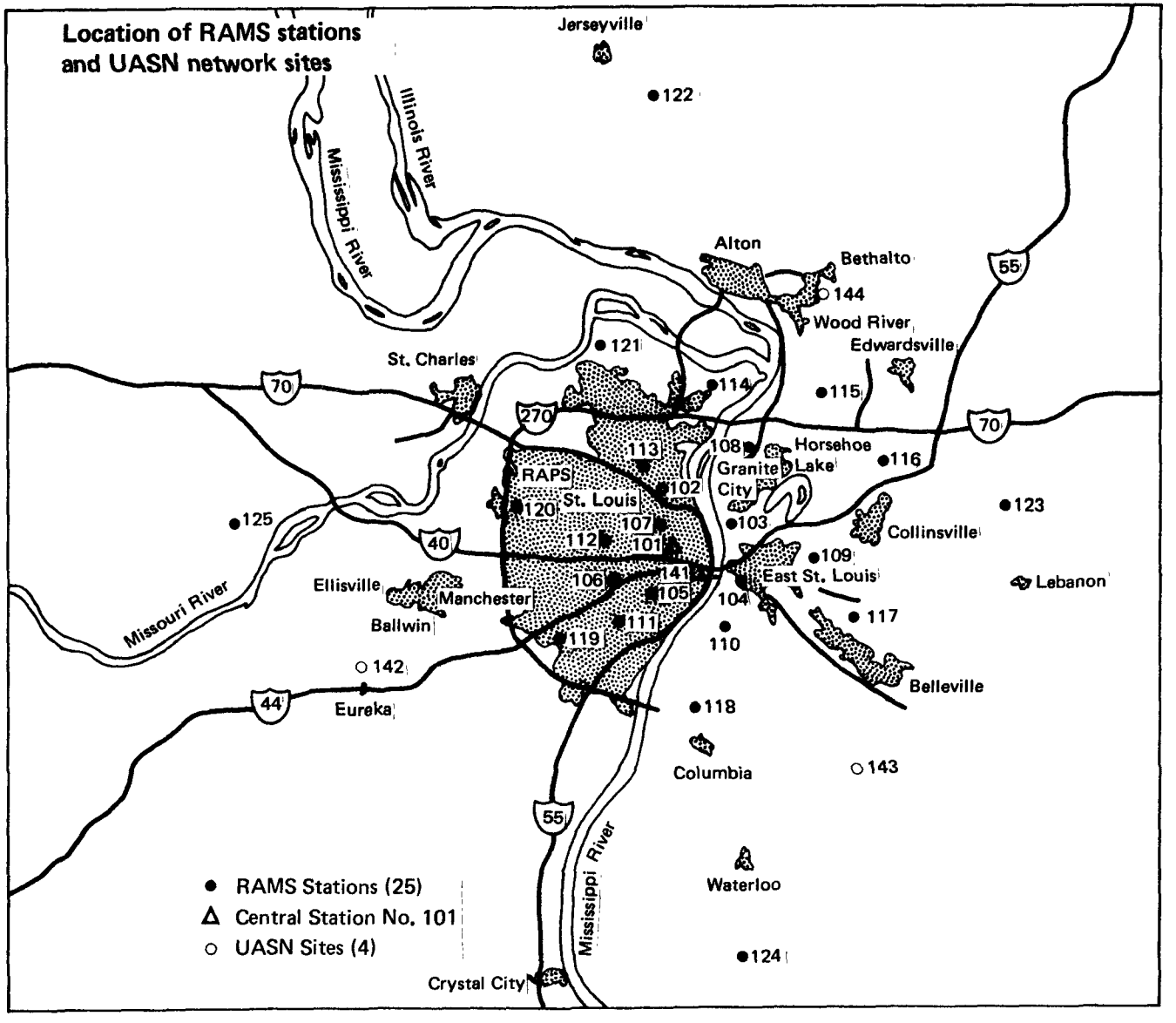

Figure 5-1 RAPS Measurement Station Locations

Each hour's stability was classified by computing the hour's regional average temperature gradient and using the following criteria:

$$\frac{dT}{dz} > -.005\ °C/m \qquad \text{stable}$$

$$-.005 \geq \frac{dT}{dz} \geq -.015\ °C/m \qquad \text{neutral}$$

$$\frac{dT}{dz} \leq -.015\ °C/m \qquad \text{unstable}$$

The net result of this correction is the multiplication of 10-meter wind speed by 1.437, 1.219, and 1.166 for stable, neutral, and unstable conditions, respectively. These adjustments were made for the wind data from RAMS Stations 108, 110, 114, 115, 116, 117, 118, and 121. No adjustments were made to the corresponding wind direction data since the available methods were not believed to be reliable.

Another feature incorporated by the model accounts for differences in the surface roughness length for the urban and rural portions of the modeling region. Since the urban region is approximately circular, a surface roughness island is simulated in the model. The urban region within five kilometers of the island center (identified by UTM x and y coordinates of 739.5 and 4280.5 km) is assumed to have a surface roughness length of one meter. The rural region located beyond ten kilometers from the center is assumed to have a roughness length of 0.25 meters. In the suburban region between five and ten kilometers from the center, the surface roughness is assumed to vary linearly with distance between 1.0 and 0.25 meters.

In adapting the model to the RAMS data base, procedures were incorporated to compute and interpret the ultraviolet radiation data. The ultraviolet radiation for each hour was calculated by subtracting the measured solar radiation for wavelengths greater than 3950 Angstroms from the total solar radiation data. The regional average ultraviolet radiation was computed from data collected at six stations. This regional average of observed radiation was compared with the expected clear-sky ultraviolet radiation function shown in Figure 5-2. The ratio of the observed to the expected ultraviolet radiation was computed and is referred to as the sky clearness ratio in this study. The clearness

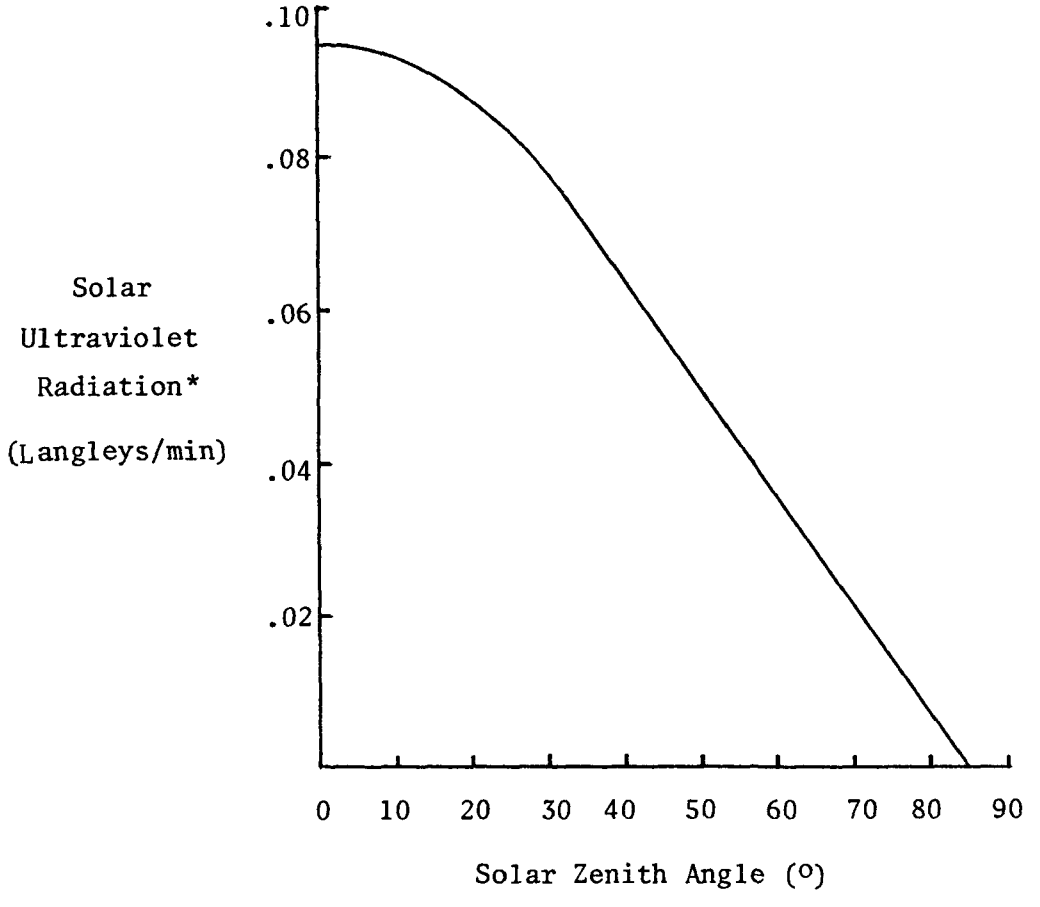

*For wavelengths less than 3950 Angstroms and near sea-level elevations.

Figure 5-2. Clear-Sky Ultraviolet Radiation

ratio is used in the model to adjust the clear-sky ultraviolet-dependent photodissociation rates to the appropriate levels. These computational procedures were fully automated for this study.

The clear-sky radiation function applies to solar radiation with wavelength less than 3950 Angstroms (Å) and for near sea-level elevations. It was developed for this study based on both observed and computed clear-sky solar radiation for St. Louis reported by Bergstrom and Peterson (1977). Since their data only included radiation below 3800 Å, an upward adjustment of 31 percent was incorporated into the UV function for wavelengths below 3950 Å. This adjustment was based on the ratio of solar actinic fluxes through 3950 Å to actinic fluxes through 3800 Å computed by Peterson (1976) for solar zenith angles between 20 and 60 degrees.

Terrain maps for the St. Louis region were examined, and it was concluded that the topographic features within the region were too small to present significant barriers to the wind fields. Thus, the air trajectory generation submodule of the code was set up without geographic barriers normally used to constrain air parcel trajectory paths.

Program modifications were incorporated (as optional features) to accommodate the variable size grid square characteristic of the RAPS emissions grid. The RAPS area source data are compiled (by EPA) for grid squares ranging in size from 1 x 1 to 10 x 10 kilometers, and each square is referenced by a single identifier. The program was modified to determine air trajectory grid square crossing times on this grid and to retrieve corresponding emissions data by the single identifiers.

The program was adapted to a 100 x 100 kilometer emissions grid for the St. Louis region. The grid is positioned with its southwest corner (origin) located at UTM x and y coordinates of 680 and 4,230 kilometers, respectively. The grid, referred to as the ERT grid in this study, is a subregion of the RAPS emissions grid. The ERT grid encompasses 1,664 of the 1,988 RAPS grid squares and all of the RAMS Stations. Emissions from area sources outside of the ERT grid are quite small, and are not considered important for simulation of St. Louis air quality. Point source emissions outside of the ERT grid may be more important. For this reason, there are no geographic boundaries imposed on the use of the RAPS point source emissions data by the model.

In summary, there were no major problems in adapting the model to the St. Louis region. The wealth of data provided by the RAPS program and the forethought given to the design of the data base made for a straightforward adaptation of the model to the region.

6. METHODS AND RESULTS FOR TEST DAY SIMULATIONS

This section describes the methods and model results for the simulations of air quality in the St. Louis region on June 29, July 13, and July 14, 1976. Air parcel trajectories, meteorological conditions, air quality data, initial species concentrations, and predicted concentrations for these days are described and interpreted.

6.1 Air Parcel Trajectories

Hourly surface wind measurements from the RAMS Stations were used to generate receptor-oriented air parcel trajectories for each of the test day simulations. Hourly ozone data for these stations were examined to isolate the hours and stations with high measured ozone concentrations. Backward trajectory space-time histories were generated from several stations at several hours to isolate trajectories suitable for modeling. One trajectory for each day was selected based on the criteria that: (1) the receptor recorded relatively high ozone concentrations; (2) the trajectory start location was within the modeling region; and (3) the trajectory start time was near sunrise. In addition, it was considered desirable for the trajectory to have a rural start location, where pollutant concentrations are generally low in the early morning hours.

Following selection of a single backward trajectory for each day, forward trajectories were then generated using the near sunrise start locations. The reason for running forward trajectories is twofold. First, due to inherent nonlinearities in the method of computing backward trajectories, trajectories generated in the forward direction are believed to be more reliable representations of the wind field. Second, the forward trajectories can be extended beyond the selected receptor location in space and time. Extension of the trajectory duration permits simulation of concentration histories for an entire day, not just the portion which precedes the receptor.

The trajectory selected for June 29, 1976, is illustrated in Figure 6-1. This trajectory starts at 6:00 A.M. southwest of St. Louis, and is oriented to pass RAMS Station 116 at 1:00 P.M. The parcel is advected at moderate wind speeds (4-6 meters/second) across southern St. St. Louis, and passes quite near RAMS Stations 119, 111, and 105 between

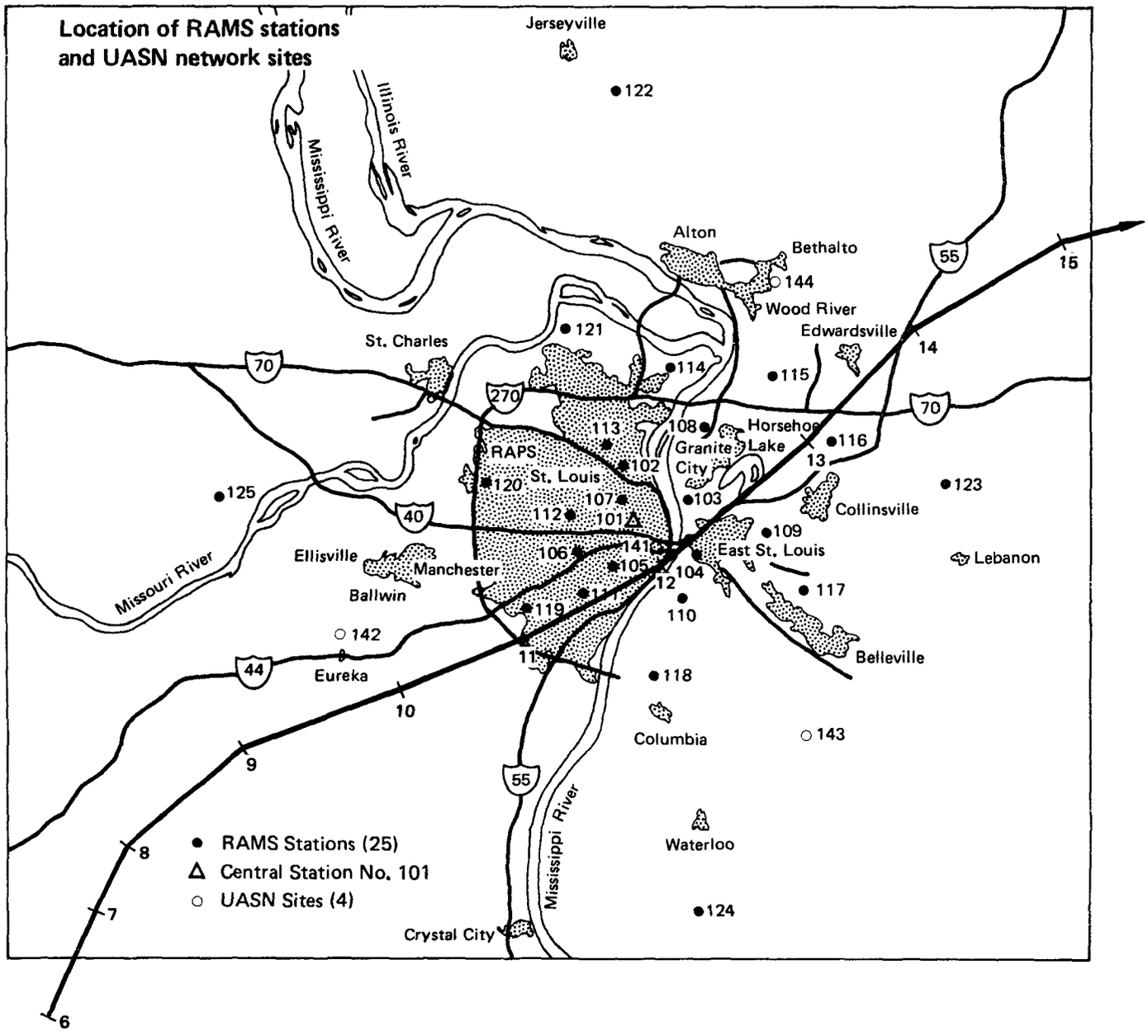

Figure 6-1 Air Parcel Trajectory For 6-29-76

11:00 and 12:00 o'clock. After passing RAMS Station 116 at 1:00 P.M., the parcel continues moving in a northeasterly direction, which eventually carries it out of the modeling region.

The trajectory selected for July 13, 1976, is illustrated in Figure 6-2. The trajectory has a 6:00 A.M. start east of St. Louis, and moves in a northwesterly direction until 1:00 P.M., where it turns north-northeast to arrive at RAMS Station 122 at 4:00 P.M. The air parcel is advected by relatively light winds (1 to 3 meters/second) throughout the day.

The trajectory selected for July 14, 1976, is illustrated in Figure 6-3. The air parcel space-time tract begins west of St. Louis at 6:00 A.M. and moves in a westerly direction throughout the day. It arrives at RAMS Station 117 at 1:00 P.M. and remains in the modeling region until 4:00 P.M. The parcel is advected by wind speeds between 3 and 4 meters/second throughout the day.

6.2 Meteorological Conditions

The meteorological data provided by the RAMS and UASN measurements were processed to establish meteorological conditions along the three test-day trajectories. These measurements are summarized in the following tables and figures. The hourly surface temperatures, wind speeds, mixing heights, atmospheric stability, ultraviolet radiation, and sky clearness are presented in Tables 6-1, 6-2 and 6-3, respectively. Vertical temperature profiles, obtained from radiosondes released at approximately 0400, 1000, and 1600 hours each day, are shown in Figures 6-4, 6-5 and 6-6. The surface temperature, wind speed, and vertical temperature data are used to compute the schedules of mixing coefficient profiles shown in Tables 6-4, 6-5 and 6-6.

Overcast skies characterized the morning hours of June 29, 1976. Atmospheric conditions were relatively unstable with 4 to 6 meters/second wind speeds. A sharp decrease in surface temperature between 1100 and 1200 resulted in stable conditions for that hour. Surface temperature reached a maximum of 29.7° C at 1600 hours. Mixing depth increased from the 200 meter elevation at sunrise to a maximum of 1080 meters at 1600 hours.

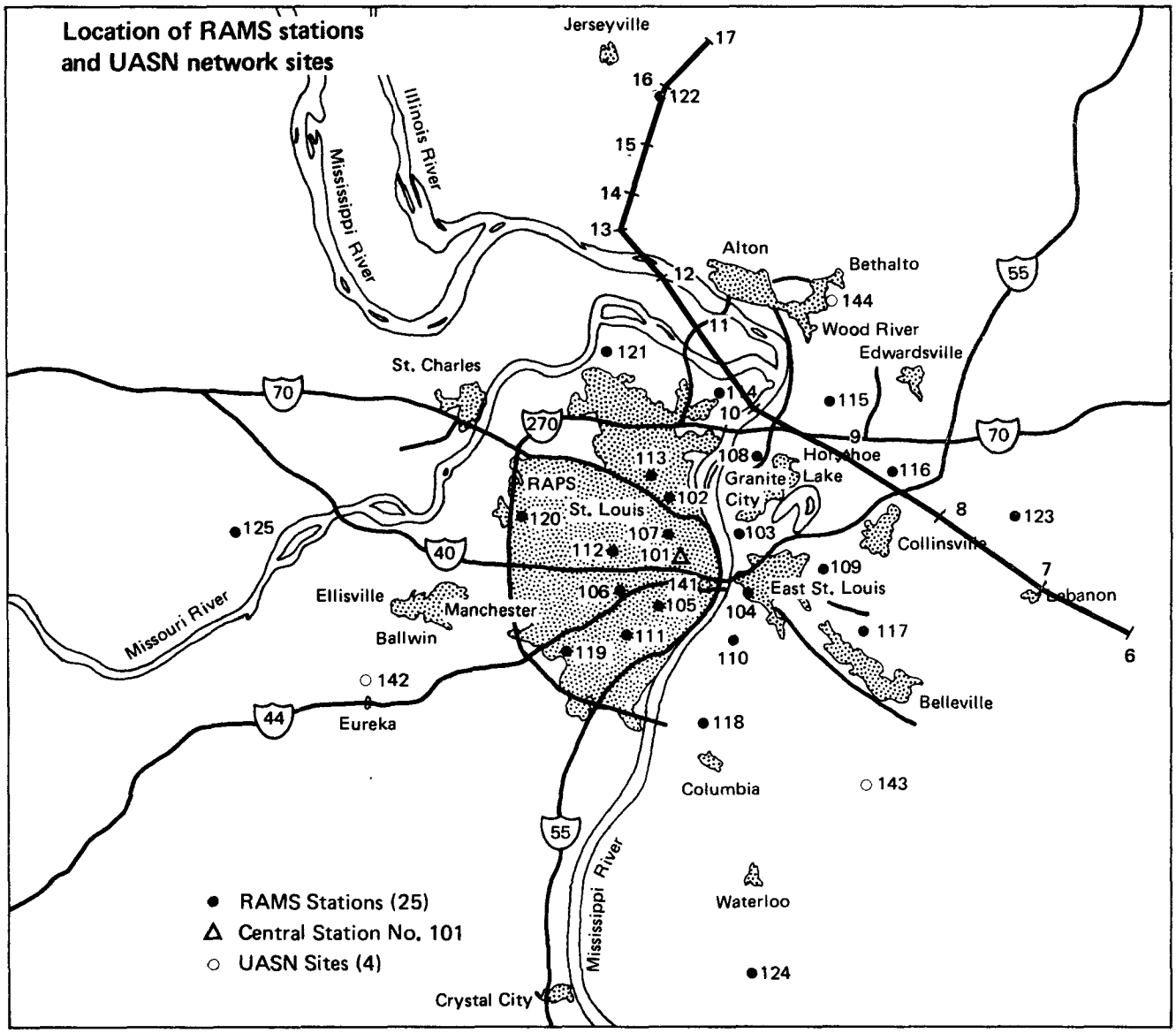

Figure 6-2 Air Parcel Trajectory For 7-13-76

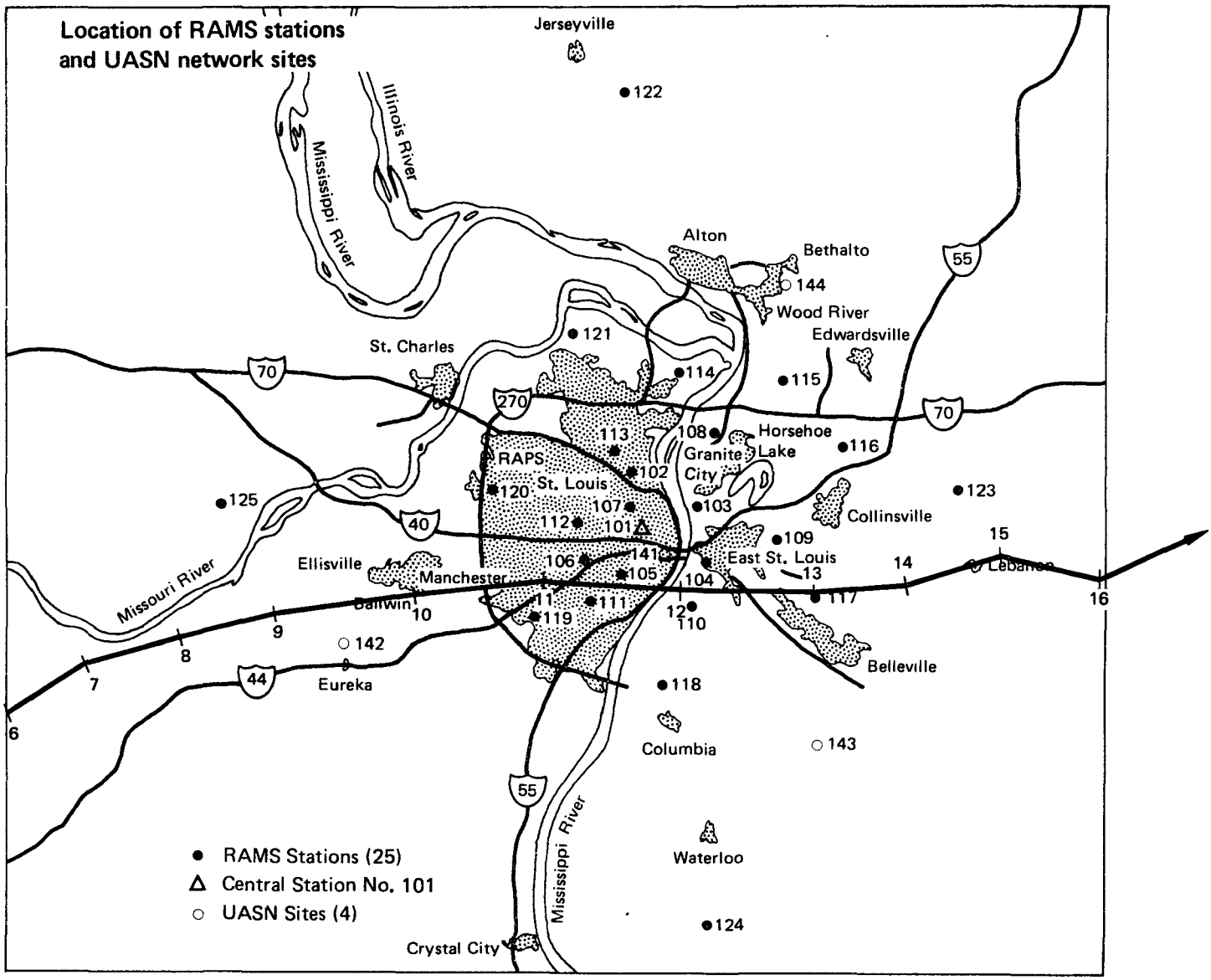

Figure 6-3 Air Parcel Trajectory For 7-14-76

TABLE 6-1

METEOROLOGICAL CONDITIONS FOR 6/29/76

Hour	Surface Temperature[1] (°C)	Wind Speed[2] (m/s)	Mixing Heights[3] (meters)	Atmospheric Stability Class[4] (1-6)	Ultraviolet Radiation[5]	Sky Clearness[6]
6	21.5	3.1	200	2	.0109	.55
7	22.4	2.3	270	2	.0255	.70
8	24.4	4.7	340	2	.0402	.76
9	26.5	4.8	410	2	.0503	.72
10	27.7	4.3	490	2	.0579	.69
11	26.5	4.3	600	5	.0490	.54
12	28.5	6.0	710	2	.0513	.57
13	29.6	5.1	820	2	.0854	1.00
14	29.4	4.5	930	2	.0523	.73
15	29.3	6.0	1040	3	.0541	.97
16	29.7	6.9	1080	2	.0390	1.00
17	29.0	6.9	900	2	.0172	.77

[1]Interpolated to trajectory nodes from the three closest RAMS Stations
[2]Measured at the 30 meter elevation
[3]Estimated from the closest UASN Station
[4]Predicted by the program's eddy diffusivity submodule where classes 1-6 correspond to Pasquill-Gifford classes A-F
[5]Regional average in Langleys/minute from RAMS Stations
[6]Ratio of measured to estimated clear sky ultraviolet radiation

TABLE 6-2

METEOROLOGICAL CONDITIONS FOR 7/13/76

Hour	Surface Temperature[1] (°C)	Wind Speed[2] (m/s)	Mixing Heights[3] (meters)	Atmospheric Stability Class[4] (1-6)	Ultraviolet Radiation[5]	Sky Clearness[6]
6	20.5	2.5	140	5	.0138	.66
7	22.3	3.6	200	1	.0305	.82
8	23.8	3.1	270	1	.0506	.94
9	25.6	3.0	340	1	.0709	1.0
10	27.2	2.7	400	1	.0813	.97
11	28.8	1.9	470	1	.0846	.94
12	30.5	1.7	600	1	.0896	.99
13	31.8	0.9	750	1	.0825	.98
14	32.4	1.6	880	1	.0706	.99
15	32.8	1.9	1020	1	.0555	1.0
16	32.9	2.1	1160	1	.0350	.92
17	32.7	1.7	1300	3	.0117	.82

[1]Interpolated to trajectory nodes from the three closest RAMS Stations
[2]Measured at the 30 meter elevation
[3]Estimated from the closest UASN Station
[4]Predicted by the program's eddy diffusivity submodule where classes 1-6 correspond to Pasquill-Gifford classes A-F
[5]Regional average in Langleys/minute from RAMS Stations
[6]Ratio of measured to estimated clear sky ultraviolet radiation

TABLE 6-3

METEOROLOGICAL CONDITIONS FOR 7/14/76

Hour	Surface Temperature[1] (°C)	Wind Speed[2] (m/s)	Mixing Heights[3] (meters)	Atmospheric Stability Class[4] (1-6)	Ultraviolet Radiation[5]	Sky Clearness[6]
6	24.8	3.0	360	5	.0136	.65
7	27.0	2.8	510	2	.0324	.87
8	29.3	3.2	660	2	.0502	.93
9	31.5	3.8	810	2	.0694	.98
10	33.2	4.0	1000	1	.0856	.96
11	34.2	3.9	1340	1	.0887	.98
12	35.3	3.5	1680	1	.0937	1.0
13	34.3	2.8	2000	1	.0798	.95
14	34.8	3.1	2250	1	.0621	.85
15	35.1	2.9	2500	1	.0525	.96
16	34.9	2.9	2500	1	.0368	.97
17	34.2	3.9	2500	1	.0190	.88

[1]Interpolated to trajectory nodes from the three closest RAMS Stations
[2]Measured at the 30 meter elevation
[3]Estimated from the closest USAN Station
[4]Predicted by the program's eddy diffusivity submodule where classes 1-6 correspond to Pasquill-Gifford classes A-F
[5]Regional average in Langleys/minute from RAMS Stations
[6]Ratio of measured to estimated clear sky ultraviolet radiation

Figure 6-4 Vertical Temperature Profiles (6-29-76)

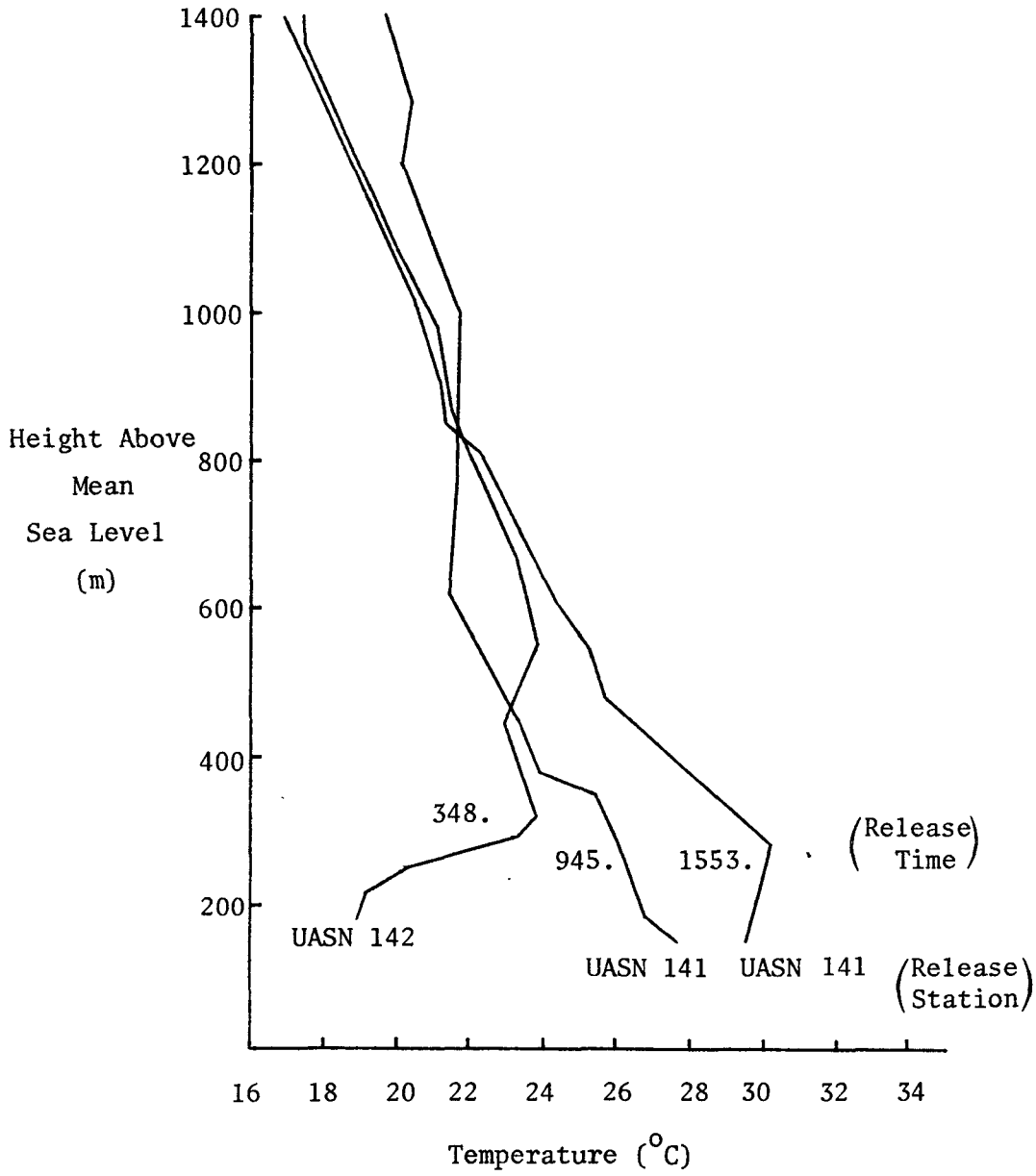

Figure 6-5 Vertical Temperature Profiles (7-13-76)

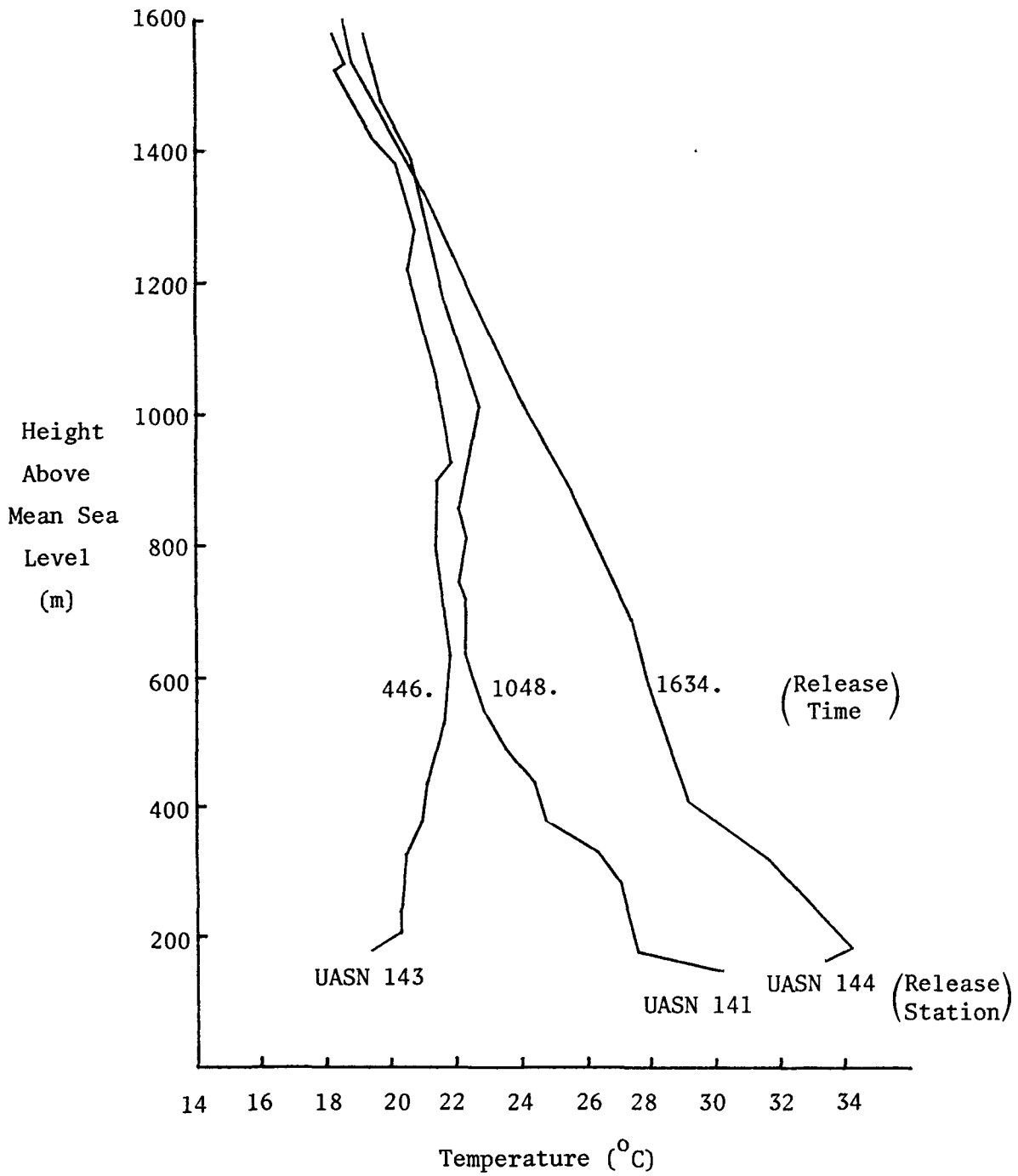

Figure 6-6 Vertical Temperature Profiles (7-14-76)

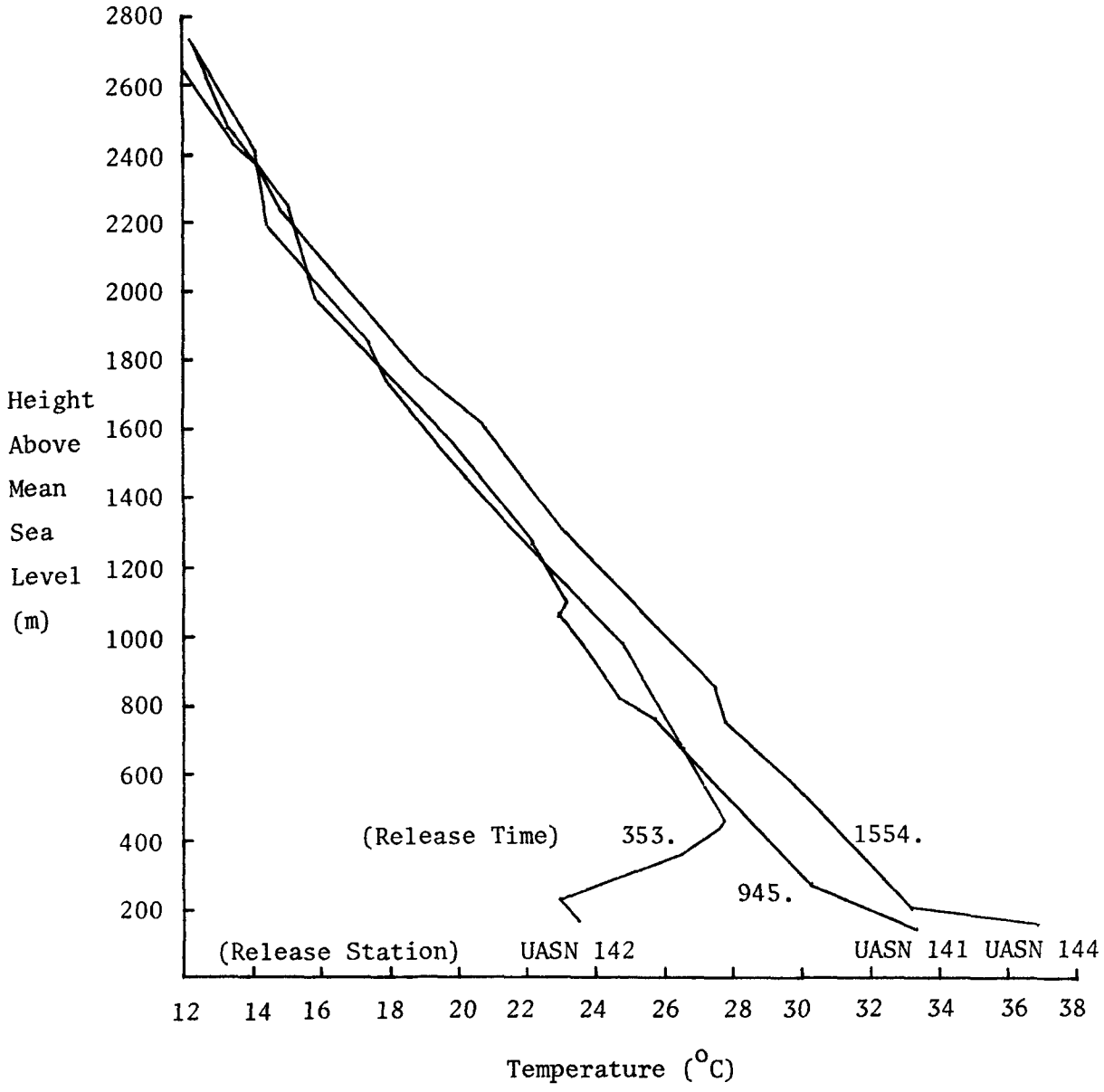

TABLE 6-4

VERTICAL EDDY DIFFUSIVITY COEFFICIENTS* FOR 6/29/76

Hour	Heights (meters) 0-120	120-300	300-600	600-1200
6	9	236	327	126
7	41	166	140	27
8	487	389	842	507
9	1,486	550	867	527
10	1,782	6,202	9,845	1,767
11	137	738	1,495	363
12	3,099	11,193	18,901	6,756
13	2,136	7,654	13,583	10,764
14	1,701	7,383	13,520	10,833
15	1,403	5,940	13,019	10,898
16	104	5,352	7,509	2,520
17	104	5,352	7,509	2,520

* Average K_z coefficient for the height range shown in meters^2/minute.

TABLE 6-5

VERTICAL EDDY DIFFUSIVITY COEFFICIENTS* FOR 7/13/76

Hour	Height (meters) 0-140	140-350	350-700	700-1400
6	26	6	6	6
7	858	9	6	75
8	1,818	787	6	12
9	1,905	2,829	6	8
10	1,758	4,387	453	6
11	1,306	4,037	6,561	3,301
12	1,209	3,824	6,613	7,482
13	624	1,988	3,491	4,233
14	1,114	3,553	6,262	7,709
15	1,325	4,230	7,471	9,271
16	1,494	4,772	8,434	10,492
17	286	947	285	6

* Average K_z coefficient for the height range shown in meters^2/minute.

TABLE 6-6

VERTICAL EDDY DIFFUSIVITY COEFFICIENTS* FOR 7/14/76

Hour	Height (meters) 0-250	250-625	625-1250	1250-2500
6	11	90	6	6
7	146	71	6	6
8	781	104	6	6
9	1,873	159	7	6
10	5,086	13,837	18,981	6,393
11	6,096	16,835	24,039	13,342
12	4,767	13,241	19,337	13,973
13	3,605	10,015	14,625	10,569
14	3,962	11,008	16,075	11,617
15	3,633	10,093	14,740	10,652
16	3,617	10,060	14,732	10,837
17	4,939	13,735	20,113	14,794

* Average K_z coefficient for the height range shown in meters^2/minute.

For July 13, 1976, the processed meteorological data indicate a more typical summer day for St. Louis. Clear skies and continuously-increasing surface temperatures until 1600 hours resulted in unstable atmospheric conditions throughout the day. The mixing height increased from a sunrise elevation of 140 meters to a maximum of 1300 meters at 1700 hours. The relatively light winds resulted in a somewhat smaller vertical dispersion than those calculated for June 29, 1976.

Meteorological conditions for July 14, 1976, were also typical of summer conditions for the St. Louis region. Clear skies, rapidly increasing surface temperatures, and moderate wind speeds combined to create conditions of vigorous vertical mixing. The atmosphere was unstable, with the mixing height extending to 2500 meters by 1500 hours. Surface temperatures and mixing heights are significantly higher than those on the previous day. The range of surface temperatures was from 24.8° C at 0600 to 35.1° C at 1500 hours.

6.3 Air Quality Conditions

The air quality measurements from the RAMS Stations were interpolated along the three test trajectories. Ambient concentrations at the three closest stations are weighted by the square of their inverse distance to the trajectory node to estimate concentrations in the Lagrangian air parcel. Interpolated air quality estimates along each trajectory are listed in Tables 6-7, 6-8 and 6-9 for ozone (O_3), carbon monoxide (CO), methane (CH_4), total hydrocarbons (THC), nitric oxide (NO), nitrogen dioxide (NO_2), and sulfur dioxide (SO_2). The concentrations listed for a particular time represent the average value of measurements taken during the hour following the time listed.

The air quality measurements for June 29, 1976, are fairly typical for a summer day in St. Louis. The ozone concentrations ranged from .06 and .07 parts per million (ppm) between 1300 and 1700 hours. Nitric oxide and nitrogen dioxide concentrations were below .01 ppm, except during the noon hour where they slightly exceed this value. The carbon monoxide concentrations were generally low, between 0.10 and 0.40 ppm, with the exception of a 1.37 ppm peak at 1400 hours. In addition, all the sulfur dioxide monitors reported 0.0025 ppm, which is the lower detectable limit of the measurement instrumentation. These air quality

TABLE 6-7

AIR QUALITY ALONG TRAJECTORY FOR 6/29/76[1]

Hour	O_3 (ppm)	CO (ppm)	CH_4 (ppm)	THC (ppmc)	NO (ppm)	NO_2 (ppm)	SO_2 (ppm)
6	.0293	.133	1.52	1.48	.0031	.0055	-
7	.0220	.240	1.50	1.96	.0052	.0144	.0025
8	.0298	.108	1.47	1.50	.0033	.0082	.0025
9	.0382	.086	1.47	1.44	.0028	.0061	.0025
10	.0436	.216	1.45	1.47	.0033	.0111	.0025
11	.0445	.362	1.38	1.44	.0028	.0069	.0025
12	.0439	.278	1.59	1.66	.0102	.0114	-
13	.0655	.197	1.57	1.66	.0025	.0052	-
14	.0621	1.37	1.51	1.53	.0025	.0057	-
15	.0599	.165	1.49	1.49	.0026	.0076	.0025
16	.0693	.176	1.52	1.48	.0025	.0065	-

[1]Interpolated to trajectory nodes from the three closest RAMS Stations.

TABLE 6-8

AIR QUALITY ALONG THE TRAJECTORY FOR 7/13/76[1]

Hour	O_3 (ppm)	CO (ppm)	CH_4 (ppm)	THC (ppmc)	NO (ppm)	NO_2 (ppm)	SO_2 (ppm)
6	.0335	.120	1.63	1.71	.0025	.0025	-
7	.0391	.114	1.63	1.56	.0025	.0025	-
8	.0447	.089	1.61	1.61	.0025	.0029	-
9	.0475	.139	1.73	1.63	.0036	.0031	-
10	.0631	1.25	1.76	1.79	.0052	.0112	-
11	.0909	.577	1.81	1.95	.0037	.0204	-
12	.1305	.492	1.77	1.93	.0025	.0222	-
13	.1412	.334	1.69	1.74	.0025	.0152	-
14	.1260	.149	1.66	1.53	.0025	.0167	-
15	.1288	.118	1.58	1.54	.0025	.0165	-
16	.1430	.082	1.58	1.52	.0025	.0051	-
17	.1413	.108	1.61	1.56	.0025	.0067	-

[1]Interpolated to trajectory nodes from the three closest RAMS Stations.

TABLE 6-9

AIR QUALITY ALONG TRAJECTORY FOR 7/14/76[1]

Hour	O_3 (ppm)	CO (ppm)	CH_4 (ppm)	THC (ppmc)	NO (ppm)	NO_2 (ppm)	SO_2 (ppm)
6	.0213	.222	1.71	1.66	.0037	.0100	-
7	.0335	.222	1.71	1.67	.0025	.0069	-
8	.0489	.152	1.64	1.58	.0025	.0040	-
9	.0599	.148	1.61	1.54	.0025	.0031	-
10	.0649	.159	1.53	1.50	.0025	.0083	-
11	.0630	.311	1.46	2.69	.0025	.0073	-
12	.0945	.066	1.49	1.43	.0025	.0052	-
13	.0942	.106	1.38	1.54	.0025	.0040	-
14	.0870	.115	1.46	1.46	.0025	.0027	-
15	.0808	.172	1.48	1.46	.0025	.0026	-
16	.0693	.166	1.47	1.44	.0025	.0029	-
17	.0596	.216	1.47	1.42	.0035	.0029	-

[1]Interpolated to trajectory nodes from the three closest RAMS Stations.

measurements are consistent with expected values for the observed meteorological conditions of June 29, 1976. The moderate wind speeds and unstable atmosphere combined to rapidly advect and vertically disperse the pollutant mass in the atmosphere. Reduced ultraviolet radiation, due to overcast conditions, limited the photochemical production of ozone to levels below the Federal Standard of 0.08 ppm.

The air quality measurements for July 13, 1976, show somewhat higher concentrations than those for June 29. The ozone concentrations reached 0.12 to 0.14 ppm between 1200 and 1700 hours. Although the nitric oxide reached a maximum of only 0.005 ppm, the nitrogen dioxide exceeded 0.02 ppm from 1100 to 1300 hours. Carbon monoxide measurements ranged from 0.1 ppm, a typical rural background level for St. Louis, to a maximum of 1.25 ppm at 1000 hours. These somewhat higher ozone and nitrogen dioxide concentrations are consistent with the meteorological conditions of light winds, clear skies, and higher temperatures.

The interpolation of air quality measurements for July 14, 1976, shows ozone concentrations which ranged between 0.08 and 0.094 ppm during the 1200 to 1600 hour time period. The nitric oxide and nitrogen dioxide measurements remained quite low, below 0.0037 and 0.0083 ppm, respectively. Similarly, the carbon monoxide concentration measurements ranged between 0.06 and 0.22 ppm, which are also quite low. These low precursor concentrations are consistent with the meteorological trends for this day. Vigorous vertical mixing of pollutants introduced near the surface to elevations as high as 2500 meters prevented significant build-up of pollutant mass at the surface.

Methane measurements for all three days ranged between 1.38 and 1.81 ppm, which equal or slightly exceed the global background methane concentration, and are believed to be typical of the St. Louis region. The total hydrocarbon measurements range from 1.42 to 2.69 ppmc. It is important to note that the total hydrocarbon measurements are smaller than the methane measurements for approximately half the hours examined. This occurrence indicates that the non-methane hydrocarbons concentrations are generally low since the differences (between methane and total hydrocarbons are within the accuracy limits of the instrumentation employed in the measurement program.

6.4 Source Emission Strengths

Each of the three test-day trajectories has associated schedules of area source and point source emission rates based on the RAPS emissions inventory (provided by EPA) for the corresponding day. These emissions schedules include emission rates for nitrogen oxides, four classes of reactive hydrocarbons (alkenes, alkanes, aromatics, and aldehydes), carbon monoxide, and sulfur oxides. Tables 6-10 and 6-11 list the total number of moles of each species entrained into the air parcels from area sources and point sources, respectively, for each of the three test-day trajectories. The data show that the majority of nitrogen oxide, reactive hydrocarbon, and carbon monoxide emissions are due to sources included in the area source emissions inventory. The major contribution of sulfur oxides to the emission schedules is due to sources included in the point source emissions inventory. In comparing the data for the three different trajectories, it appears that the total emissions for June 29 and July 14 are quite similar, yet the emissions for the July 13, 1976, trajectory are generally lower. The July 13 trajectory did not traverse as much of the emission-intensive metropolitan region as did the June 29 and July 14 trajectories.

6.5 Initial Pollutant Concentrations

The simulation model requires specification of initial pollutant concentrations as inputs. The interpolated RAMS air quality data are used for the surface concentration inputs to the model. Concentrations at elevations above the surface are estimated by means of the following assumptions. Nitric oxide, hydrocarbon, carbon monoxide, sulfur dioxide and sulfate concentrations above the mixing height (or inversion base) are chosen as one-half the measured surface concentration. The concentration at the mixing height is assumed to be two-thirds of the surface concentration. Concentrations at elevations between the surface and mixing height are chosen by assuming a linear rate of change from the surface. Although this formulation is somewhat arbitrary, it is consistent with the physical expectation of precursor pollutant profiles which normally exhibit highest concentrations near the surface and sources.

TABLE 6-10

AREA SOURCE EMISSIONS ENTRAINED ALONG TRAJECTORIES

Date	Moles NOX	PARF	OLEF	AROM	ALDE	CO	SOX
6/29/76	554.	201.	136.	58.	39.	10481.	23.
7/13/76	184.	69.	49.	26.	22.	3913.	10.
7/14/76	608.	272.	168.	67.	45.	12445.	25.

TABLE 6-11

POINT SOURCE EMISSIONS ENTRAINED ALONG TRAJECTORIES

Date	Moles NOX	PARF	OLEF	AROM	ALDE	CO	SOX
6/29/76	103.	30.	9.	39.	.2	852	245
7/13/76	148.	.05	.05	.02	.05	45	216
7/14/76	98.	18.	1.4	32.	.12	117	143

Initial vertical profiles of ozone concentrations are input to the model, assuming that the lowest ozone concentrations occur at the surface. At model mesh point elevations below the mixing height, the ozone concentrations are chosen as one and one-half times the surface measurement. Above the mixing height and below 1500 meters, the ozone concentrations are estimated to be twice the surface values. Above 1500 meters, the ozone concentrations are estimated to be three times the surface value.

These methods for choosing initial pollutant vertical profiles are based on typical shapes of vertical profiles measured by Meteorology Research, Inc.*, during aircraft measurements between the hours of 0500 and 0900 in August, 1977. The location of the measurements was in a rural region near Rockport, Indiana, which is similar to the rural start locations outside of St. Louis modeled in this study. Note that the methods described here provide approximate initial conditions suitable for summer morning trajectories with rural start locations. Uncertainties in these approximations could easily be plus or minus one hundred percent.

An additional task in choosing initial concentrations is the partitioning of individual hydrocarbon class concentrations from the reactive hydrocarbon data. Given a reactive hydrocarbon measurement [RHC] in parts per million as carbon (ppmC), the individual hydrocarbon class concentrations in ppm are estimated as follows:

[Alkanes]	=	.15* [RHC]
[Alkenes]	=	.03* [RHC]
[Aromatics]	=	.03* [RHC]
[Formaldehydes]	=	.02* [RHC]
[Other Aldehydes]	=	.01* [RHC]

These partitioning formulae are based on the assumption of a somewhat aged reactive hydrocarbon mix, so that there are relatively large fractions of the less reactive alkanes and aromatics, and smaller fractions of the more reactive alkenes and aldehydes, than indicated by the St. Louis emissions inventory. The assumption of an aged atmospheric hydrocarbon mixture is appropriate since the formulae are applied

*Blumenthal, 1978.

uniformly to calculate initial conditions at all elevations and in rural locations with low emission densities.

An additional procedure is incorporated in the determination of initial conditions for hydrocarbons as a result of uncertainties in the RAMS measurements. A minimum reactive hydrocarbon concentration of 0.02 ppmC is assumed when the difference between total hydrocarbon and methane measurements is below this level.

The initial pollutant concentration inputs to the model are shown in Figures 6-7, 6-8 and 6-9 for the three test days, respectively. The figures indicate vertical profiles for nitric oxide (NO), alkanes (PARF), alkenes (OLEF), aromatics (AROM), formaldehyde (HCHO), other aldehydes (RCHO), ozone (O_3), carbon monoxide (CO), sulfur dioxide (SO_2), and sulfate (SO_4).

Initial nitrogen dioxide concentrations are calculated by the simulation model from the photostationary state equation shown below:

$$[NO_2] = [NO]\,[O_3]\,\frac{k_1}{k_3}$$

where k_1 and k_3 are the rate constants for the reactions:

$$NO_2 + h\nu \xrightarrow{k_1} NO + O$$

$$NO + O_3 \xrightarrow{k_3} NO_2 + O_2$$

The concentrations of the radical species OH and HO_2 are input with vertically uniform values of 10^{-8} and 10^{-6} ppm, respectively. Initial H_2O concentrations are also input with uniform profiles, and the values assumed for the three test days are shown below.

Date	H_2O Concentrations
6-29-76	1.7×10^4
7-13-76	1.7×10^4
7-14-76	2.2×10^4

Figure 6-7 Initial Pollutant Concentration Vertical Profiles

6 AM 6-29-76

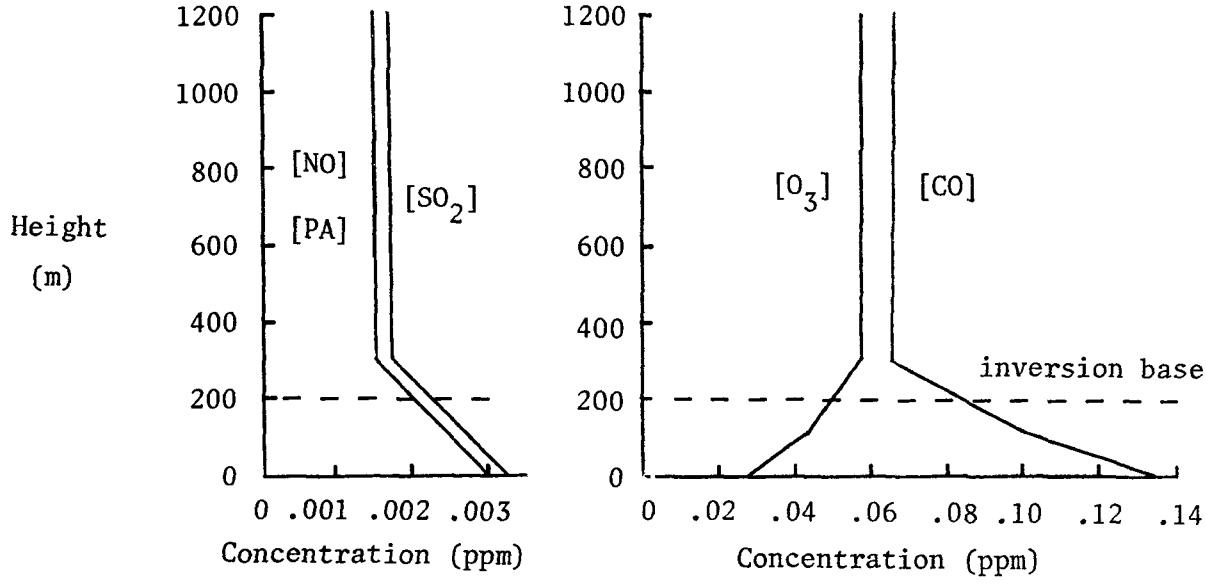

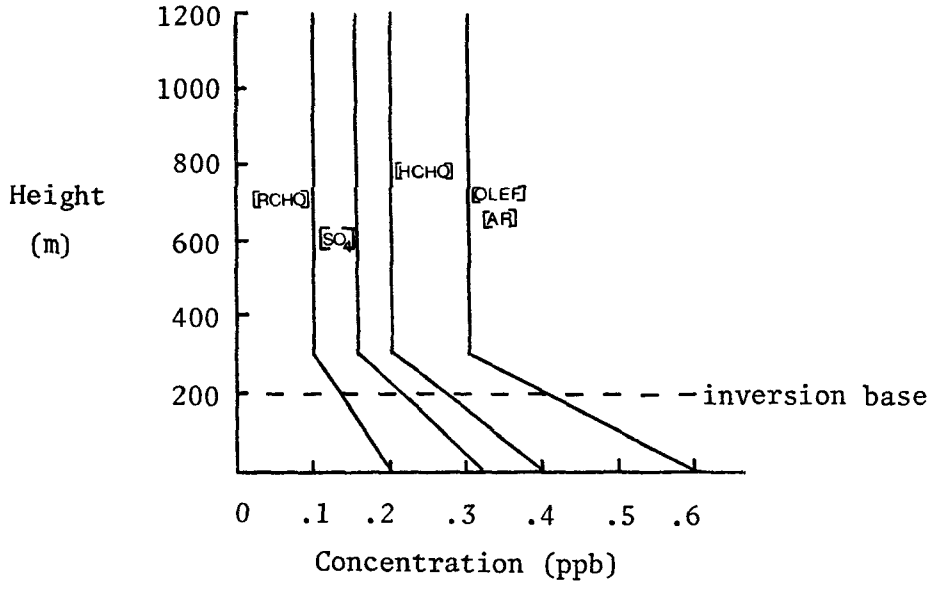

Figure 6-8

Initial Pollutant Concentration Vertical Profiles

6 AM 7-13-76

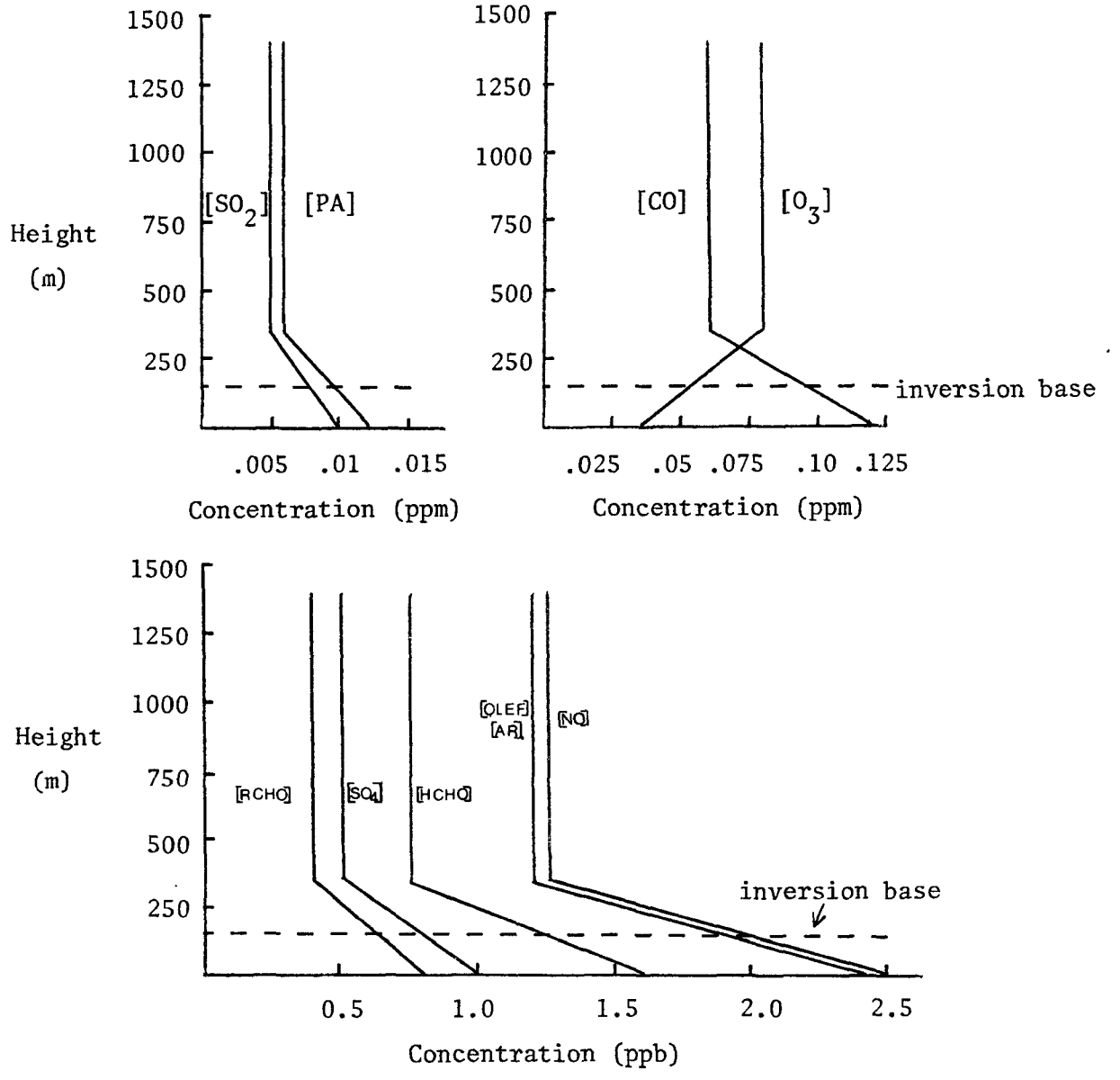

Figure 6-9 Initial Pollutant Concentration Vertical Profiles
6 AM 7-14-76

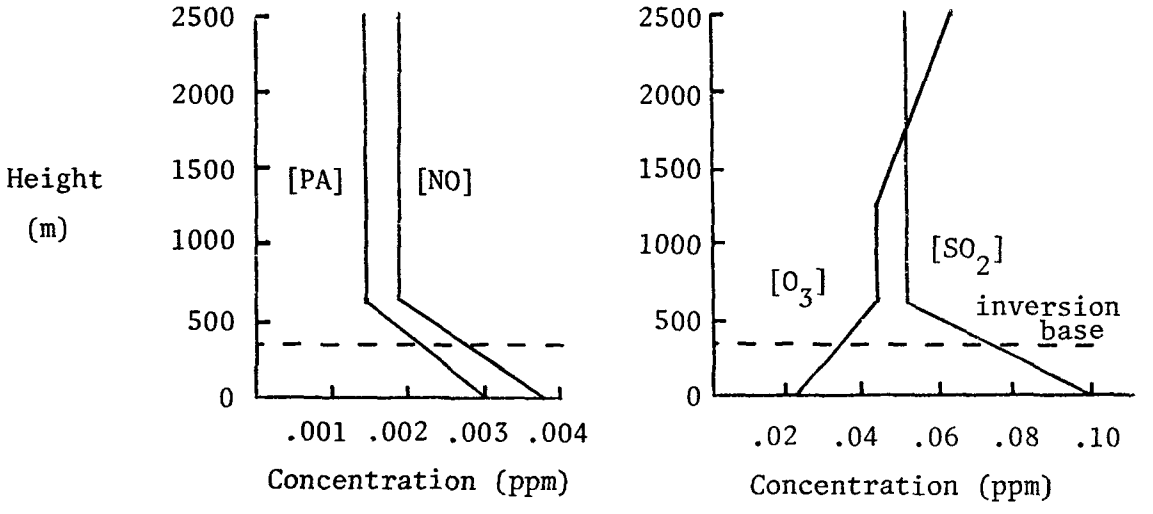

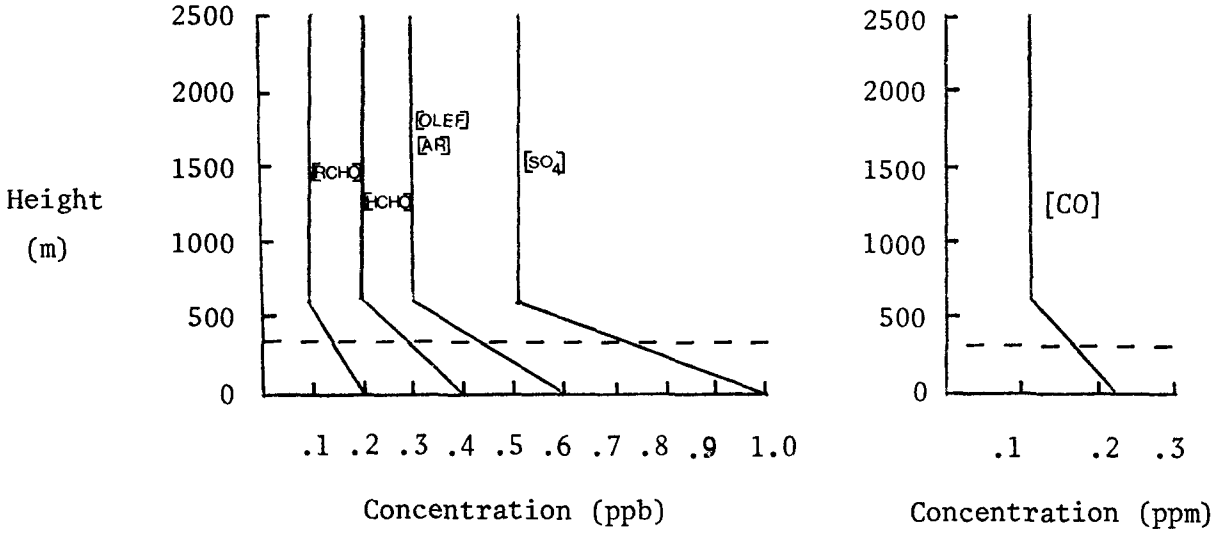

6.6 Simulation Model Results

The ERT Lagrangian Photochemical Diffusion Model was exercised to simulate pollutant concentrations along the three test-day trajectories. The methodology developed for applying the model in the St. Louis region was applied consistently on the three days without adjustment to improve model performance on a particular day. The results are presented in Figures 6-10 through 6-15, which show the predicted surface concentrations of ozone, nitrogen dioxide, nitric oxide, carbon monoxide, sulfur dioxide, and sulfate, and the interpolated RAMS measurements as functions of time.

In examining the model's performance relative to interpolated measurements, it is important to recognize that there are situations where the interpolated measurements may not be truly representative of the air parcel concentrations. Situations arise where the interpolated data represent measurements made at 20 to 60 kilometers away from a given air parcel location along the trajectory. Other situations have been observed where the three closest stations used in the interpolation have recorded concentrations which differ by more than two orders of magnitude. This indicates certain monitors are influenced by local sources, which may or may not influence the air parcel in question. It is believed that these situations are somewhat rare, and, in general, it is felt that the interpolated measurements represent the best available means of comparing concentrations computed in a Lagrangian reference frame to measurements recorded in an Eulerian reference frame. Nevertheless the reliability of the interpolated measurement, as a basis of comparison, is believed to decrease significantly when the distance to the stations exceed the air parcel dimensions.

The model results for the June 29, 1976, trajectory should be viewed with the knowledge that approximately 90% of the source emissions are entrained into the air parcel between 1000 and 1400 hours. The predicted ozone concentrations for the trajectory agree well ($\pm$ .005 ppm) with the interpolated measurements between sunrise and noontime. In the afternoon, the model underpredicts the ozone data. This discrepancy is largest, 0.02 ppm, at 1300 hours when the air parcel passes Station 116. The computed ozone curve shows a reduction between 1100 and 1200 hours caused by both increased nitric oxide concentrations and a reduction in

ultraviolet radiation. The maximum computed ozone concentration of 0.055 ppm occurs around 60 kilometers northeast of downtown St. Louis. Computed nitrogen dioxide concentrations for this trajectory do not agree as well with the interpolated data as do the ozone predictions. The nitrogen dioxide measurements appear somewhat scattered between 5 and 14 ppb, while the computed values show a sharp rise to a midday peak of 16 ppb and a gradual decline in the afternoon hours. Computed nitric oxide concentrations follow trends in the data more closely than nitrogen dioxide. Until 1030, both predicted and measured values for this species are at or near the lowest detectable limit of the instrumentation. The model's NO concentrations increase to a maximum value of 6 ppb at 1130, and the interpolated measurements indicate a peak of 10 ppb at 1200 hours. Afternoon NO concentrations decline to values near the lowest detectable limit (2.5 ppb), which is consistent with the measurement records. The computed carbon monoxide concentrations agree fairly well ($\pm$ .2 ppm) with the interpolated data, except for a significant discrepancy at 1400 hours. Upon closer examination of this discrepancy, we find that the three stations, from which the interpolated value of 1.37 ppm was determined, were measuring widely varying CO levels. The stations, distances, and measurements are listed below.

Station	Distance (km)	[CO] (ppm)
116	15.3	3.67
115	15.9	.15
123	16.3	.05

This tabulation shows that the apparently high interpolated value is due to one high measurement at RAMS 116. Thus, the interpolated value is felt to be unrepresentative of the region, and the discrepancy is understandable. Sulfur dioxide concentrations predicted by the model exhibit trends that are consistent withe the trajectory's SO_x emission schedule. The peak computed SO_2 concentration (7.5 ppb) occurs at 1230 when the air parcel is over southern St. Louis. All the available measurement records indicate an SO_2 level of 2.5 ppb, which is the lower detectable limit of the instruments. Prior to 1100, the computed concentrations are below this level. After 11 o'clock, they are above this level, but since there is only one measurement record after this time, it is

Figure 6-10

Trajectory Model Concentration Predictions for 6-29-76

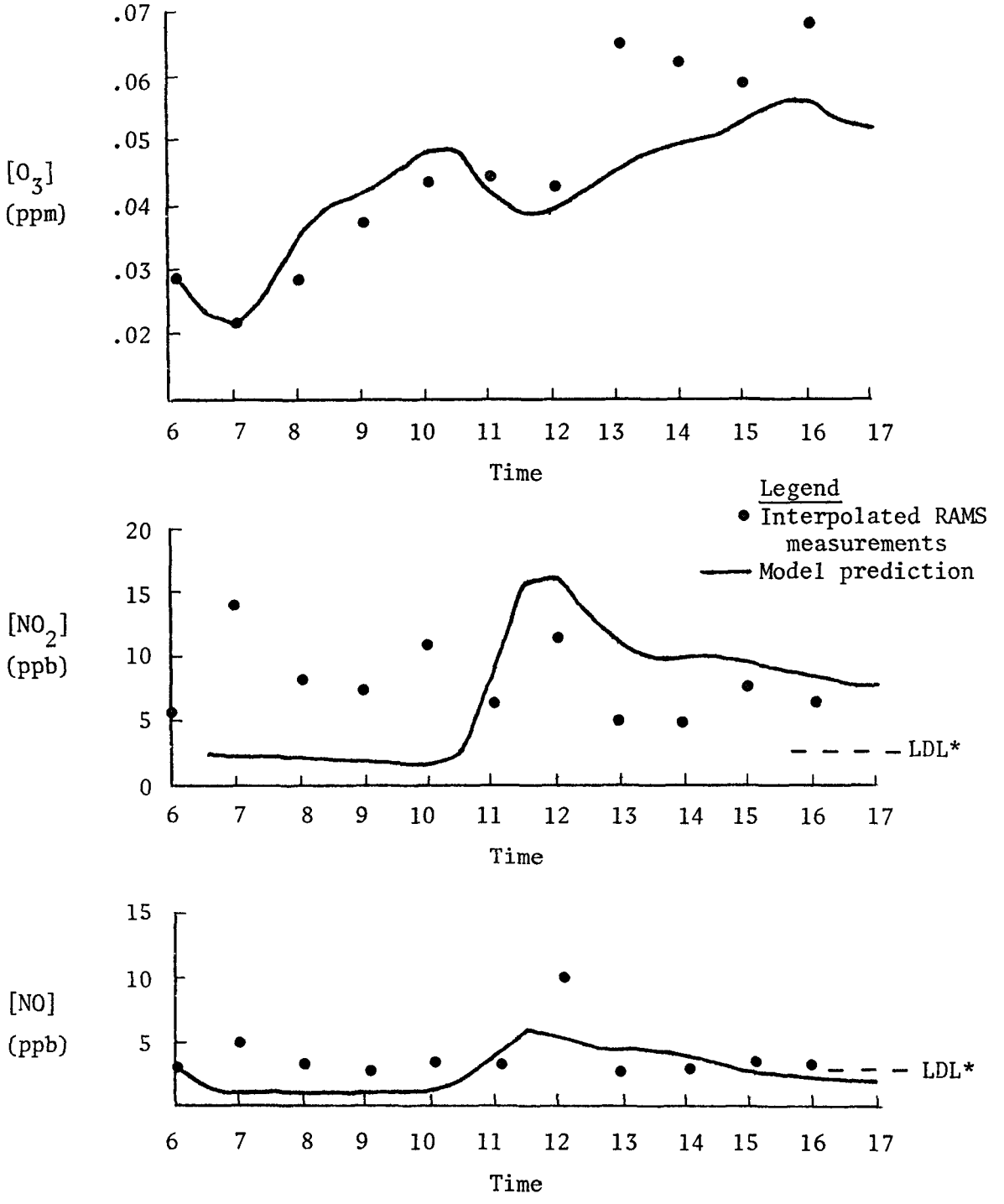

* LDL = Lower Detectable Limit of Instrumentation

Figure 6-11

Trajectory Model Concentration Predictions for 6-29-76

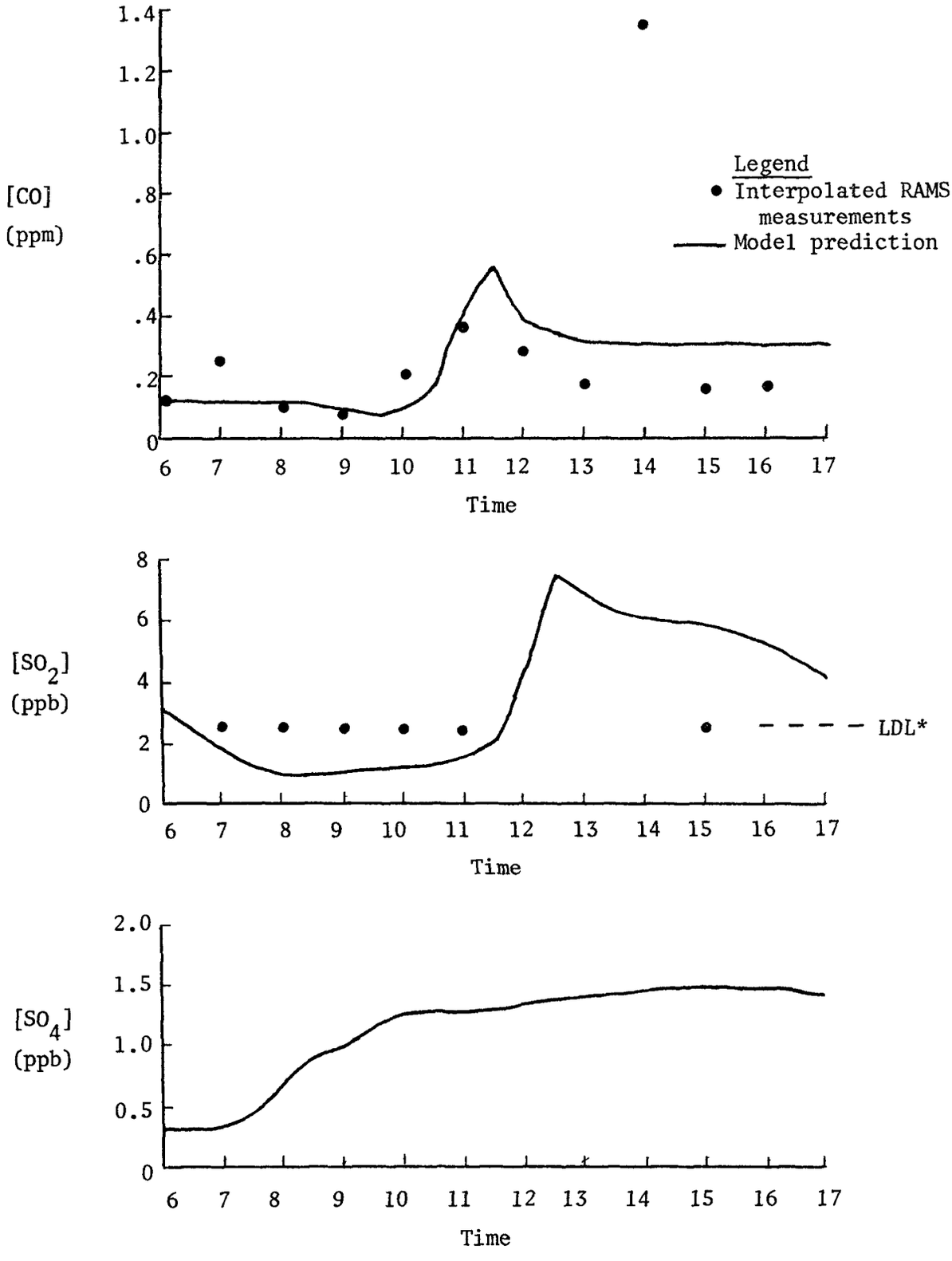

*LDL = Lower Detectable Limit of Instrumentation

difficult to draw conclusions about the model's SO_2 predictive capability from these limited data. Similarly, since hourly sulfate measurements are not routinely archived by the RAPS network, it is not possible to make an assessment of the accuracy of the sulfate predictions. Nevertheless, the computed sulfate concentration history for this trajectory is interesting and unique in this study. The almost constant afternoon concentrations show a balance between the effects of SO_2 conversion to SO_4 and SO_4 surface deposition.

The model results for the July 13, 1976, trajectory indicate that the model underpredicts the interpolated data for all pollutants. Recall that the total emissions used in the simulation of this trajectory are only 1/3 to 1/2 as large as those for the other trajectories, yet the interpolated RAMS data indicate generally higher atmospheric concentrations. The model's computed ozone shows good agreement with the data until 1100 hours, after which these data are underpredicted by 0.03 to 0.06 ppm. The model predicts a peak ozone concentration of 0.098 ppm at 1600 hours when it passes Station 122, where the measured ozone was 0.143 ppm. Computed nitrogen dioxide concentrations for the trajectory are well below the observed values, with the largest discrepancies occurring between 1000 and 1500 hours. The computed nitric oxide concentrations are generally quite low, which is consistent with the measurement records, since most measurements are near the lowest detectable limit for the instrumentations employed. The time of the model-predicted peak nitric oxide concentration agrees with the observed data, but the magnitude of the computed peak is only 40% of the observed maximum. The carbon monoxide concentration predictions are also well below observed levels between 0900 and 1300 hours. The consistent underprediction by the model on this trajectory may be caused by a number of factors. First, the trajectory path generated from the wind data has the smallest levels of pollutant emissions of any of the trajectories in this study. It appears that this trajectory may have missed some major sources of pollutants which influenced the air mass. The wind data show light winds for most of the day. Thus, there is believed to be more uncertainty in the accuracy of the trajectory path on this day than the others in the study. The underprediction may also be attributable to an overestimate of the strength of vertical dispersion for this particular day.

Figure 6-12

Trajectory Model Concentration Predictions for 7-13-76

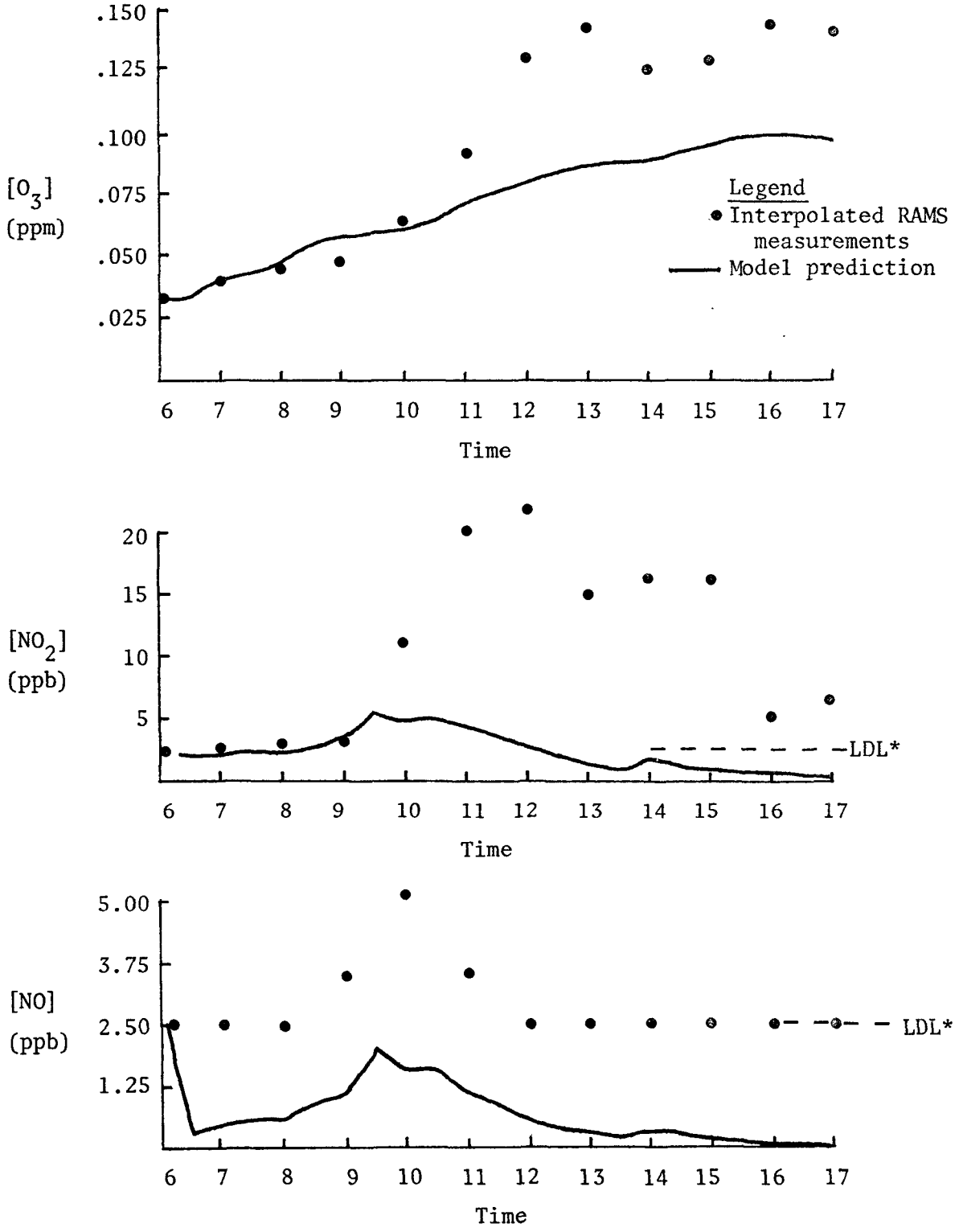

*LDL = Lower Detectable Limit of Instrumentation

Figure 6-13

Trajectory Model Concentration Predictions for 7-13-76

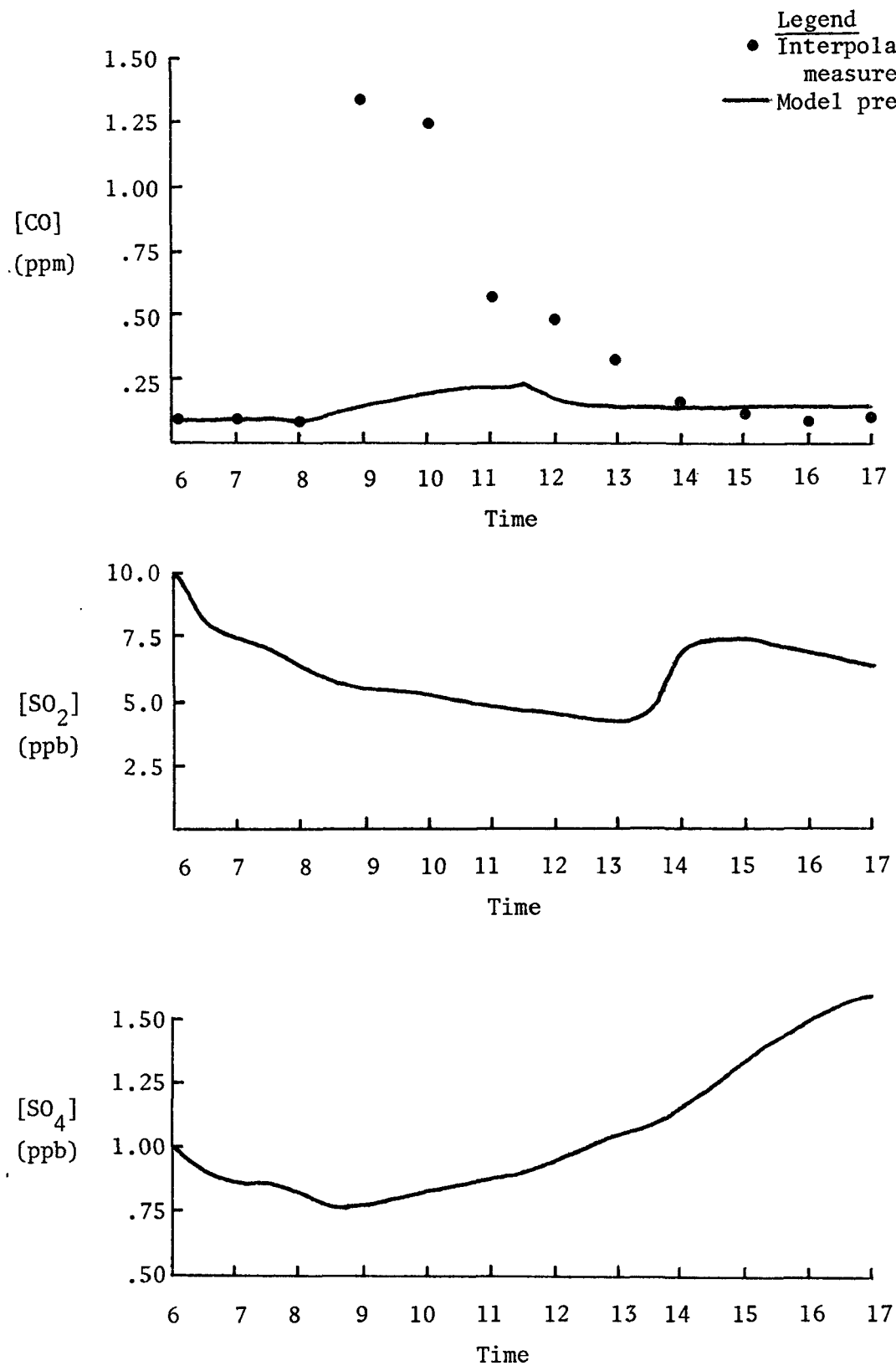

For the July 14, 1976, trajectory, the model predicts ozone concentration below the observed levels. The interpolated RAMS data indicate a maximum ozone level of 0.094 ppm at 1300 when the computed ozone concentration in the parcel has a value of 0.046 ppm. The computed ozone increases to a maximum value of 0.074 ppm at 1700, and the interpolated data show a decline to 0.060 ppm by this time. The model's nitrogen dioxide predictions show good agreement with the data at 0800 and 0900 hours. The model's peak nitrogen dioxide concentration is equal to the observed peak value (8.3 ppb), yet it is predicted at 1200 hours instead of 1000, when the maximum measurement was recorded. The computed afternoon nitrogen dioxide concentrations decline at a rate similar to that indicated by the observed measurements, but they overpredict the observed values by 2 to 3 ppb. Predicted nitric oxide concentrations exceed the interpolated data during the midday hours. The model predicts a maximum concentration of 4.7 ppb nitric oxide at 1200 hours, but all of the data between 0700 and 1600 indicate 2.5 ppb, the lowest detectable limit of the instrumentation. Prior to 1030 and after 1330, the computed nitric oxide values are below 2.5 ppb, which is consistent with the measurement records. The predicted carbon monoxide concentrations agree well ($\pm$ .07 ppm) with the data between 0600 and 1100 hours. The model predicts a peak carbon monoxide concentration of 0.38 ppm at 1130, and the maximum interpolated value along the trajectory is 0.31 ppm at 1100 hours. In the afternoon, the model overpredicts the interpolated data with the largest discrepancies occurring between 1200 and 1400, and smaller discrepancies between 1500 and 1700. Unfortunately, there are no sulfur dioxide measurements archived for this day. Hence, no basis exists for interpretations of the sulfur dioxide or sulfate predictions. It should be pointed out that the initial concentrations of SO_2 and SO_4 are arbitrary and believed to be somewhat higher than might have been observed on this day. They were purposefully chosen somewhat high to demonstrate the effects of the chemistry at somewhat higher concentrations.

In summary, over the three test-day trajectories, the model predictions give best agreement with the interpolated RAMS air quality data for ozone and carbon monoxide, and poorest agreement for nitrogen dioxide. In examining the results for the different days, the model

Figure 6-14

Trajectory Model Concentration Predictions for 7-14-76

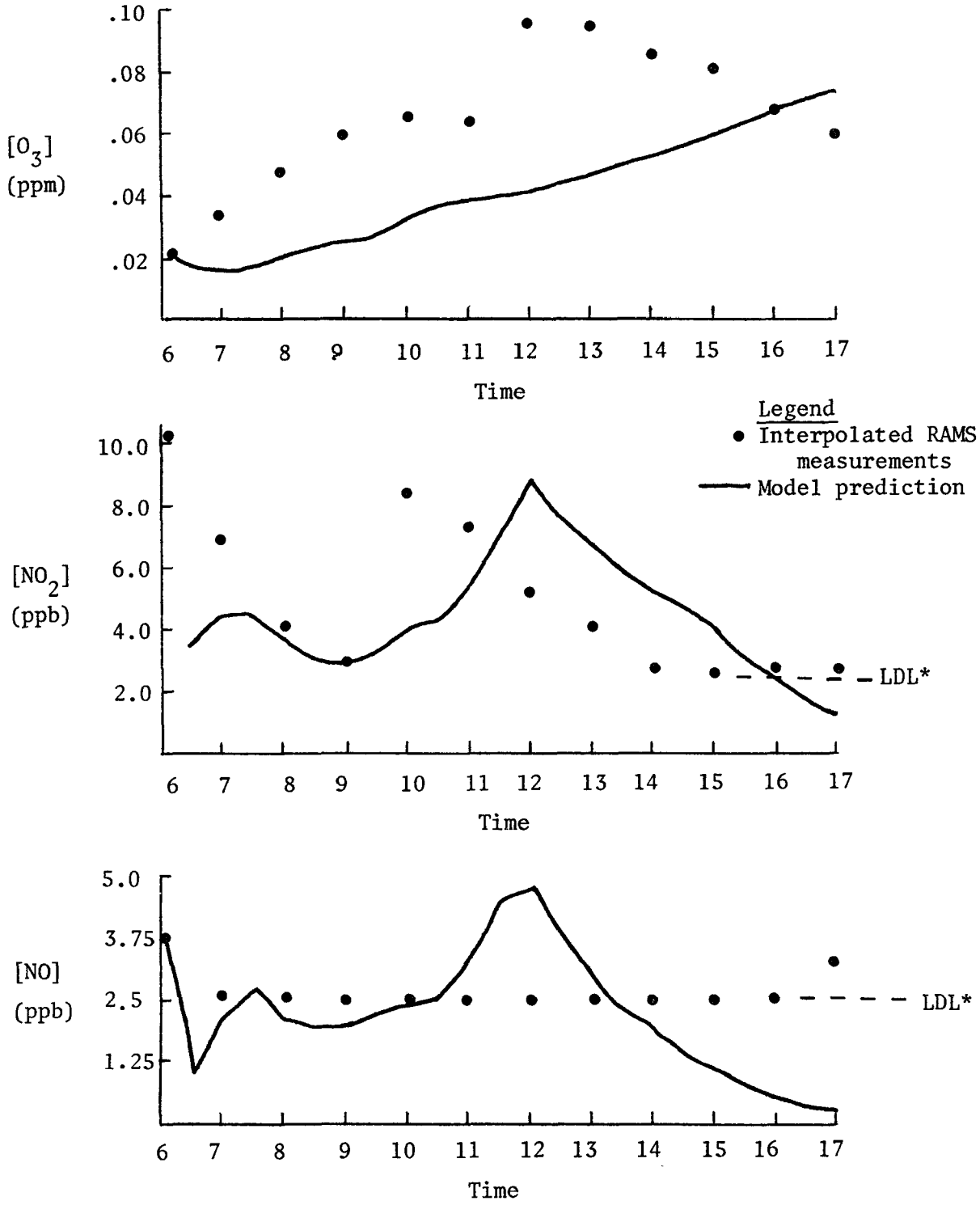

*LDL = Lower Detectable Limit of Instrumentation

Figure 6-15

Trajectory Model Concentration Predictions for 7-14-76

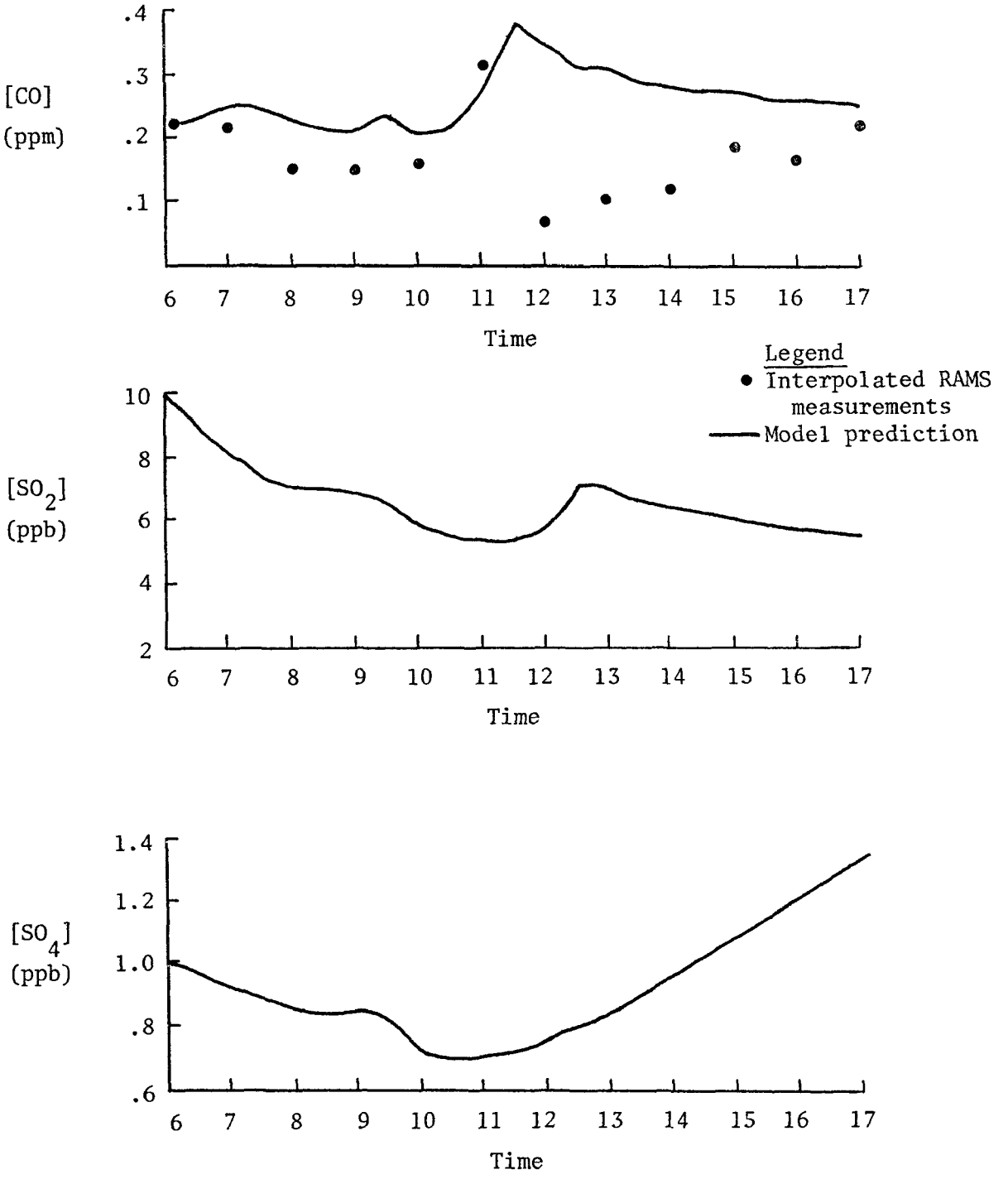

performed best on June 29, 1976, and worst on July 13, 1976. These simulations are viewed as being preliminary demonstration runs for a complex simulation model. Given the wealth of data from the RAPS program, refinements in the methods for selecting trajectories and initial conditions can be made when the model has been exercised for a greater number of days in the St. Louis region. Such refinements have proved important in other geographic areas, and may improve the model's predictive capabilities for the St. Louis application.

7. CONCLUSIONS AND RECOMMENDATIONS

The primary objective of this study has been to provide a Lagrangian photochemical diffusion model to the EPA. The principle conclusions from the study are that the model has been successfully adapted, documented, and demonstrated for use in the St. Louis region, and that its results show a tendency to underpredict measured ozone concentrations.

It is our understanding that the primary reason for the delivery of the model is to provide the means for the EPA to conduct an assessment of the accuracy and validity of the model. In light of this plan, a list of recommendations has been compiled which pertains to the model evaluation. The recommendations cover possible refinements in the modeling of St. Louis, running the model for purposes of evaluation, and how the evaluation may be carried out.

It is suggested that prior to the evaluation of the model, it be exercised more extensively with the RAPS data base. The purpose of these exercises would be to develop procedures for trajectory selection and initial pollutant concentration designation that are more sophisticated than the ones used in this study. Particular attention should be given to the choice of initial conditions and their vertical distributions because there is considerable uncertainty in these inputs and the model predictions are usually sensitive to them. The exercises would involve examining any available elevated pollutant concentration data for St. Louis, as well as examining the model's performance using different initial concentration profiles. These exercises should not be confused with altering the model formulation, which they are not. Rather, the exercises would consist of investigations to reduce the uncertainty in the inputs, using real data and feedback from the model.

It is suggested that a relatively large number of days (20-50) and trajectories be simulated with the model for the evaluation. These selected test days should include a spectrum of meteorological conditions and have data bases as complete as possible. Also, since each of the model's simulations provides information for only one space-time tract through the region, the model should be exercised for several trajectories for each test day. These procedures will enhance the statistical significance of the model evaluation results.

An important aspect of the evaluation, which should be addressed, is how to evaluate Lagrangian concentration predictions relative to data collected in an Eulerian reference frame. In this study, the model results have been compared to the data interpolated from the three closest stations, using reciprocal distance squared weighting of the individual station data. A relatively large maximum distance criteria was used, which allowed data to be interpolated from stations as far as sixty kilometers away from the air parcel location. Given that the resolution of the model is approximately a one kilometer wide space-time tract, such large distances would be unexceptably large for a rigorous evaluation of the model. From a practical standpoint, the maximum distance cannot be chosen too small because this would greatly reduce the number of points of comparison. Thus, as a compromise, it is suggested that the model results be compared to station data measured within five kilometers of the air parcel locations. An obvious exception to this criteria would be when either a station or the air parcel, but not both, is a short distance downwind of a large emissions source. In this case, a maximum distance criteria of less than one kilometer should be applied.

Lastly, the model performance evaluation should be accompanied by some model sensitivity analyses to increase its validity and define areas for further research. In particular, model sensitivity to input parameter variations needs to be established. The magnitude of these variations should be comparable to the uncertainty in the input data. Given the large number of inputs to the model, this task can become a huge one. So, from a practical point of view, the matrix of runs with input perturbations must be limited and carefully chosen. Nevertheless, they should include meteorological, emissions, and chemical input data. The results of such analyses are quite valuable when interpreting the accuracy of the model. For it is believed that the results of a performance evaluation of a model reflect not only accuracy of the physical formulation, but also the accuracy of the inputs.

Since the accuracy and extent of the RAPS data base exceed any other known air pollution modeling data base, the model evaluation studies should reveal the upper limit of air quality predictability with current modeling technology. It is hoped in the course of the evaluation that both strengths and weaknesses of air quality simulation models

be elucidated which may subsequently further the state-of-the-art of the technology.

8. REFERENCES

Anderson, L.G. 1976. J. Geophys. Res. 14: 151.

Atkinson, R., R.A. Perry and J.N. Pitts, Jr. 1976. Rate Constants for the Reactions of the OH Radical With NO_2 (M = Ar and N_2) and SO_2 (M = Ar). J. Chem. Phys. 65(July 1): No.1: 306-310.

Beauchene, J.H., P.J. Bekowies, J.M. McAfee, A.M. Winer, L. Zafonte and J.N. Pitts, Jr. 1973. A Novel 20 KW Solar Simulator Designed for Air Pollution Research. Proceedings of Seventh Conference on Space Simulation (NASA Special Publ. 336). Paper No. 66(Nov. 12-14): 811-825.

Bergstrom, R.W. and J.T. Peterson 1977. Comparison of Predicted and Observed Solar Radiation in an Urban Area. Journal of Applied Meteorology, 16: 1107-1116.

Bergstrom, R.W. and J.T. Peterson 1977. Comparison of Predicted and Observed Solar Radiation in an Urban Area. Journal of Applied Meteorology, 16 pp 1107-1116.

Blackadar, A.K. and H. Tennekes 1968. Asymptotic Similarity in Neutral Barotropic Planetary Boundary Layers. J. Atmospheric Sci. 25: 1015-1020.

Blumenthal, D.L. 1978. Aircraft Measurements of Pollutant and Meteorological Parameters in the SURE Network. Meteorology Research, Inc., report submitted to the Electric Power Research Institute for contracts RP-862-3 and RP-862-4.

Brost, R.A. and J.C. Wyngarrd 1978. A Model Study of the Stably Stratified Planetary Boundary Layer, Manuscript, CIRES, University of Colorado/NOAA, Boulder.

Bufalini, J.J., S.L. Kopczynski and M.C. Dodge 1972. Contaminated Smog Chambers in Air Pollution Research. Environ. Lett. 3: No.2: 101-109.

Businger, J.A., J.C. Wyngaard, Y. Izumi and E.F. Bradley 1971. Flux-Profile Relationships in the Atmospheric Surface Layer. J. Atmospheric Sci. 28: 181-189.

Businger, J.A. and S.P.S. Arya 1974. Height of the Mixed Layer in the Stably Stratified Planetary Boundary Layer. Advances in Geophysics. 18A: 73-92.

Calvert, J.G. 1974. Modes of Formation of the Salts of Sulfur and Nitrogen in an NO_x-SO_2-Hydrocarbon Polluted Atmosphere. Conference on Health Effects of Atmospheric Salts and Gases of Sulfur and Nitrogen in Association With Photochemical Oxidant. Volume II - Reference Documents, T. Timothy Crocker, ed., ARB Contract No. 3-197, University of California (January): VIII-1 - VIII-16. (Available from NTIS as PB 251 233.)

Calvert, J.G. and J.N. Pitts, Jr. 1966. Photochemistry. New York: John Wiley & Sons, Inc.

Calvert, J.G. and R.D. McQuigg 1975. The Computer Simulation of the Rates and Mechanisms of Photochemical Smog Formation. Chemical Kinetics Data for the Upper and Lower Atmosphere. Int. J. Chem. Kinet. Symp. No. 1: 113-154.

Calvert, J.G., Fu Su, Jan W. Bottenheim and Otto P. Strausz 1978. Mechanism of the Homogeneous Oxidation of Sulfur Dioxide in the Troposphere. Atmos. Environ. 12: No.1-3: 197-226.

Carter, William P.L., Karen R. Darnall, Alan C. Lloyd, Arthur M. Winer and James N. Pitts, Jr. 1976. Evidence for Alkoxy Radical Isomerization in Photooxidations of C_4-C_6 Alkanes Under Simulated Atmospheric Conditions. Chem. Phys. Lett. 42(August 15): No.1: 22-27.

Carter, W.P.L., A.C. Lloyd, J.L. Sprung and J.N. Pitts, Jr. 1978. Int. J. Chem. Kin. Accepted for Publication.

Castleman, A.W., Jr, Richard E. Davis, H.R. Munkelwitz, I.N. Tang and William P. Wood 1975. Kinetics of Association Reactions Pertaining to H_2SO_4Aerosol Formation. Chemical Kinetics of Association Reactions Pertaining to H_2SO_4 Aerosol Formation. Chemical Kinetics Data for the Upper and Lower Atmosphere. Int. J. Chem. Kinet. Symp. No. 1: 629-640.

Castleman, A.W., Jr. and I.N. Tang 1977. Kinetics of the Association Reaction of Sulfur Dioxide With the Hydroxyl Radical. J. Photochem. 6: No.5: 349-354.

Chan, Walter H., Robert J. Nordstrom, Jack G. Calvert and John H. Shaw 1976. Kinetic Study of HONO Formation and Decay Reactions in Gaseous Mixtures of HONO, NO, NO_2, H_2O, and N_2. Environ. Sci. & Technol. 10(July): No.7: 674-682.

Chan, Walter H., Robert J. Nordstrom, Jack G. Calvert and John H. Shaw 1976. An IRFTS Spectroscopic Study of the Kinetics and the Mechanism of the Reactions in the Gaseous System, HONO, NO, NO_2, H_2O. Chem. Phys. Lett. 37(Feb. 1): No.3: 441-446.

Chan, Walter H., William M. Uselman, Jack G. Calvert and John H. Shaw 1977. The Pressure Dependence of the Rate Constant for the Reaction: HO + CO → H + SO_2. Chem. Phys. Lett. 45 (Jan. 15): No.2: 240-243.

Cox, R.A. 1974. Photolysis of Nitrous Acid in the Presence of Carbon Monoxide and Sulfur Dioxide. J. Photochem. 3: No.4: 291-304.

Cox, R.A. 1975. The Photolysis of Gaseous Nitrous Acid - A Technique for Obtaining Kinetic Data on Atmospheric Photooxidation Reactions. Chemical Kinetics Data for the Upper and Lower Atmosphere. Int. J. Chem. Kinet. Symp. No.1; 379-398.

Cox, R.A. and S.A. Penkett 1971. Photo-Oxidation of Atmospheric SO_2. Nature. 229(Feb. 12) No.5285: 486-488.

Cox, R.A. and S.A. Penkett 1971a. Oxidation of Atmospheric SO_2 by Products of the Ozone-Olefin Reaction. Nature. 230(Apr. 2): Review Suppl.: 321-322.

Cox, R.A. and R.G. Derwent 1975. Kinetics of the Reaction of Hydroperoxy With Nitric Oxide and Nitrogen Dioxide. J. Photochem. 4: Nos.1-2; 139-153.

Cox, R.A. and R.G. Derwent 1977. The Ultraviolet Absorption Spectrum of Gaseous Nitrous Acid. J. Photochem. 6: No.1; 23.

Cox, Richard A., Richard G. Derwent and Pauline M. Holt 1976. Relative Rate Constants for the Reactions of OH Radicals With H_2, CO, NO, and HONO at Atmospheric Pressure and 296 K. J. Chem. Soc., Faraday Trans. I. 72: Pt.9: 2031-2043.

Cvetanovic, R.J. 1976. Chemical Studies of Free Radicals of Atmospheric Interest. Paper No. 31, 12th International Symposium on Free Radicals, Laguna Beach, California. January 4-9.

Darnall, K.R. 1977. Private communication.

Darnall, Karen R., William P.L. Carter, Arthur M. Winer, Alan C. Lloyd and James N. Pitts, Jr. 1976. Importance of RO_2 + NO in Alkyl Nitrate Formation From C_4-C_6 Alkane Photooxidations Under Simulated Atmospheric Conditions. J. Phys. Chem. 80(Aug. 12): No.17: 1948-1950.

Daubendiek, Richard L. and Jack G. Calvert 1975. A Study of the N_2O_5-SO_2-O_3 Reaction System. Environ. Lett. 8: No.2: 103-116.

Davis, D.D. and Gary Klauber 1975. Atmospheric Gas Phase Oxidation Mechanisms for the Molecule SO_2. Chemical Kinetics Data for the Upper and Lower Atmosphere. Int. J. Chem. Kinet. Symp. No. 1: 543-556.

Davis, D.D. and R. Schiff 1974. Unpublished work.

Davis, D.D., W. Bollinger and S. Fischer 1975. A Kinetics Study of the Reaction of the OH Free Radical With Aromatic Compounds. I. Absolute Rate Constants for Reaction With Benzene and Toluene at 300° K. J. Phys. Chem. 79(Jan.): No.3: 293-294.

Demerjian, Kenneth L., J. Alistair Kerr and Jack G. Calvert 1974. The Mechanism of Photochemical Smog Formation. Advances in Environmental Science and Technology. 4: 1-262. John Wiley and Sons. c.1974. James N. Pitts, Jr. and Robert L. Metcalf, eds.

Dodge, M.C. 1977. Combined Use of Modeling Techniques and Smog Chamber Data To Derive Ozone-Precursor Relationships. International Conference on Photochemical Oxidant Pollution and Its Control - Proceedings. U.S. Environmental Protection Agency. EPA-600/3-77-001b. II(Jan.): 881-889. (Available from NTIS as PB 264 233.)

Dodge, M.C. and T.A. Hecht 1975. Rate Constant Measurements Needed to Improve a General Kinetic Mechanism for Photochemical Smog. Chemical Kinetics Data for the Upper and Lower Atmosphere. Int. J. Chem. Kinet. Symp. No. 1: 155-163.

Dodge, Marcia C. and Gary Z. Whitten 1976. Aldehydes and Photochemical Smog. Paper presented before the Division of Environmental Chemistry, American Chemical Society Centennial Meeting, New York, New York (April 4-9).

Doyle, George J., Alan C. Lloyd, K.R. Darnall, Arthur M. Winer and James N. Pitts, Jr. 1975. Gas Phase Kinetic Study of Relative Rates of Reaction of Selected Aromatic Compounds With Hydroxyl Radicals in an Environmental Chamber. Environ. Sci. & Technology. 9(Mar.): No.3: 237-241.

Durbin, P.A., T.A. Hecht and G.Z. Whitten 1975. Mathematical Modeling of Simulated Photochemical Smog - Final Report, June 1974-June 1975. EPA-650/4-75-026, U. S. Environmental Protection Agency. (June) (Available from NTIS as PB 246 122.)

Egan, B.A. and J.R. Mahoney 1972. Applications of a Numerical Air Pollution Transport Model to Dispersion in the Atmospheric Boundary Layer. J. Appl. Meteorology. 11: 1023-1039.

Fox, D.L. and R.S. Wright 1977. Photochemical Smog Mechanisms -- HC-NO_x-SO_2 Systems. Paper presented at the 4th International Clean Air Congress. Tokyo. (May 16)

Fulle, D.J. 1975. A Lapse Rate-Wind Shear Classification of Turbulent Diffusion. M.S. Thesis, University of Utah, Department of Meteorology.

Gear, C.W. 1971. Algorithm 407 - DIFSUB for Solution of Ordinary Differential Equations. Commun. ACM. 14(March): No.3: 185-190.

Golder, Donald 1972. Relations Among Stability Parameters in the Surface Layer. Boundary-Layer Meteorology. 3: 47-58.

Gordon, Sheffield and William A. Mulac 1975. Reaction of the $OH(X^2II)$ Radical Produced by the Pulse Radiolysis of Water Vapor. Chemical Kinetics Data for the Upper and Lower Atmosphere. Int. J. Chem. Kinet. Symp. No. 1: 289-299.

Graedel, T.E. 1976. Sulfur Dioxide, Sulfate Aerosol, and Urban Ozone. Geophys. Res. Lett. 3(March): No.3: 181-184.

Graedel, T.E., L.A. Farrow and T.A. Weber 1976. Kinetic Studies of the Photochemistry of the Urban Troposphere. Atmos. Environ. 10: No.12: 1095-1116.

Graham, Richard A., Arthur M. Winer and James N. Pitts, Jr. 1977. Temperature Dependence of the Unimolecular Decomposition of Pernitric Acid and Its Atmospheric Implications. Chem. Phys. Lett. 51(Oct. 15): No.2: 215-220.

Haltiner, G.J. and Frank L. Martin 1957. Dynamical and Physical Meteorology. New York: McGraw-Hill Book Company: 227.

Hampson, Robert F. Jr. and David Garvin eds. 1975. Chemical Kinetic and Photochemical Data for Modeling Atmospheric Chemistry. U.S. National Bureau of Standards, Technical Note #866, U.S. Department of Commer. (June): 1-113.

Hansen, D.A., R. Atkinson and J.N. Pitts, Jr. 1975. Rate Constants for the Reaction of OH Radicals With a Series of Aromatic Hydrocarbons. J. Phys. Chem. 79(Aug. 14): No.17: 1763-1766.

Hanst, P.L., E.R. Stephens, W.E. Scott and R.C. Doerr 1958. Atmospheric Ozone Olefin Reactions. The Franklin Institute. Philadelphia, Pennsylvania.

Harris, G.W. and R.P. Wayne 1975. Reaction of Hydroxyl Radicals With NO, NO_2, and SO_2. J. Chem. Soc. Faraday Trans. I. 71: Pt. 3: 610-617.

Hecht, Thomas A., John H. Seinfeld and Marcia C. Dodge 1974. Further Development of Generalized Kinetic Mechanism for Photochemical Smog. Environ. Sci. & Technology. 8(April): No. 4: 327-339.

Hendry, D.G. 1977. Private communications from M.C. Dodge, Progress Report to M.C. Dodge (May).

Hendry, D.G., A.C. Baldwin, J.R. Barker and D.M. Golden 1978. Computer Modeling of Simulated Photochemical Smog. EPA-600/3-78-059, U.S. Environmental Protection Agency (June). (Available from NTIS.)

Hidy, G.M. and C.S. Burton 1975. Atmospheric Aerosol Formation by Chemical Reactions. Chemical Kinetics Data for the Upper and Lower Atmosphere. Int. J. Chem. Kinet. Symp. No. 1: 509-541.

Hindmarsh, R.D. and G.D. Byrne 1975. EPISODE, Lawrence Livermore Laboratory, UCID-20112.

Howard, Carleton J. 1977. Kinetics of the Reaction of HO_2 With NO_2. J. Chem. Phys. 67(Dec. 1): No.11: 5258-5263.

Jeffries, H., D. Fox and R. Kamens 1975. Outdoor Smog Chamber Studies. Effect of Hydrocarbon Reduction on Nitrogen Dioxide. EPA-650/3-75011, U.S. Environmental Protection Agency (June). (Available from NTIS as PB 245 829.)

Lee, Edward K.C., Roger S. Lewis and Richard G. Miller 1976. Photochemistry of Formaldehydes: Past and Present. The 12th Informal Conference on Photochemistry - Extended Abstracts, National Bur. Stand., U.S. Dept. Commer. (June 28-July 1): C2-1.

Levine, S.Z., W.M. Uselman, W.H. Chan, J.G. Calvert and J.H. Shaw 1977. The Kinetics and Mechanism of the HO_2-NO_2 Reactions; the Significance of Peroxynitric Acid Formation in Photochemical Smog. Accepted for publication in Chem. Physics. Lett.

Lloyd, Alan C., Karen R. Darnall, Arthur M. Winer and James N. Pitts, Jr. 1976. Relative Rate Constants for Reaction of the Hydroxyl Radical With a Series of Alkanes, Alkenes, and Aromatic Hydrocarbons. J. Phys. Chem. 80(April 8): No.8: 789-794.

Lloyd, Alan C. and Cindie Tashima 1977. Chemical Mechanism Development for Modeling the Los Angeles Reactive Pollutant Program (LARPP) Data. Prepared for Coordinating Research Council by Environmental Research & Technology, Inc. Preliminary Draft (June 16).

Lloyd, Alan C. 1978. Tropospheric Chemistry of Aldehydes. Environmental Research & Technology, Inc., paper presented at Chemical Kinetic Data Needs for Modeling the Lower Troposphere (Reston, Virginia) (May).

Martinez, J. Raul, Khan T. Tran, Alan C. Lloyd and George M. Hidy 1977. Development of an Atmospheric Model for Sulfate Formation. Environmental Research & Technology, Inc., Document No. P-1534 (Sept.). Prepared for National Science Foundation.

Myrup, L.O. and A.J. Ranzieri 1976. A Consistent Scheme for Estimating Diffusivities to be Used in Air Quality Models. California Dept. of Transportation Report #CA-DOT-TL-7169-3-76-32.

Niki, H. 1977. Private communication.

Niki, H., E.E. Daby and B. Weinstock 1972. Mechanisms of Smog Reactions. Adv. Chem. Ser. No. 113: 16-57.

Niki, H. and B. Weinstock 1975. Environmental Protection Agency Seminar. Washington, D.C. (February).

Niki, H., P. Maker, C. Savage and L. Breitenbach 1976. IR Fourier-Transform Spectroscopic Studies of Atmospheric Reactions. The 12th Informal Conference on Photochemistry - Extended Abstracts, National Bur. Stand., U.S. Dept. Commerc. (June-July): N2-1 - N2-4.

Niki, H., P. Maker, C. Savage and L. Breitenbach 1976a. Fourier-Transform Spectroscopic Studies of Gas-Phase Ozone-Olefin Reactions. ACS Centennial Meeting, New York, New York (April 4-9).

Niki, H., P.D. Maker, C.M. Savage and L.P. Breitenbach 1977a. Fourier Transform IR Spectroscopic Observation of Pernitric Acid Formed Via HOO + NO_2 → $HOONO_2$. Chem. Phys. Lett. 45(Feb. 1): No.3: 564-566.

Niki, H., P.D. Maker, C.M. Savage and L.P. Breitenbach 1977. Fourier Transform IR Spectroscopic Observation of Propylene Ozonide in the Gas Phase Reaction of Ozone--Cis-2-Butene--Formaldehyde. Chem. Phys. Lett. 46(Mar. 1): No.2: 327-330.

O'Brien, J.J. 1970. A Note on the Vertical Structure of the Eddy Exchange Coefficient in the Planetary Boundary Layer. J. Atmospheric Sci. 27: 1213-1215.

O'Brien, R.J. 1975. ACS Meeting, Los Angeles, California, October.

Pate, C.W., R. Atkinson and J.N. Pitts, Jr. 1976. Rate Constants for the Gas Phase Reaction of Peroxyacetyl Nitrate With Selected Atmospheric Constituents. J. Environ. Sci. & Health. Part A: A11: No. 1: 19-31.

Payne, W.A., L.J. Stief and D.D. Davis 1973. A Kinetics Study of the Reaction of HO_2 With SO_2 and NO. J. American Chem. Soc. 95(Nov. 14): No.23: 7614-7619.

Perry, R.A., R. Atkinson and J.N. Pitts, Jr. 1977. Kinetics and Mechanism of the Gas Phase Reaction of OH Radicals With Aromatic Hydrocarbons Over the Temperature Range 296-473 K. J. Phys. Chem. 81(Feb. 24): No.4: 296-304.

Pitts, J.N., Jr. 1975. Int. Conf. on Env. Monitoring, Las Vegas, Sept.

Pitts, J.N., Jr., A.C. Lloyd and J.L. Sprung, 1975. Ecology, Energy and Economics. Chem. Britain. 11(July): No.7: 247-256.

Pitts, James N., Jr., Arthur M. Winer, Karen R. Darnall, George J. Doyle and John M. McAfee 1975a. Chemical Consequences of Air Quality Standards and of Control Implementation Programs: Roles of Hydrocarbons, Oxides of Nitrogen and Aged Smog in the Production of Photochemical Oxidant. ARB-R-3-017-75-52, Air Resources Board, State of California (July). (Available from NTIS as PB 269 376.)

Pitts, James N., Jr., Arthur M. Winer, Karen R. Darnall, George J. Doyle and John M. McAfee 1976. Chemical Consequences of Air Quality Standards and of Control Implementation Programs: Roles of Hydrocarbons, Oxides of Nitrogen and Aged Smog in the Production of Photochemical Oxidant. ARB Contract No. 4-214 (May). University of California.

Pitts, J.N., Jr., A.M. Winer, K.R. Darnall, A.C. Lloyd and G.J. Doyle 1977. Hydrocarbon Reactivity and the Role of Hydrocarbons, Oxides of Nitrogen, and Aged Smog in the Production of Photochemical Oxidants. International Conference on Photochemical Oxidant Pollution and Its Control - Proceedings: Volume II, EPA-600/3-77-001b, U.S. Environmental Protection Agency (January): 687-704. (Available from NTIS as PB 264 233.)

Pitts, James N., Jr., Karen R. Darnall, Arthur M. Winer and John M. McAfee 1977a. Mechanisms of Photochemical Reactions in Urban Air - Volume II. Chamber Studies. EPA-600/3-77-014b, U.S. Environmental Protection Agency (February). (Available from NTIS as PB 265 593.)

Peterson, J.T. 1976. Calculated Actinic Fluxes (290-700 nm) For Air Pollution Photochemistry Applications, EPA-600/4-76-025.

Rao, K.S. and H.F. Snodgrass 1978. The Structure of the Nocturnal Planetary Boundary Layer, National Oceanic and Atmospheric Administration, ATDL Contribution File No. 78/9.

Sander, Stanley P. and John H. Seinfeld 1976. Chemical Kinetics of Homogeneous Atmospheric Oxidation of Sulfur Dioxide. Environ. Sci. & Technol. 10(Nov.): No.12: 1114-1123.

Schofield, Keith 1973. Evaluated Chemical Kinetic Rate Constants for Various Gas Phase Reactions. J. Phys. & Chem. Ref. Data. 2:No.1; 25-84.

Sellers, W.D. 1965. Physical Climatology. Chicago: University of Chicago 152-153.

Shir, C.C. 1973. A Preliminary Numerical Study of Atmospheric Turbulent Flows in the Idealized Planetary Boundary Layer. J. Atmospheric Sci. 30: No.7: 1327-1339.

Sie, B.K.T., R. Simonaitis and J. Heicklen 1976. The Reaction of OH With CO. Int. J. Chem. Kinet. 8: No.1: 85-98.

Simonaitis, R. and Julian Heicklen 1974. Reaction of HO_2 With NO and NO_2. J. Phys. Chem. 78(Mar. 28): No.7: 653-657.

Simonaitis, R. and Julian Heicklen 1976. Reactions of HO_2 With NO and NO_2 and of OH With NO. J. Phys. Chem. 80(Jan. 1): No.1: 1-7.

Singleton, D.L. and R.G. Cvetanovic 1976. J. Am. Chem. Soc. 98: 6812.

Thrush, B.A. and co-workers 1978. Private communication from R. Atkinson.

Walter, Theodore A., Joseph J. Bufalini and Bruce W. Gay, Jr. 1977. Mechanism for Olefin - Ozone Reactions. Environ. Sci. & Technol. 11(Apr.): No.4: 382-386.

Wayne, Lowell, Roy Danchick, Mel Weisburd, Allan Kokin and Arnold Stein 1971. Modeling Photochemical Smog on a Computer for Decision-Making. J. Air Pollut. Control Assoc. 21(June): No.6: 334-340.

Weaver, James, James Meagher and Julian Heicklen 1976. Photo-Oxidation of CH_3CHO Vapor at 3130 A. J. Photochem. 6(Dec.): No.2: 111-126.

Westenberg, A.A. and N. DeHaas 1975. Rate of the Reaction $O + SO_2 + M \rightarrow SO_3 + M$. J. Chem. Phys. 63(Dec. 15): No.12: 5411-5415.

Whitbeck, Michael R., Jan W. Bottenheim, Stuart Z. Levine and Jack G. Calvert 1976. A Kinetic Study of CH_3O_2 and $(CH_3)_3CO_2$ Radical Reactions by Kinetic Flash Spectroscopy. The 12th Informal Conference on Photochemistry - Extended Abstracts. Natl. Bur. Stand., U.S. Dept. Commer. (June-July); K1-1.

Whitten, G.Z. and H. Hogo 1977. Mathematical Modeling of Simulated Photochemical Smog - Final Report. EPA-600/3-77-011, U.S. Environmental Protection Agency, June 1975/June 1976. (Available from NTIS as PB 263 348.)

Wilson, W. et al 1976. Sulfates in the Atmosphere. ACPA Paper 73-30-06. Presented at 69th Annual Meeting of the APCA, Portland, Oregon.

Wood, W.P., A.W. Castleman, Jr. and I.N. Tang 1975. Mechanisms of Aerosol Formation From SO_2. J. Aerosol. Sci. 6(Sept.): No.5: 367-374.

Wu, C.H., S.M. Japar and H. Niki 1976. Relative Reactivities of HO-Hydrocarbon Reactions From Smog Reactor Studies. J. Environ. Sci. & Health - Environ. Sci. & Eng. A11: No.2: 191-200.

Wyngaard, J.C. 1975. Modeling the Planetary Boundary Layer - Extension to the Stable Case. Boundary-Layer Meteorology. 9: 441-460.

Zafonte, L., P.L. Rieger and J.R. Holmes 1975. Some Aspects of the Atmospheric Chemistry of Nitrous Acid. Presented at 1975 Pacific Conference on Chemistry and Spectroscopy. Los Angeles, California. Oct. 28-30.

Zilitinkevich, S.S. 1972. On the Determination of the Height of the Ekman Boundary Layer. Boundary-Layer Meteorology. 3: 141-145.

TECHNICAL REPORT DATA
(Please read Instructions on the reverse before completing)

1. REPORT NO.	2	3. RECIPIENT'S ACCESSION NO.
EPA-600/8-79-015a		

4. TITLE AND SUBTITLE	5. REPORT DATE
A LAGRANGIAN PHOTOCHEMICAL AIR QUALITY SIMULATION MODEL Adaptation to the St. Louis - RAPS Data Base Volume I. Model Formulation	June 1979 6. PERFORMING ORGANIZATION CODE
7. AUTHOR(S) Fred Lurmann, Daniel Godden Alan C. Lloyd and Richard A. Nordsieck	8. PERFORMING ORGANIZATION REPORT NO.
9. PERFORMING ORGANIZATION NAME AND ADDRESS Environmental Research and Technology, Inc. 2625 Townsgate Road Westlake Village, CA 91361	10. PROGRAM ELEMENT NO. 1AA603A AA-045 (FY- 79) 11. CONTRACT/GRANT NO. 68-02-2765
12. SPONSORING AGENCY NAME AND ADDRESS Environmental Sciences Research Laboratory - RTP, NC Office of Research and Development U.S. Environmental Protection Agency Research Triangle Park, NC 27711	13. TYPE OF REPORT AND PERIOD COVERED Final 14. SPONSORING AGENCY CODE EPA/600/09

15. SUPPLEMENTARY NOTES

Volume II.User's Manual -- EPA-600/8-79-015b, June 1979

16. ABSTRACT

A Lagrangian photochemical air quality simulation model has been adapted to the St. Louis, Missouri/Illinois metropolitan region and the Regional Air Pollution Study (RAPS) aerometric and emissions data base. This adaptation was performed to provide a means for EPA to independently assess the validity of a state-of-the-art Lagrangian photochemical model.

Chemical kinetic oxidation mechanisms involving hydrocarbons, nitrogen oxides and sulfur oxides and a vertical diffusion formulation developed by Environmental Research and Technology Inc. for modeling reactive pollutants in the troposphere are described. Methods for determining model input parameters are discussed and model results for ozone, nitrogen dioxide, carbon dioxide, sulfur dioxide, and sulfate are presented for three summer days in 1976. In considering so few simulations, no firm conclusions concerning model reliability are possible, although predicted pollutant concentrations are of reasonable levels. Most noteworthy for future users, the results suggest that the model may predict less ozone than is actually generated in St. Louis. Uncertainty in initial conditions of ozone and organic species is likely responsible for this discrepancy between observed and computed values.

17. KEY WORDS AND DOCUMENT ANALYSIS

a. DESCRIPTORS	b. IDENTIFIERS/OPEN ENDED TERMS	c. COSATI Field/Group
* Air pollution * Hydrocarbons * Nitrogen oxides * Sulfur oxides * Ozone * Data Adaptation * Mathematical models * Photochemical reactions	St. Louis, MO Missouri/Illinois region	13B 07C 07B 12A 07E

18 DISTRIBUTION STATEMENT	19. SECURITY CLASS *(This Report)*	21. NO. OF PAGES
RELEASE TO PUBLIC	UNCLASSIFIED	156
	20. SECURITY CLASS *(This page)*	22. PRICE
	UNCLASSIFIED	

EPA Form 2220-1 (9-73)